Titre: Title:	Simulation of fine powder suspensions
Auteur: Author:	Ramin Mortazavi
Date:	1999
Type:	Mémoire ou thèse / Dissertation or Thesis
Référence: Citation:	Mortazavi, R. (1999). Simulation of fine powder suspensions [Mémoire de maîtrise, École Polytechnique de Montréal]. PolyPublie. https://publications.polymtl.ca/8832/

UNIVERSITÉ DE MONTRÉAL

SIMULATION OF FINE POWDER SUSPENSIONS

RAMIN MORTAZAVI

DÉPARTEMENT DE GÉNIE CHIMIQUE

ÉCOLE POLYTECHNIQUE DE MONTRÉAL

MÉMOIRE PRÉSENTÉ EN VUE DE L'OBTENTION

DU DIPLÔME DE MAÎTRISE ÈS SCIENCES APPLIQUÉES

(GÉNIE CHIMIQUE)

DÉCEMBRE 1999

UNIVERSITÉ DE MONTRÉAL

ÉCOLE POLYTECHNIQUE DE MONTRÉAL

Ce mémoire intitulé:

SIMULATION OF FINE POWDER SUSPENSIONS

présenté par: MORTAZAVI Ramin

en vue de l'obtention du diplôme de: Maîtrise ès sciences appliquées

a été dûment acceptée par le jury d'examen constitué de:

M. LAFLEUR Pierre G., Ph.D., président

M. CHAOUKI Jamal, Ph.D., membre et directeur de recherche

M. GRMELA Miroslav, Doctorat, membre et codirecteur de recherche

M. KLVANA Danilo, Ph.D., membre

ACKNOWLEDGEMENT

I am very thankful to my supervisor, Dr. Jamal Chaouki, for accepting me as a graduate student at the right time when it was very important for me. He gave me the opportunity to work on two great projects of tomography and the subject of this thesis. He always encouraged me to use my imagination in problem solving and tried to make me an independent researcher. I also appreciate all the help, moral, and financial support that he provided me over the last two years and also correcting my thesis.

I am grateful to my co-supervisor, Dr. Miroslav Grmela. He patiently answered every question that I had at any time and after each visit I forgot my stresses. I have profited from his useful suggestions during my studies and his constant support held me steadfast in seeing this research to completion. He also kindly corrected my thesis.

I appreciate Dr Kengo Ichiki from Kyoto University in Japan for his computer program and answering my questions through e-mail.

I thank Dr. Rahmat Sotoudeh Gharabagh for introducing me to my supervisor and orienting me to new environment.
I thank Dr. Ramachandran Deiva Venkatesh for introducing me to this project and the cooperation we had in writing our article.

I appreciate the help of Jean Huard, Andreas Haderlein, Jean-Francois Hamelin, Dr. Richard Labrie, Dr. Michel Bertrand, Dr. Gregory Kennedy, Manouchehr Modirrousta, Ali Amouzadeh, Farzad Ebrahimi, Fredric Lepage, Karim Kiared, Heping Cui, Yunli Fang, Antoine Mongrain, and all other friends.

Finally, I wish to express my thanks to my parents, sisters, brother, and brother-in-law for their support and advice.

RÉSUMÉ

Le comportement hydrodynamique des particules fines en suspension dans une échelle réduite est simulé par des modèles type dynamique stokesienne. Les effets de la taille, de la densité et de la cohésion des particules, ainsi que la vitesse, la densité et la viscosité du fluide, sur la conduite de la suspension sont étudiés. Les sédimentations, les lits fluidisés et les lits à jet sont considérés comme trois cas de suspension.

La méthode de simulation est basée premièrement sur la spécification des interactions des particules entre elles-mêmes et leur environnement, et deuxièmement sur le calcul de trajectoires des particules en se référant aux lois de mouvement de Newton. La méthode Stokesienne de la Dynamique a été utilisée pour le calcul des interactions hydrodynamiques des particules. Les forces inter-particules directes sont représentées dans un modèle analogue à celui de Lennard-Jones.

La distribution des vitesses des particules, la taille des bulles et leurs vitesses, le profil de densité du lit, et autres particularités statistiques du lit ont été calculés. Leur ordre de grandeur est similaire aux mesures expérimentales.

ABSTRACT

The hydrodynamic behavior of fine powder suspensions in micro scale is simulated with the assistance of computers and the effects of particle size, density, and cohesiveness and also fluid velocity pattern, density, and viscosity on the behavior of suspension is studied. Sedimentation, fluidized bed, and spouted bed as three cases of suspensions are considered.

The simulation method is based on , first, specifying the interactions of the particles with each other and with their surrounding, and second, calculating the trajectories of particles by using Newton's laws of motion. Stokesian dynamics method has been used in the calculation of hydrodynamic interactions of particles. The direct inter particle forces are represented in a pattern similar to Lennard-Jones force.

The velocity distribution of particles, bubble size and rising velocity in a fluidized bed, density profile of the bed, and other statistical characteristics of the bed have been calculated.

CONDENSÉ EN FRANÇAIS

La suspension des particules fines dans le fluide est observée dans une large gamme de phénomènes naturels et des montages réalisés par l'homme. Connaître ses comportements constitue une science de base qui peut avoir des applications diverses dans différents domaines. Les particules fines font partie des micro-particules qui ont une taille de l'ordre de 1 à 70 µm. Le sang, par exemple, est une suspension des particules (globules rouges et blancs) dans le plasma. Les particules fines sont utilisées comme des catalyseurs dans une large échelle au sein des réacteurs multiphases dans l'industrie pétrolière, et ont une application majeure dans les industries pharmaceutiques " Happel et Brenner (1986)."

L'objet de ce travail consiste à simuler, en utilisant la dynamique stokesienne, le comportement hydrodynamique des particules fines en suspension. Ceci est effectué d'abord par la spécification des interactions des particules entre elles-mêmes et leur environnement, et ensuite par le calcul de trajectoires des particules en se référant aux lois de mouvement de Newton. Les sédimentations, les lits fluidisés et les lits à jet sont considérés comme trois cas de suspension. Les effets de la taille, de la densité et de la cohésion des particules, ainsi que la vitesse, la densité et la viscosité du fluide, sur la conduite de la suspension sont étudiés. La méthode Stokesienne de la Dynamique a été utilisée pour le calcul des interactions hydrodynamiques des particules.

La simulation d'un cas réel de suspension est complexe, et il est hors de portée de la puissance des ordinateurs ordinaires. Ainsi, nous avons retenu quelques hypothèses simplificatrices qui sont:

1) Pas de réactions chimiques entre les particules.

2) Les particules sont sphériques et sont toutes de la même taille.

3) Les collisions entre les particules sont élastiques.

4) Le diamètre des particules est si grand que les forces Browniennes peuvent être négligées.

5) Afin d'éliminer les termes d'inertie dans les équations de Navier-Stokes, le diamètre de la particule est fixé entre 1 et 70 μm.

6) La suspension à deux dimensions est examinée. C'est-à-dire les particules ont des vitesses 2-D.

7) Seulement 100 particules localisées dans une cellule virtuelle sont examinées.

8) Pour rendre compte des particules rentrant dans une cellule ou sortant de celle-ci, mais aussi de l'interaction des particules avec celles situées en dehors de cellule, nous supposons que chaque cellule est entourée par sa réplique dans toutes les trois dimensions de l'espace.

La simulation est conduite dans deux cas. Dans le premier cas, on suppose qu'il n'y a aucune force directe (non-hydrodynamique) entre les particules. Dans le deuxième cas, on suppose que les particules s'attirent selon un schéma comme celui de forces de Lennard-Jones, et peuvent s'agglomérer entre elles.

Le mouvement de n particules en suspension se déplaçant dans un plan, peut être décrit par l'équation de mouvement, bien connue, de Newton:

$$m\frac{d}{dt}\mathbf{U}(t) = m\frac{d^2}{dt^2}\mathbf{X}(t) = \mathbf{F} \qquad (1)$$

où m, t, $\mathbf{U}$, $\mathbf{X}$ et $\mathbf{F}$ sont respectivement la masse de la particule, le temps, la vitesse des particules, la position des particules, et les forces déployées sur les particules. $\mathbf{U}$, $\mathbf{X}$ et $\mathbf{F}$ sont des vecteurs colonnes de $2n$ éléments chacun relayé aux composants de n particules horizontaux et verticaux. L'équation (1) est rendue sans dimension par la masse d'une particule m_p, la vitesse terminale d'une particule isolée u_t, le rayon d'une particule a, le temps nécessaire à une particule pour traverser son rayon à sa vitesse terminale isolée t_p, et la force de traînée de Stokes appliquée à une particule se déplaçant à sa vitesse terminale isolée $6\pi\mu a u_t$, où μ est la viscosité du fluide. Après la substitution des variables de l'équation (1) par leurs valeurs addimensionnelles, nous obtenons l'équation: $\frac{2\rho_f a u_t}{9\mu}\frac{d}{d\hat{t}}\hat{\mathbf{U}}(\hat{t}) = \hat{\mathbf{F}}$, où ρ_p est la densité de la particule. Nous appelons le coefficient addimensionnel de précédente dérivée le nombre de Stokes, St. Il peut être interprété comme le rapport de l'énergie cinétique d'une particule divisé par le travail de la force de traîné sur le rayon d'une particule. En effet:

$$St\frac{d}{d\hat{t}}\hat{\mathbf{U}}(\hat{t}) = \hat{\mathbf{F}} = \hat{\mathbf{F}}_g + \hat{\mathbf{F}}_{lj} + \hat{\mathbf{F}}_b + \hat{\mathbf{F}}_h \qquad (2)$$

La force résultante déployée sur les particules, $\hat{\mathbf{F}}$, peut inclure la force de gravité $\hat{\mathbf{F}}_g$, les forces directes inter-particules $\hat{\mathbf{F}}_{lj}$, les forces Browniennes $\hat{\mathbf{F}}_b$, et les forces

hydrodynamiques $\hat{\mathbf{F}}_h$. L'équation (2) doit être intégrée deux fois numériquement pour obtenir les vitesses et les positions des particules. Le temps d'intégration est habituellement pris égal à 0.1 fois du temps addimensionnel. Les simulations sont effectuées en générale au cours de 1000 temps addimensionnel qui représente 1.7 à 10 secondes. Nous avons utilisé un ordinateur IBM RISC Système 6000-37T, et avec cette machine il faut environ 3 jours pour terminer 10000 temps d'intégration.

Les trajectoires des particules étant déterminées, nous avons calculé la perméabilité du lit, la taille des bulles leurs vitesses, l'énergie cinétique des particules, la hauteur du centre de la masse des particules, la répartition des vitesses de particules, et la déviation standard de vitesses des particules, pour ainsi comprendre de manière quantitative ce qui se passe à l'intérieur de la cellule.

Quand le nombre de Stokes augmente lors de la simulation des sédimentations, les particules se fixent plus lentement. Ceci est dû à la réduction des effets de viscosité.

Pour la simulation des lits fluidisés, quand le nombre de Stokes augmente, il y a transition de la fluidisation homogène à la celle où apparaissent des bulles. L'énergie cinétique des particules atteint son niveau maximal pour enregistrer une baisse. La hauteur du centre de la masse des particules augmente continuellement sans atteindre un maximum. Quand la vitesse du gaz superficielle augmente, l'énergie cinétique des particules et la hauteur du centre de la masse des particules augmentent aussi. Au cours

de la fluidisation, la hauteur du centre de la masse, l'énergie cinétique des particules, et la déviation standard des vitesses des particules enregistrent un pic quand il y a une bulle dans la cellule. La simulation est effectuée à deux endroits du lit fluidifié. Un près du distributeur dans lequel nous avons utilisé des particules fixes comme distributeur, et l'autre au centre du lit (celui-ci n'a aucune condition limite). Les résultats obtenus sont conformes à ce qu'on trouve dans la littérature.

Dans la simulation des lits à jet, le mouvement cyclique des particules est reproduit.

Les résultats de simulations sont similaires aux résultats obtenus par des observations expérimentales. L'échelle de simulation, qui est beaucoup plus petit à celle retenue dans les applications industrielles, peut être agrandie en utilisant les ordinateurs modernes plus puissants. Les recommandations suivantes peuvent être suggérées pour la poursuite de ce travail dans l'avenir:

1) Simuler des particules non sphériques avec des tailles différentes.
2) La force de Lennard-Jones est isotrope. Les particules peuvent librement glisser l'une sur l'autre aussi longtemps que la distance entre deux particules ne change pas. Il est recommandé d'inclure les forces qui empêchent les particules attachées de changer d'orientation.
3) Simuler le comportement de particules plus larges en utilisant l'équation de mouvement de Navier-Stoke.

4) Inclure les réactions chimiques entre les phases gaz-particule et/ou particule-particule.

5) Simuler plusieurs cellules en parallèle sans utiliser la méthode de condition de limitation périodique .

6) Simuler les suspensions en 3D

TABLE OF CONTENTS

LIST OF FIGURES

LIST OF SYMBOLS

a	Radius of a particle, m
a	Constant in Lennard-Jones formula
b	Constant in Lennard-Jones formula
$\mathbf{E}_z$	Array of gravity force in dimensionless form
$E(\omega)$	Energy spectrum of particle velocities
F	Force applied on a particle
$\mathbf{F}$	Array of forces applied on particles
$\hat{\mathbf{F}}$	Array of forces applied on particles in dimensionless form
$\hat{\mathbf{F}}_b$	Array of Brownian forces in dimensionless form
F_d	Drag force
$\hat{\mathbf{F}}_g$	Array of gravity forces in dimensionless form
$\hat{\mathbf{F}}_h$	Array of hydrodynamic forces in dimensionless form
$\hat{\mathbf{F}}_{lj}$	Array of Lennard-Jones forces in dimensionless form
$\mathbf{F}_m$	Array of forces applied on mobile particles
F_{max}	Maximum Lennard-Jones force between two particles
$\hat{\mathbf{F}}_p$	Array of forces applied from particles on fluid in dimensionless form
g	Acceleration due to gravity

$\tilde{g}$	Effective gravitational acceleration defined as $\frac{\rho_p - \rho_f}{\rho_p} g$
h	Altitude
k_B	Boltzmann's constant, 1.381×10^{-23} J / K
$\hat{k}_i$	Component of the unit vector in the direction of $\mathbf{k}_\lambda$
$\mathbf{k}_\lambda$	Position of a periodic cell in reciprocal space
L_1	Length of a periodic cell
L_2	Width of a periodic cell
L_3	Height of a periodic cell
$\overline{L}$	Geometric average length of a periodic cell
m	Mass of a particle
m	Constant in Lennard-Jones formula
M	Mobility matrix
M^∞	Far-field mobility matrix
m_p	Mass of a particle
n	Constant in Lennard-Jones formula
N	Number of particles in a periodic cell
n_p	Fraction of particles in a periodic cell with specified characteristic
p	Pressure, Pa
Pe	Peclet number
$\mathbf{r}$	Center to center vector between two particles

$\hat{r}_i$	Component of the unit vector in the direction of **r**
$\mathbf{r}_\gamma$	Position of a periodic cell in real space
R	Resistance matrix
R^∞	Far-field resistance matrix
R_{2B}	Two-body resistance matrix
R^∞_{2B}	Far-field two-body resistance matrix
R_{ff}	Resistance submatrix among fixed particles
R_{mf}	Resistance submatrix among mobile-fixed particles
R_{mm}	Resistance submatrix among mobile particles
$\mathrm{Re_p}$	Particle Reynolds number
St	Stokes number
S	Separation between surfaces of two particles
S_{F0}	Separation in which the Lennard-Jones potential is at its minimum value
$S_{F,\max}$	Separation in which the Lennard-Jones force is at its maximum value
t	Time, s
t_p	The time that takes a particle to travel its radius at its isolated terminal velocity
$\hat{t}$	Time, made dimensionless by t_p
T	Absolute temperature
t_r	Relaxation time

V_p	Volume of a particle
V_{lj}	Lennard-Jones potential
V	Dimensionless volume of a periodic cell
VF	Average volume fraction of particles
VD	Average velocity distribution of particles
W	Width of a periodic cell
X	Position of a particle
$\mathbf{X}$	Array of positions of particles
$\hat{\mathbf{X}}$	Array of positions of particles, made dimensionless by radius of a particle
x	Position
$x^a_{\alpha\beta}$	mobility function
$X^A_{\alpha\beta}$	Resistance function
$Y^A_{\alpha\beta}$	Resistance function
$y^a_{\alpha\beta}$	Mobility function
μ	Viscosity of fluid
ρ_p, ρ_f	Density of particle and fluid
v	Velocity of fluid
γ	Index vector of periodic cells in real space
λ	Index vector of periodic cells in reciprocal space
λ	Radius ratio

$\delta_{i,j}$	Kronecker delta
ξ	$\frac{\sqrt{\pi}}{L}$

LIST OF APPENDICES

CHAPTER 1: INTRODUCTION

Suspensions of fine particles in a fluid are found in a wide range of natural phenomena and man-made settings and knowing its behavior is a basic science that can be applied in many different cases. Blood, for example, is a suspension of red cells and white cells in plasma. Powders are used as catalyst on a large scale in multiphase reactors in petroleum industries and they have a major application in pharmaceutical industries, " Happel and Brenner (1986)."

Fine particles fall into category of micro particles as shown in Figure 1.1. These particles are located between macromolecules and macro particles. The size of particles is less than the thickness of human hair and milled flour and red blood cells are samples of these particles. Particles have diameter between 1 and 70 μm. In this range of particle size the Reynolds number is lower than one; because of this, we can use the linearized form of the equations of motion which results from omitting the inertial terms of the Navier-Stokes equations, giving the so-called creeping motion or Stokes equations. Many systems that involve bulk flow relative to external boundaries at high Reynolds number are still characterized by low Reynolds number as regards the movement of particles relative to fluid. Also inertial effects are less important for systems consisting of a number of particles in a bounded fluid medium than they are for the motion of a single particle in an unbounded fluid.

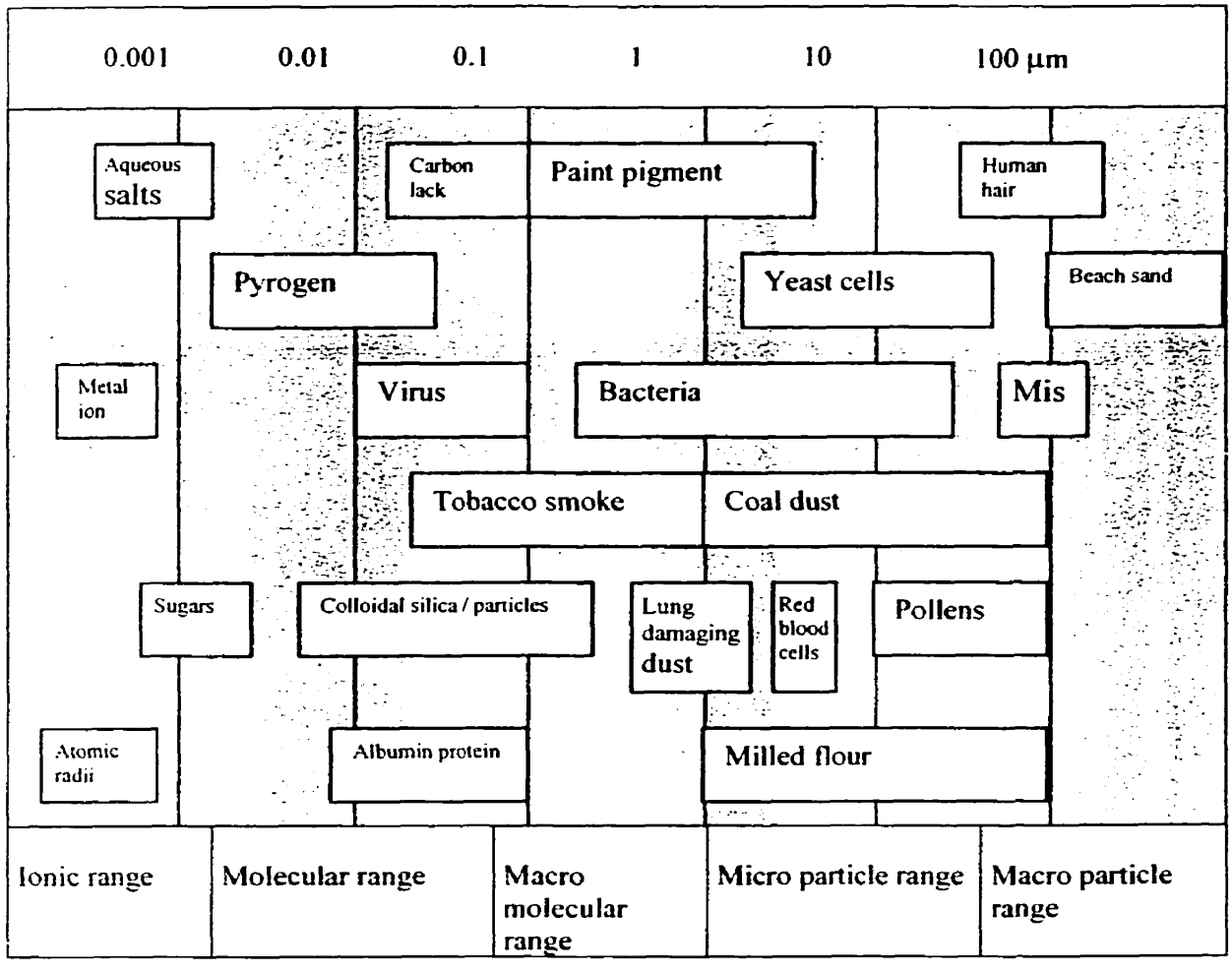

Figure 1.1 The particle size spectrum of micro hydrodynamics. From: " Kim and Karrila (1990) in Microhydrodynamics, Principles and selected applications page 4

Depending on the pattern of fluid flow, suspension may be in sedimentation, fluidization, or spouted mode. In sedimentation, particles move together in bulk through a fluid. Fluidization is the levitation of a mass of particles by a fluid moving in the opposite direction of gravity. In this state, the particle mass behaves like a fluid in that it tends to establish a level and flow in response to pressure gradients. An intense mixing occurs and

gas solids contact increases. These properties make it easy to have a system with high heat and mass transfer. The fluidized beds can be used as a means of heat and / or mass transfer between i) gas and particles, ii) particles and particles, iii) particles and surface of the bed, heat transfer between iv) bed and surface, v) gas-gas reactions in which solid acts as catalyst or a heat sink, and vi) gas-solid reactions in which solids are transformed. A good quantitative knowledge of the hydrodynamics of fluidization would make it possible to design an efficient multiphase reactor or heat and mass transferring equipment.

The variety of fluidized beds encountered in commercial operation is enormous. It includes powders having mean sizes as small as 15 μm and as large as 6 mm, bed diameters from 0.1 to 10 m, bed depths from a few centimeters to 10 m and gas velocities from 0.01 to 3 m/s or even as high as 10 m/s for recirculating high velocity beds.

Spouted bed is a special configuration of a fluidized bed in which gas is injected at high velocity through a hole located at the center of the bottom of a column. In this bed particles rise rapidly in a hollowed central core within the bed of solids. These particles, after reaching somewhat above the surface of bed, rain back onto the annular region between the hollowed core and the column wall, where they slowly travel downward and, to some extent, inward as a loosely packed bed. The characteristic of spouted bed is the cyclic motion of particles from bottom to top of column and vice versa.

Three categories of models have been proposed to describe a suspension. The first one is two-fluid model " Ding and Gidaspow (1990), Kuipers et al. (1992)." In this model both solid and gas phases are considered as a fluid and are assumed to be fully interpenetrating. Both phases are described in terms of separate conservation equations, governing the balance of mass, momentum and energy in each phase. Appropriate interaction terms are used to represent the coupling between the phases. This model has the benefit of analytical treatments. However, parameters included in the constitutive equations for the solid phase lack generality. Some parameters arising in the constitutive equations can be determined only empirically by requiring the fit with results of observations. The role of particle motions is not clear because the particles are seen in the model as a fluid; consequently, a clear understanding of the role of particle motion in macroscopic properties cannot be reached. Furthermore, particle shape and size distribution cannot be accounted for in the fluid-type models.

The second model is Distinct Element Method (DEM) " Tsuji, Kawaguchi, Tanaka (1993), Hoomans, Kuipers et al. (1995) ". In this model the motion of each single particle is directly calculated while accounting for interactions with other particles and the continuous fluid. Particles interact with each other through contact forces. These forces are calculated with simple mechanical models such as a spring, a dashpot and a friction slider. A phenomenological model is used to describe the fluid motion and the resistance between the fluid and the particles. In this way hundreds of thousands of particles have been successfully simulated and a realistic motion of particles is reproduced. However it

oversimplifies the interaction among particles. For instance, the boundary condition between the particles and fluid is not satisfied on the scale of particle. The other disadvantage of this model is its dependency on empirical parameters.

The third model that is chosen in this thesis is Stokesian Dynamics Method (SDM), " Durlofsky, Brady, Bossis (1987), Brady, Bossis (1988) ". It is based completely on basic principles such as Navier-Stokes equations of motion and Newton's laws of motion. It does not need any empirical parameters. The only information that is needed is particle radius, the particle-particle interactions, the mass densities of the fluid and the particles, and the shear viscosity of the fluid. Particles may interact through both hydrodynamic and non-hydrodynamic forces. The simulation method is valid both for dilute or concentrated systems.

1.1 Research objectives

The objective of this work is to simulate, with the assistance of computers, the hydrodynamic behavior of fine powder suspensions. This is done by, first, specifying the interactions of the particles with each other and with their surrounding, and second, calculating the trajectories of the particles by using Newton's laws of motion. Sedimentation, fluidized bed, and spouted bed as three cases of suspensions are considered. The effects of particle size, density, and cohesiveness and also fluid velocity pattern, density, and viscosity on the behavior of suspension are studied. Stokesian

dynamics method has been used in the calculation of hydrodynamic interactions of particles.

The simulation method is very important for the following reasons. Firstly, simulations provide a mean to study the effect of each parameter as for example Stokes number, pattern of fluid motion, and type of interactions between particles, on the behavior of suspensions. Secondly, simulations provide a better qualitative understanding of the physics determining the behavior. Thirdly, the validity of the continuum-type theories can be examined, and lastly, the time and money used in building the experimental settings and operating the experiment are saved. Of course, simulations cannot replace experiments; they can however increase considerably their efficiency.

The simulation of a real fluidized bed is complex and is beyond the power of current computers. We have used the following simplifying assumptions.

1) The chemical reactions between particles are neglected.
2) Particles are spherical and they are all of the same size.
3) The collisions between particles are elastic.
4) The diameter of particles is so large that Brownian forces can be neglected.
5) In order to neglect inertia terms in the Navier-Stokes equations, the diameter of a particle is chosen between 1 – 70 μm's.
6) A two-dimensional fluidized bed is considered that is particles have 2-D velocities.

7) Only a finite number of particles located in an imaginary cell are considered.

8) To account for the particles entering the cell or going out of it and also the interaction of particles with those in outside of the cell, we assume that each cell is surrounded by its replicate in all directions.

9) The simulation is conducted in two cases. In the first case it is assumed that there is no direct (non-hydrodynamic) forces between the particles. In the other case, it is assumed that particles attract each other in a pattern like Lennard-Jones forces and can agglomerate with each other.

CHAPTER 2: SIMULATION METHOD

The motion of each particle in the fluidized bed can be described by the well-known Newton's equation of motion. For one particle in one-dimensional motion, Newton's equation takes the form:

$$m\frac{d}{dt}U = m\frac{d^2}{dt^2}X = F \tag{1}$$

where m, U, X, F, and t are respectively mass of a particle, velocity of a particle, position of a particle, the force exerted on a particle, and time. The same equation can be used for n particles in two-dimensional motion; however the velocity, position, and force should be replaced by $\mathbf{U}$, $\mathbf{X}$, and $\mathbf{F}$, which are column vectors of $2n$ elements each. The coefficient 2 is for two components of plane. That is:

$$m\frac{d}{dt}\mathbf{U}(t) = m\frac{d^2}{dt^2}\mathbf{X}(t) = \mathbf{F} \tag{2}$$

where:

$$\mathbf{U} = \begin{pmatrix} \mathbf{U}^{(1)} \\ \cdot \\ \cdot \\ \cdot \\ \mathbf{U}^{(n)} \end{pmatrix}, \quad \mathbf{X} = \begin{pmatrix} \mathbf{X}^{(1)} \\ \cdot \\ \cdot \\ \cdot \\ \mathbf{X}^{(n)} \end{pmatrix}, \quad \mathbf{F} = \begin{pmatrix} \mathbf{F}^{(1)} \\ \cdot \\ \cdot \\ \cdot \\ \mathbf{F}^{(n)} \end{pmatrix} \tag{3a}$$

$$\mathbf{U}^{(i)} = \begin{pmatrix} u_x^{(i)} \\ u_y^{(i)} \end{pmatrix}, \quad \mathbf{X}^{(i)} = \begin{pmatrix} x_x^{(i)} \\ x_y^{(i)} \end{pmatrix}, \quad \mathbf{F}^{(i)} = \begin{pmatrix} f_x^{(i)} \\ f_y^{(i)} \end{pmatrix} \tag{3b}$$

Equation (2) is made dimensionless by mass of a particle m_p, the terminal velocity of an isolated particle u_t, the radius of a particle a, the time that takes a particle travels its radius at its isolated terminal velocity t_p, and the Stokes drag force applied to a particle moving at its isolated terminal velocity $6\pi\mu a u_t$, where μ is the viscosity of the fluid.

$$\hat{\mathbf{U}} = \frac{\mathbf{U}}{u_t}, \quad \hat{t} = \frac{t}{t_p}, \quad \hat{\mathbf{F}} = \frac{\mathbf{F}}{6\pi\mu a u_t}, \quad \hat{m} = \frac{m}{m_p}, \quad \hat{\mathbf{X}} = \frac{\mathbf{X}}{a} \tag{4}$$

After substituting the variables of equation (2) in terms of their dimensionless values and knowing that $m_p = \frac{4}{3}\pi a^3 \rho_p$ and $\hat{m} = 1$ for monodisperse particles, we reach at this equation: $\frac{2\rho_p a u_t}{9\mu}\frac{d}{d\hat{t}}\hat{\mathbf{U}}(\hat{t}) = \hat{\mathbf{F}}$, where ρ_p is density of a particle. We call the dimensionless coefficient of the above derivative as Stokes number, *St*. It can be rearranged as the ratio of kinetic energy of a particle divided by the drag work over the radius of a particle: $St = \frac{2\rho_p a u_t}{9\mu} = \frac{m_p u_t^2}{6\pi\mu u_t a^2}$ therefore:

$$St\frac{d}{d\hat{t}}\hat{\mathbf{U}}(\hat{t}) = \hat{\mathbf{F}} = \hat{\mathbf{F}}_g + \hat{\mathbf{F}}_{lj} + \hat{\mathbf{F}}_b + \hat{\mathbf{F}}_h \tag{5}$$

The resultant force exerted on particles, $\hat{\mathbf{F}}$, may include the gravity force $\hat{\mathbf{F}}_g$, the attractive Lennard-Jones forces $\hat{\mathbf{F}}_{lj}$, Brownian forces $\hat{\mathbf{F}}_b$, and hydrodynamic forces $\hat{\mathbf{F}}_h$.

2.1 Gravity force

If the positive z axis is taken in the opposite direction of gravity, the gravity force would be equal to:

$$\mathbf{F}_g = -V_p(\rho_p - \rho_f)g\mathbf{E}_z = -m_p\left(\frac{\rho_p - \rho_f}{\rho_p}\right)g\mathbf{E}_z = -m_p\tilde{g}\mathbf{E}_z \qquad (6)$$

where V_p is volume of a particle, ρ_f is the density of fluid, and $\tilde{g} = \left(\frac{\rho_p - \rho_f}{\rho_p}\right)g$ is the effective gravitational acceleration in the fluid, and

$$\mathbf{E}_z = \begin{pmatrix} \mathbf{E}_z^{(1)} \\ \cdot \\ \cdot \\ \cdot \\ \mathbf{E}_z^{(n)} \end{pmatrix} \quad \text{and} \quad \mathbf{E}_z^{(i)} = \begin{pmatrix} 0 \\ 1 \end{pmatrix} \qquad (7)$$

When a particle falls in a fluid at its terminal velocity, the drag force is equal to its weight, that is: $m_p\tilde{g} = 6\pi\mu a u_t$. Therefore, the dimension less form of gravity force is:

$$\hat{\mathbf{F}}_g = -\mathbf{E}_z \qquad (8)$$

2.2 Periodic boundary condition

The amount of calculations in the simulation is proportional to the third power of number of particles, "Press (1988)"; hence, it is only possible to keep track of the motion of only a limited number of particles. We consider 105 particles in an imaginary cell in the midst of a fluidized bed. However, considering a cell of particles by its own is not

comprehensive for two reasons. First, particles can cross the cell and this causes that after a while all the considered particles go out of the cell. Second, particles interact with each other and we need information about the positions of particles surrounding the cell to determine the correct value of inter particle forces. There is a method, called method of periodic boundary conditions, which eliminates these problems by assuming that the cell is surrounded by its replicates in all directions of space. This method in two dimensions is shown in Figure 2.1. In this model when a particle leaves from one side of a cell, its replicate in the cell situated in the opposite side of the cell enters it.

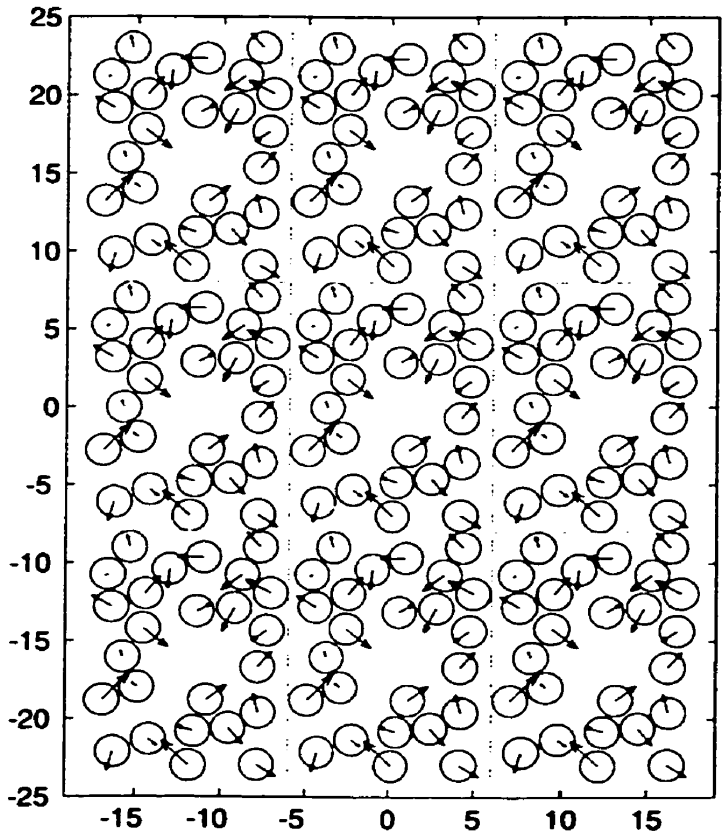

Figure 2.1 Periodic boundary condition

2.3 Direct inter particle force

We include the direct inter particle forces $\hat{\mathbf{F}}_{ij}$, in the form of Lennard-Jones forces, " Atkins (1990) ". The Lennard-Jones potential has the following form:

$$V_{ij} = \frac{a}{S^m} - \frac{b}{S^n} \tag{9}$$

where a, b, m, and n are constants and S is the separation between surfaces of two particles. The values of n and m are generally equal to 6 and two times of n respectively. The inter particle Lennard-Jones force is the derivative of the potential with respect to separation as shown in Figures (2.1) and (2.2).

$$F_{ij} = \frac{d}{dS} V_{ij} = -\frac{am}{S^{m+1}} + \frac{bn}{S^{n+1}} \tag{10}$$

The particles attract each other when they are far from each other but they repel each other when they get too close to each other. We neglect the repulsive Lennard-Jones forces, since theses forces are already taken into account by lubrication force, coming from the thin layer of fluid between two particles, and Hooke's force which prevent two collided particles from overlapping.

In order to get the resultant Lennard-Jones force applied to each particle, we first find the neighbours of each particle and then add the force that each neighbouring particle applies on it.

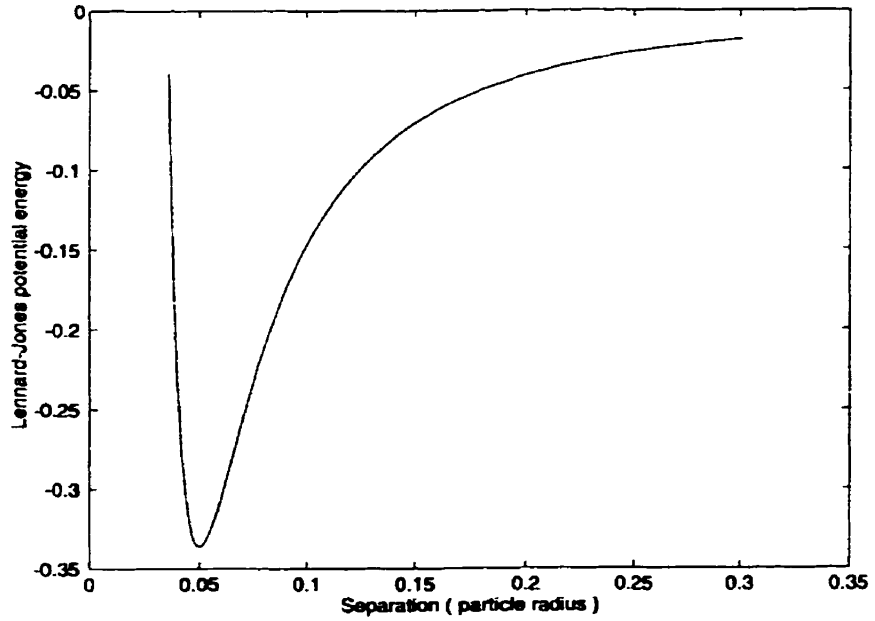

Figure 2.2 Lennard-Jones Potential

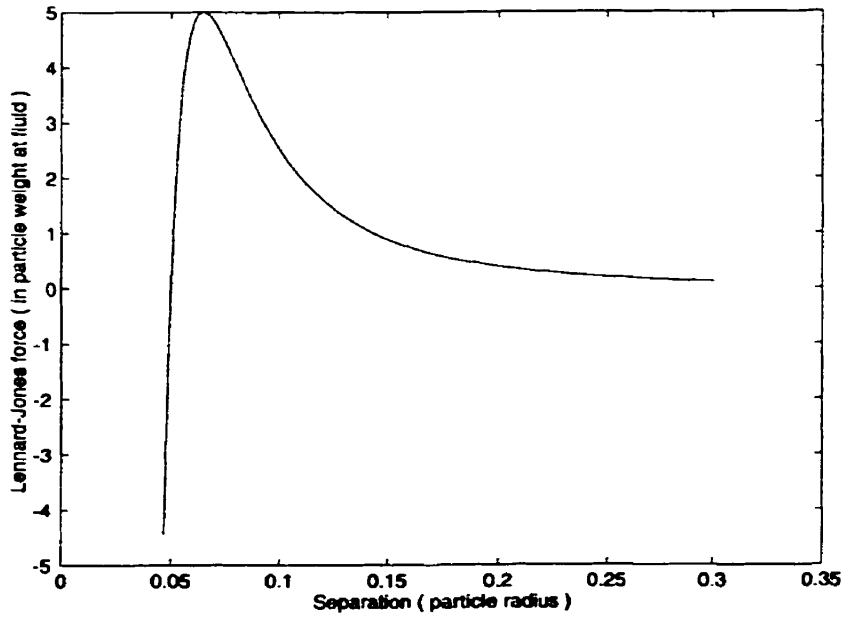

Figure 2.3 Lennard-Jones force between two particles

The Lennard-Jones force is effective in a very narrow distance. However, the time step in our simulation, in which the new positions of particles are calculated, is so large that particles travel farther than Lennard-Jones effective distance. We have chosen the exponents of m and n equal to 4 and 2 respectively in order to compensate the effect of large time step. The values of a and b constants are calculated by determining the maximum attractive force between two particles, $F_{\max}$, and the separation in which there is no force between two particles and the Lennard-Jones potential is at its minimum value, S_{F0}:

$$F_{lj} = \frac{d}{dS} V_{lj} = 0 \qquad \Rightarrow \qquad S_{F0} = \left(\frac{am}{bn}\right)^{1/(m-n)} \tag{11}$$

This is the separation at which the direction of force changes.

$$\frac{d}{dS} F_{lj} = \frac{am(m+1)}{S^{m+2}} - \frac{bn(n+1)}{S^{n+2}} = 0 \qquad \Rightarrow \qquad S_{F\,Max} = \left(\frac{am(m+1)}{bn(n+1)}\right)^{1/(m-n)} \tag{12}$$

This is the separation at which the attractive force is at its maximum value.

$$F\left(S_{F\,Max}\right) = F_{\max} \tag{13}$$

By solving equations (11) and (13) simultaneously, the following expression for the constants of a and b can be obtained:

$$a = \frac{n+1}{m(m-n)} F_{\max} S_{F0}^{m+1} \left(\frac{m+1}{n+1}\right)^{m+1/m-n} \tag{14}$$

$$b = \frac{n+1}{n(m-n)} F_{\max} S_{F0}^{n+1} \left(\frac{m+1}{n+1}\right)^{m+1/m-n} \tag{15}$$

If the S_{F0} is taken as 0.05 of particle radius and F_{max} is taken 5 times of particle weight in fluid, which are typical values in our simulation, the graphs (2.1) and (2.2) are obtained.

2.3.1 Deiva's method of describing agglomeration – deagglomeration

The direct inter particle force that was introduced in this section causes particles to attract each other and stick with each other. However, particles have still their own velocities and do not produce an agglomerate with a unique velocity and shape. "Deiva et al. (1988)" have introduced a method describing agglomeration and deagglomeration. In this method, when two body collide with each other with a total kinetic energy less than a threshold, called minimum collision energy Ec_{MIN}, they agglomerate with each other. A bond between colliding particles is produced. The energy of bond is equal to a fraction of the total kinetic energy of colliding particles. This fraction is called cohesivity, ε. Two colliding body deagglomerate if their total kinetic energy is greater than Ec_{MIN}. In this case, the weak cohesive bonds are broken. These weak bonds are those bonds whose commutative sum of bond energies ($\sum BE_{weak}$) is less than or equal to the total kinetic energies (E_{col}) of the impacting bodies. If agglomerate A collides with agglomerate B, agglomerate A is broken to two small agglomerates. The bigger one is called A' and the smaller one is called A''. The same definition is used for agglomerate B.

$$A + B \rightarrow A' + A'' + B' + B''$$

The disadvantage of this method is that it is based on two false assumptions to calculate the velocities of A', A'', B', and B''. It assumes that the velocities of A'' and B'' is equal to A and B respectively. It also assumes that the fraction of the total kinetic energy available for motion of A before deagglomeration is equal to the fraction of the total kinetic energy available to it (i.e, A') after deagglomeration.

2.4 Brownian force

When the size of particles moving in the air is less than 16 μm, they are subjected to Brownian motion because of the impact of the fluid molecules," Perry (1997) ". For particles finer than 0.1 μm, this random motion is far greater in magnitude than any directed particle motion due to gravitational settling. The criterion for inclusion of Brownian forces is the magnitude of Peclet dimensionless number, which is defined as the ratio of the drag work of a settling particle over the distance of its radius to its thermal energy.

$$Pe = \frac{6\pi\mu a^2 u_t}{k_B T} \tag{16}$$

where k_B is the Boltzmann's constant and T is the absolute temperature. The Brownian force in our simulation is neglected because Pe number is much greater than one.

2.5 Hydrodynamic forces

The hydrodynamic forces can be derived from Navier-Stokes equations of motion along with mass continuity equation.

$$\rho \frac{Dv_j}{Dt} = -\rho g \frac{\partial h}{\partial x_j} - \frac{\partial p}{\partial x_j} + \mu \frac{\partial}{\partial x_i}\left(\frac{\partial v_j}{\partial x_i}\right) \tag{17}$$

$$\frac{\partial \rho}{\partial t} + \frac{\partial}{\partial x_i}(\rho v_i) = 0 \tag{18}$$

The air in our case, where the particle velocities are much slower than sound velocity, is considered incompressible. We also consider micro particles whose Reynolds number is much lower than one and as a result, inertia terms in Navier-Stokes equations can be neglected. Therefore, these equations at constant density and viscosity of fluid simplify to Stokes equations of motion and incompressible continuity equation.

$$\rho \frac{\partial v_j}{\partial t} = -\rho g \frac{\partial h}{\partial x_j} - \frac{\partial p}{\partial x_j} + \mu \frac{\partial}{\partial x_i}\left(\frac{\partial v_j}{\partial x_i}\right) \tag{19}$$

$$\frac{\partial}{\partial x_i} v_i = 0 \tag{20}$$

" Happel and Brenner (1986) " have shown that particle velocities, $\mathbf{U}$, are related to the force that they apply on fluid, $\mathbf{F}_p$, by the following linear relations:

$$\hat{\mathbf{F}}_p = -\hat{\mathbf{F}}_h = R(\hat{\mathbf{X}})(\hat{\mathbf{U}} - \hat{\mathbf{u}}^{\infty}) \tag{21}$$

$$\hat{\mathbf{U}} - \hat{\mathbf{u}}^{\infty} = M(\hat{\mathbf{X}})\hat{\mathbf{F}}_p \tag{22}$$

where $\hat{\mathbf{u}}^{\infty}$ is the fluid velocity in absence of particles. The $\hat{\mathbf{F}}_p$, $\hat{\mathbf{U}}$, and $\hat{\mathbf{u}}^{\infty}$ are vectors in a form similar to equation 3. $R(\hat{\mathbf{X}})$ and $M(\hat{\mathbf{X}})$ are called resistance matrix and mobility matrix respectively and they are determined from the positions of particles. If particles motions are restricted in a plane, these square matrices are of $2n$ dimension.

$$R = \begin{pmatrix} R^{1,1} & . & . & . & R^{1,n} \\ . & & & & . \\ . & & & & . \\ . & & & & . \\ R^{n,1} & . & . & . & R^{n,n} \end{pmatrix} \qquad M = \begin{pmatrix} M^{1,1} & . & . & . & M^{1,n} \\ . & & & & . \\ . & & & & . \\ . & & & & . \\ M^{n,1} & . & . & . & M^{n,n} \end{pmatrix} \tag{23}$$

$R^{\alpha,\beta}$ and $M^{\alpha,\beta}$ are dyadic or two-dimensional tensors in a plane and represent the interaction between particles α and β . That is:

$$R^{\alpha,\beta} = \begin{pmatrix} R_{1,1}^{\alpha,\beta} & R_{1,2}^{\alpha,\beta} \\ R_{2,1}^{\alpha,\beta} & R_{2,2}^{\alpha,\beta} \end{pmatrix}, \qquad M^{\alpha,\beta} = \begin{pmatrix} M_{1,1}^{\alpha,\beta} & M_{1,2}^{\alpha,\beta} \\ M_{2,1}^{\alpha,\beta} & M_{2,2}^{\alpha,\beta} \end{pmatrix} \tag{24}$$

In equation (21) $\hat{\mathbf{F}}_h = -\hat{\mathbf{F}}_p$ because it is assumed that the accelerations of particles are negligible.

" Durlofsky and Brady (1987) " have shown that it is convenient to calculate the resistance matrix in two cases accounting for far-field interactions and near-field interactions and then summing them together. In this way equations converge rapidly and singularity is avoided. The far-field many body interactions are more easily incorporated in mobility formulation and it is described in appendix 1.1. Once the mobility matrix,

M^{∞}, is constructed, it is inverted to yield a far-field approximation to the overall resistance matrix.

The near-field contribution is mainly due to interactions between two adjacent particles. To construct R_{2B} , all the neighboring particles, for example β, around a given particle, for example α, are identified and then related $R_{2B}^{\alpha\alpha}$, $R_{2B}^{\alpha\beta}$, $R_{2B}^{\beta\alpha}$, $R_{2B}^{\beta\beta}$ tensors for (α,β) pair are calculated and added to the corresponding tensors of the R_{2B} resistance matrix. The construction of R_{2B} is described in appendix 1.2. Two-body resistance matrix, R_{2B}, includes not only near-field two-body interactions but also far-field two-body interactions which have already been calculated as part of far-field many-body resistance matrix, $R^{\infty} = (M^{\infty})^{-1}$. In order not to include far-field two-body interactions twice, we should subtract far-field two-body resistance matrix, R_{2B}^{∞} , from the summation of $(M^{\infty})^{-1} + R_{2B}$. The relations for far-field two-body interactions are available in mobility formulation: therefore for constructing R_{2B}^{∞}, as described in appendix 1.3 , we first calculate the mobility functions of $x_{i,j}^{a}, y_{i,j}^{a}$ for all the particle pairs that were used in the calculation of R_{2B}. Then for each pair, the resistance functions of $X_{i,j}^{A}, Y_{i,j}^{A}$ are calculated from mobility functions and then $R_{2B}^{\alpha\alpha,\infty}$, $R_{2B}^{\alpha\beta,\infty}$, $R_{2B}^{\beta\alpha,\infty}$, $R_{2B}^{\beta\beta,\infty}$ tensors are calculated and added to the corresponding terms of R_{2B}^{∞} resistance matrix. The summary of above explanation is:

$$R = (M^{\infty})^{-1} + R_{2B} - R_{2B}^{\infty} \qquad (25)$$

2.5.1 Fixed particles

When there are fixed particles in the cell, we would have the following relation between force and velocity:

$$\begin{pmatrix} \mathbf{F}_m \\ \mathbf{F}_f \end{pmatrix} = \begin{pmatrix} \mathbf{R}_{mm} & \mathbf{R}_{mf} \\ \mathbf{R}_{fm} & \mathbf{R}_{ff} \end{pmatrix} \begin{pmatrix} \mathbf{U}_m - \mathbf{u}_m^{\infty} \\ \mathbf{U}_f - \mathbf{u}_f^{\infty} \end{pmatrix} \tag{51}$$

In this equation the force, velocity, and resistance tensors related to mobile particles are placed at top left of the vector or matrix and are subscribed by m. The subscript f is used for fixed particles. $\mathbf{u}_f$ is zero therefore we have:

$$\mathbf{F}_m = \mathbf{R}_{mm}\left(\mathbf{U}_m - \mathbf{u}_m^{\infty}\right) - \mathbf{R}_{mf}\mathbf{u}_f^{\infty} \quad \Rightarrow \quad \mathbf{U}_m = \mathbf{u}_m^{\infty} + \mathbf{R}_{mm}^{-1}\left(\mathbf{F}_m + \mathbf{R}_{mf}\mathbf{u}_f^{\infty}\right) \tag{52}$$

$\mathbf{F}_m$ include gravity force and direct inter particle forces.

2.6 Elastic collisions

It is assumed that collisions between particles are elastic. That means two colliding particles only exchange kinetic energy and kinetic energy is not transferred to other forms of energy. To determine the velocities of two particles after collision, we make use of conservation of kinetic energy and conservation of momentum. When two particles move toward each other in the same direction that connects the centers of the two particles, the conservation laws are:

$$\begin{cases} \frac{1}{2}m_A v_{A1}^2 + \frac{1}{2}m_B v_{B1}^2 = \frac{1}{2}m_A v_{A2}^2 + \frac{1}{2}m_B v_{B2}^2 \\ m_A v_{A1} + m_B v_{B1} = m_A v_{A2} + m_B v_{B2} \end{cases} \tag{53a,b}$$

For mono disperse particles, in which $m_A = m_B$, these equations simplify to:

$$\begin{cases} v_{B2} = v_{A1} \\ v_{A2} = v_{B1} \end{cases} \tag{54a.b}$$

When the velocities of particles are not in the direction of particle center-to-center line, the velocities of each particle should be decomposed in two components in directions of particle center-to-center direction and a direction normal to this direction. Only the components of particle velocities that are in center-to-center direction are exchanged. The results are:

$$\begin{aligned} v_{Ax2} &= v_{Ax1} - \frac{r_x}{r^2}B \\ v_{Ay2} &= v_{Ay1} - \frac{r_y}{r^2}B \\ v_{Bx2} &= v_{Bx1} + \frac{r_x}{r^2}B \\ v_{By2} &= v_{By1} + \frac{r_y}{r^2}B \end{aligned} \tag{55}$$

where

$$B = (v_{Ax1} - v_{Bx1})r_x + (v_{Ay1} - v_{By1})r_y$$
$$r = \sqrt{r_x^2 + r_y^2}$$

and when a particle collides with a fixed particle, the new velocities of the particle are:

$$v_{Ar2} = v_{Ar1} - 2\frac{r_x}{r^2}B$$
$$v_{Av2} = v_{Av1} - 2\frac{r_y}{r^2}B \qquad (56)$$

2.7 Simulation procedure

The values of particle radius, particle density, fluid density, fluid viscosity, and acceleration due to gravity are taken and Stokes number is calculated. After replacing gravity force, Lennard-Jones force and hydrodynamic force in equation (5), we would have:

$$St\frac{d}{d\hat{t}}\hat{\mathbf{U}}(\hat{t}) = -R(\hat{\mathbf{X}}(\hat{t}))\left[\hat{\mathbf{U}}(\hat{t}) - \hat{\mathbf{u}}^{\infty}\right] + \hat{\mathbf{F}}_g + \hat{\mathbf{F}}_{lj} \qquad (57)$$

This equation should be integrated numerically. To increase efficiency, we assume that velocity is the sum of terminal steady velocity $\hat{\mathbf{U}}_0$, and a time varying velocity of $\hat{\mathbf{U}}_1(\hat{t})$.

$$\hat{\mathbf{U}}(\hat{t}) = \hat{\mathbf{U}}_0 + \hat{\mathbf{U}}_1(\hat{t}) \qquad (58)$$

$\hat{\mathbf{U}}_0$ is calculated from equation (52) and $\hat{\mathbf{U}}_1(\hat{t})$ is determined from:

$$St\frac{d}{d\hat{t}}\hat{\mathbf{U}}_1(\hat{t}) = -R(\hat{\mathbf{X}}(\hat{t}))\hat{\mathbf{U}}_1(\hat{t}) \qquad (59)$$

Time interval of integration is taken small enough that it is possible to approximate the resistance matrix equal to unit matrix. With this approximation we have:

$$\left.\begin{aligned}\hat{\mathbf{U}}_1(\hat{t}) &= \hat{\mathbf{U}}_1(0)\exp\left(\frac{-\hat{t}}{St}\right)\\ \hat{\mathbf{U}}(0) &= \hat{\mathbf{U}}_0 + \hat{\mathbf{U}}_1(0)\end{aligned}\right\} \quad \Rightarrow \quad \hat{\mathbf{U}}(\hat{t}) = \hat{\mathbf{U}}_0 + \left[\hat{\mathbf{U}}(0) - \hat{\mathbf{U}}_0\right]\exp\left(\frac{-\hat{t}}{St}\right) \tag{60}$$

In the above equations, $\hat{\mathbf{U}}_1(0)$ is the velocity of particles in the previous time step. Time step is usually taken equal to 0.1 of dimensionless time. Simulations are usually done during 1000 dimensionless time, which is equivalent to 1.7-10 seconds. We use IBM RISC System 6000-37T computer and with this machine it takes nearly 3 days to finish 10000 time steps.

2.8 Order of magnitude of simulation parameters

Stokes number and superficial gas velocity are the parameters used for calculation of hydrodynamic force. Particle Reynolds number and Peclet number determine the validity of Stokesian dynamics method and ignorance of Brownian forces respectively. If we assume:

$\rho_p = 1670$	kg/m^3	$\rho_f = 1.2$	kg/m^3
$g = 9.81$	m/s^2	$\mu = 1.825\times10^{-5}$	kg/m/s
a = 5-30	μm		

Other important parameters are defined below and their domain are shown in Figure 2.4, 2.5, and 2.6:

$$u_t = \frac{m\tilde{g}}{6\pi\mu a} = \frac{2a^2\rho_p\tilde{g}}{9\mu}$$ terminal velocity of an isolated particle

$$F_d = 6\pi\mu a u_t$$ drag force applied to an isolated particle

$$Re_p = \frac{\rho_f a u_t}{\mu}$$ particle Reynolds number

$$Pe = \frac{6\pi\mu a^2 u_t}{k_B T}$$ Peclet number

$$t_r = \frac{m_p u_t}{F_d} = \frac{2\rho_p a^2}{9\mu}$$ relaxation time of particle velocity due to drag force

$$t_p = \frac{a}{u_t} = \frac{9\mu}{2ag(\rho_p - \rho_f)}$$ the time during which a particle passes its radius at its isolated terminal velocity

$$St = \frac{t_r}{t_p} = \frac{2\rho_p a u_t}{9\mu}$$ Stokes number

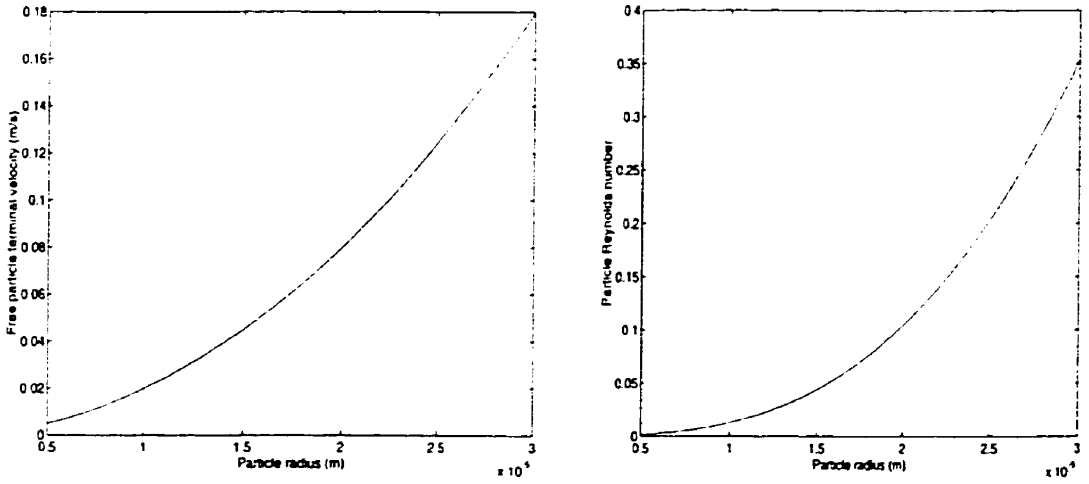

Figure 2.4 Terminal velocity of an isolated article and particle Reynolds number versus particle radius

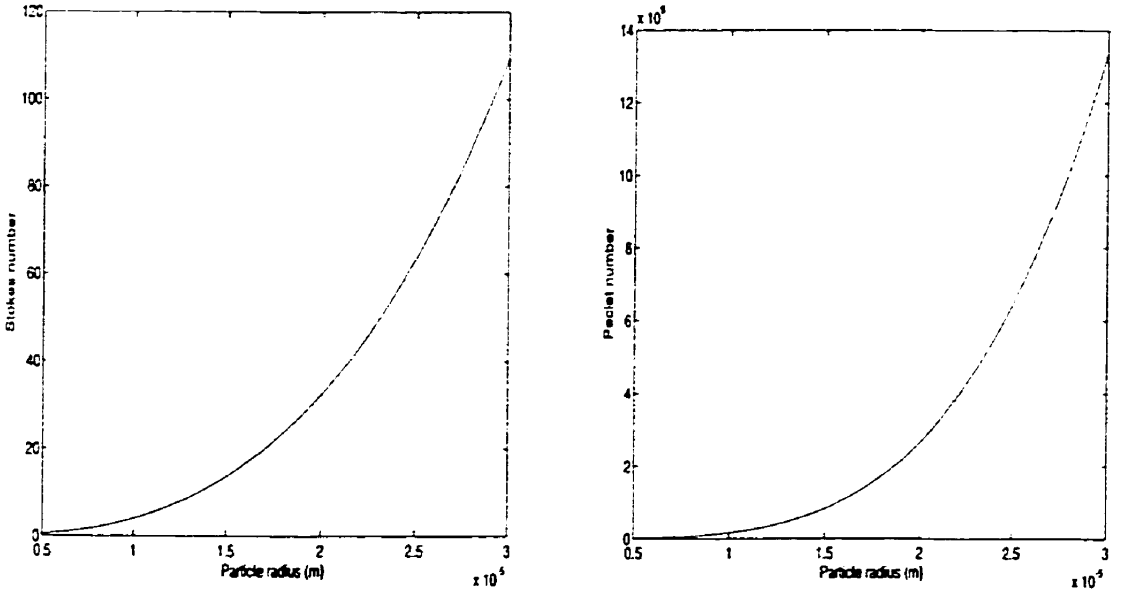

Figure 2.5 Stokes number and Peclet number versus particle radius

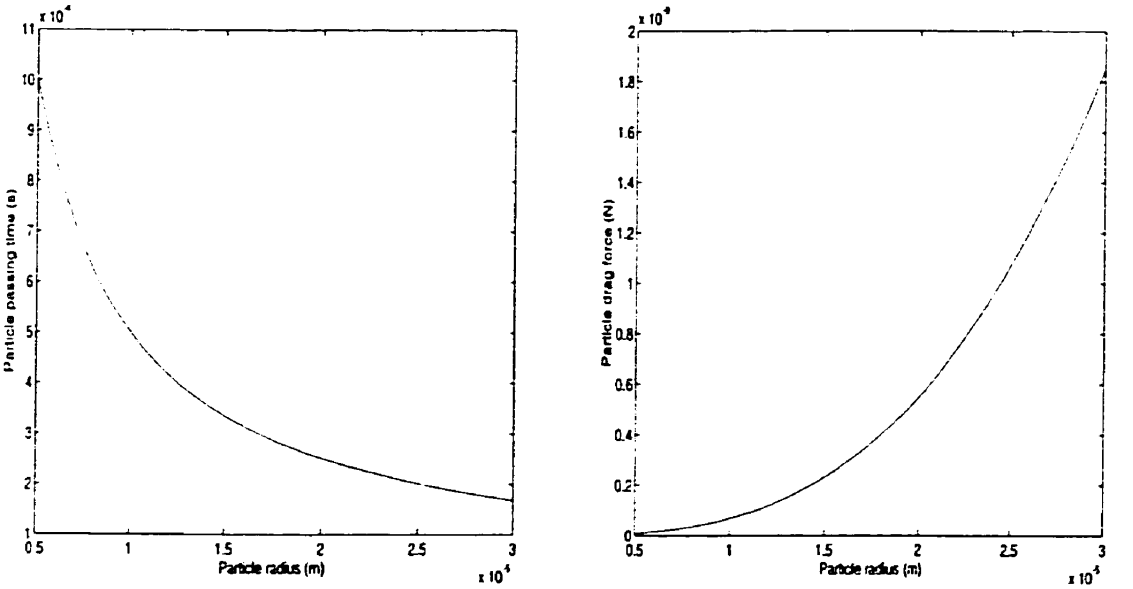

Figure 2.6 Particle passing time and drag force applied on a particle versus particle radius

CHAPTER 3: RESULTS

In this chapter the results of simulation for sedimentation, fluidization with fixed particles, fluidization without fixed particles, spouted bed, and fluidization with mixed particles of cohesive and non-cohesive particles are shown. In appendix 2, the calculated velocities of particles in fast regime fluidized bed are compared with experimental data. Also, the calculated bubble size and bubble rising velocity in bubbling fluidized bed are compared with models and experimental data. In appendix 3, there is supplementary information on this chapter. All the units are dimensionless as defined in previous chapter.

The following parameters are used to quantify the results of simulations:

1) Average volume fraction during the simulation time as a function of cell height.

$$VF(h,h+\Delta h)=\frac{1}{t+1}\sum_{t=0}^{t}\frac{4\pi n_p(h,h+\Delta h)}{6\Delta hW}$$

2) Volume fraction of particles at a given cell height as a function of time

3) Standard deviation of velocities of particles as a function of time

4) Average velocity distribution of particles during the simulation time

$$VD(U,U+\Delta U)=\frac{1}{(t+1)N\Delta U}\sum_{t=0}^{t}n_p(U,U+\Delta U)$$

5) Energy spectrum of particle velocities as a function of frequency

$$E(\omega) = \frac{1}{N}\sum_{\alpha=1}^{N} \tilde{U}^{\alpha}(\omega)\tilde{U}^{\alpha^*}(\omega)$$

$$\text{where } \tilde{U}(\omega) = \int_{-\infty}^{+\infty} e^{-i\omega t} U(t)dt$$

6) Kinetic energy per particle as a function of time

$$E(t) = \frac{1}{N_M}\sum_{\alpha=1}^{N_M} [U^{\alpha}(t)]^2$$

7) Average kinetic energy per particle

$$\bar{E} = \frac{1}{t+1}\sum_{t=0}^{t} E(t)$$

8) Height of center of mass as a function of time

$$h(t) = \frac{1}{t+1}\sum_{\alpha=1}^{N_M} h^{\alpha}(t)$$

9) Average height of center of mass

$$\bar{h} = \frac{1}{t+1}\sum_{t=0}^{t} h(t)$$

10) Standard deviation of kinetic energy per particle

11) Standard deviation of height of center of mass

3.1 Sedimentation

Figure 3.1.1 shows the sequence of simulation of batch sedimentation with 100 non-cohesive particles in a cell with $17.5 \times 2 \times 50$ dimensions. There are five fixed particle at

the bottom of cell to form distributor of the cell. In the lower left frame, particles have initial random positions with zero velocities. Sedimentation of particles is complete in the upper right frame. Fig. 3.1.2 shows that initially particles have equal velocities and the standard deviation of their velocities is zero. Then particles get momentum and get various velocities during collision and their standard deviation reach a maximum value and again decreases as particles settle. Fig. 3.1.3 shows how rapidly particles with different stokes number settle. As stokes number increases, it takes longer that particles reach their final constant volume fraction. Fig. 3.1.4-5 show the velocity distribution of particles at t=60. Most of the particles with St=1 have settled down at this time and their velocity distribution is narrower than those particles with high stokes number. Fig. 3.1.6 shows the kinetic energy per particle at St=10. It shows that at zero time, particles have only potential energy. As the time passes they reach at their maximum kinetic energy and after that the kinetic energy of particles is dissipated through viscous forces. Fig. 3.1.7 shows how the height of center of mass of particles decreases during sedimentation.

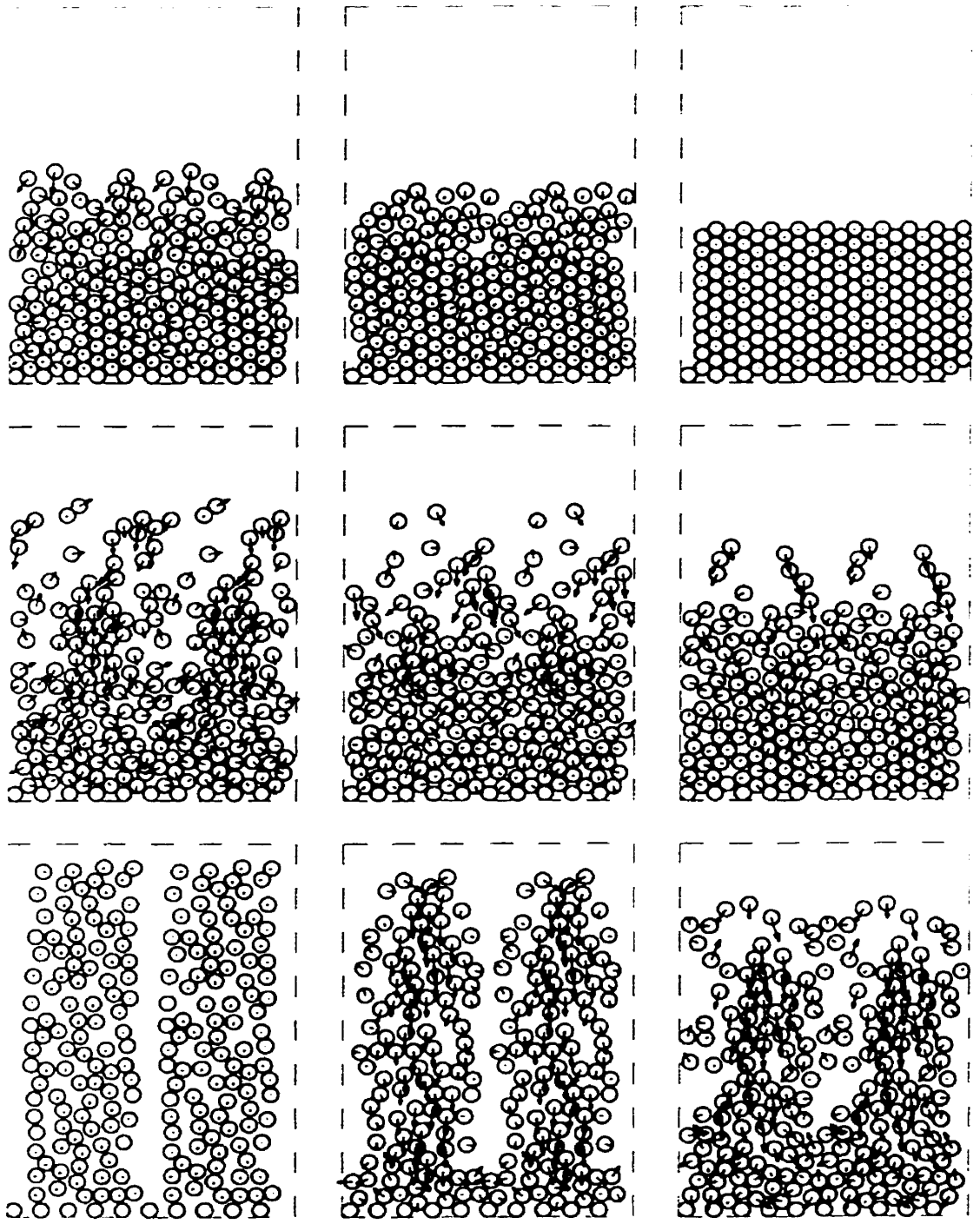

Figure 3.1.1. Sequence of the simulation of sedimentation with non-cohesive particles at St=10. Related times of the frames from lower left to upper right are 0, 10, 20, 30, 40, 50, 60, 70, and 170 in dimensionless units respectively.

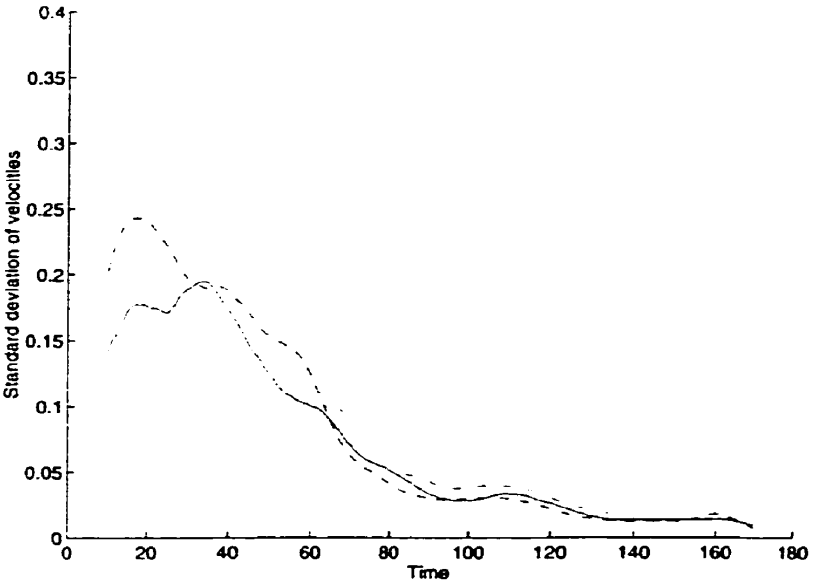

Figure 3.1.2. Standard deviation of velocities of particles in sedimentation at St=10. Solid line is for horizontal component of velocity, dash-dotted line for vertical component of velocity, and dashed line for magnitude of velocity.

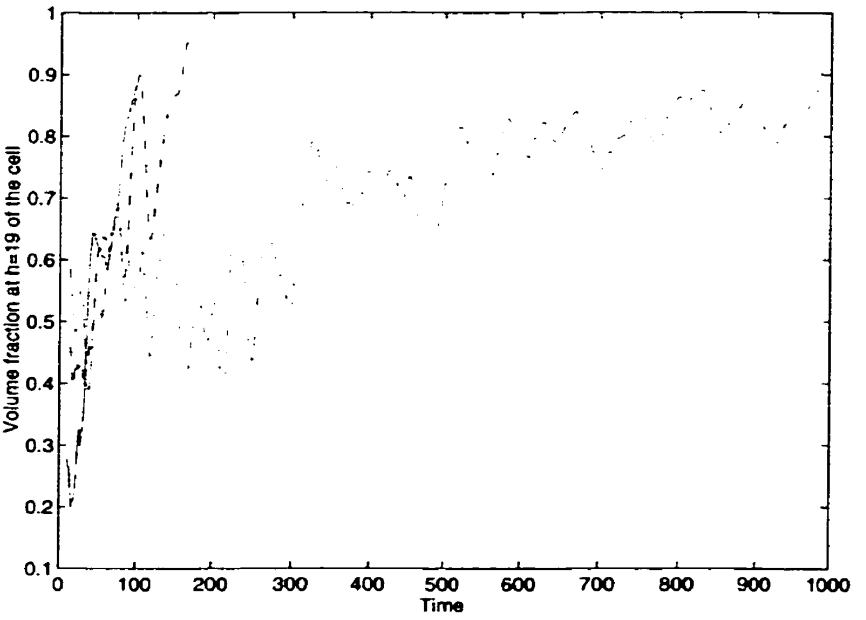

Figure 3.1.3. Volume fraction of particles in sedimentation at h=19 level of the cell. Solid line is for St=1, dash-dotted line for St=10, dashed line for St=100

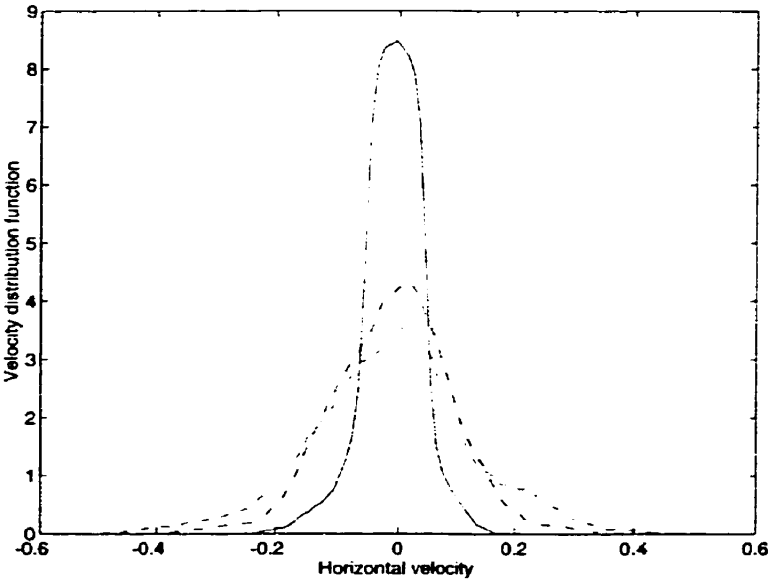

Figure 3.1.4. Velocity distribution of horizontal component of velocities of particles in sedimentation at time=60. Solid line is for St=1, dash-dotted line for St=10, dashed line for St=100

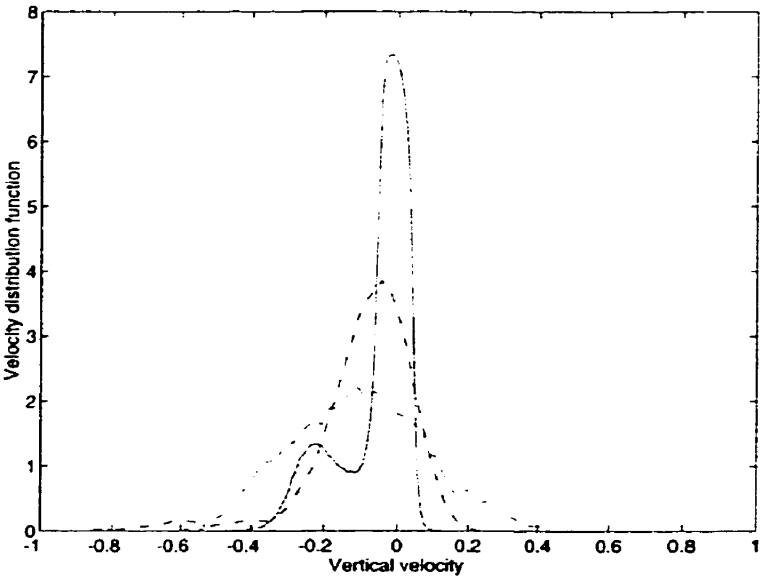

Figure 3.1.5. Velocity distribution of vertical components of velocities of particles in sedimentation at time=60. Solid line is for St=1, dash-dotted line for St=10, dashed line for St=100

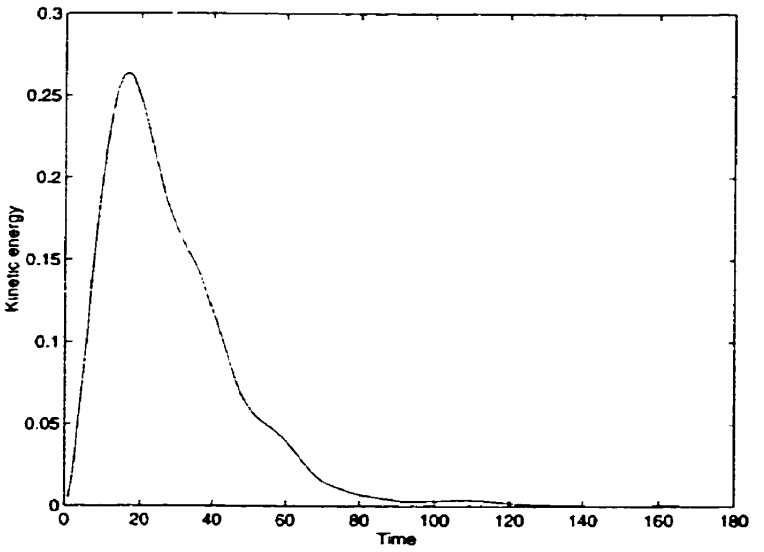

Figure 3.1.6. Kinetic energy per particle in sedimentation at St=10

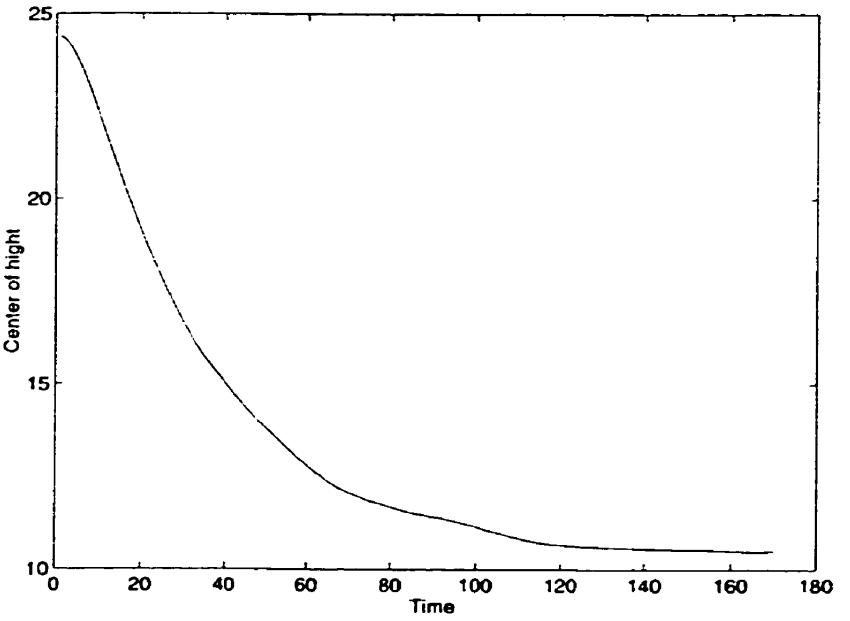

Figure 3.1.7. Height of center of mass of particles in sedimentation at St=10

3.2 Fluidization with fixed particles

Fig. 3.2.1 shows the sequence of simulation of a fluidized bed in channeling phase with 100 particles. Particles with stokes number lower than one fluidize in channeling mode. Fig. 3.2.2 is related to fluidization of particles with St=10. A bubble is developed at the bottom of cell and bursts as it reaches to the surface of the cell. Fig. 3.2.3 shows the average volume fraction of particles during fluidization for different superficial gas velocities. As the gas velocity increases, the volume fraction of particles more steadily decreases from bottom to top of the cell. Fig. 3.2.4 shows the standard deviation of particles. At start up, particles have zero velocity and their standard deviation is zero. It reaches a maximum peak at the beginning instability of fluidization and then it periodically increases when there are bubbles at the cell and decreases when there is no bubble in the cell. It is possible to count the frequency of bubble formation by counting the number of peaks of this graph in a given time interval. Fig. 3.2.5-6 show the velocity distribution of particles in two times, when there is no bubble in the cell and the other time when there is a bubble in the cell. The particles at the bottom of a bubble and in the bubble rise rapidly, while the particle around a bubble go down. This causes that particles have a wider range of velocity distribution at the bubble time. Fig. 3.2.7 shows the volume fraction of particles at h=19 level of the cell with different superficial gas velocities. At u^{*}=0.1 the bed is fixed and volume fraction has a little variations. When u^{*} increases, the volume fraction periodically increases when there is no bubble at the level of measurement and it decreases when a bubble crosses this level. Fig. 3.2.8-9 show

the velocity distribution of particles with different u^{-}. As u^{-} increases, the range of velocity distribution increases. Fig. 3.2.10 shows how the kinetic energy per particle periodically increases when the cell has a bubble. Fig. 3.2.11 shows that the height of center of mass periodically increases when there is a bubble in the cell. Fig. 3.2.12-13 show the role of frequencies of components of the velocities of particles. High frequency is related to colliding particles and the energy of these frequencies exponentially decreases. Fig. 3.2.14 shows that as stokes number increases kinetic energy of particles increases to a maximum value and after that decreases. Fig. 3.2.15 shows that the height of center of mass of particles increases with increase of stokes number. Fig. 3.2.16-17 show that as u^{-} increases, so do the kinetic energy and height of center of mass of particles.

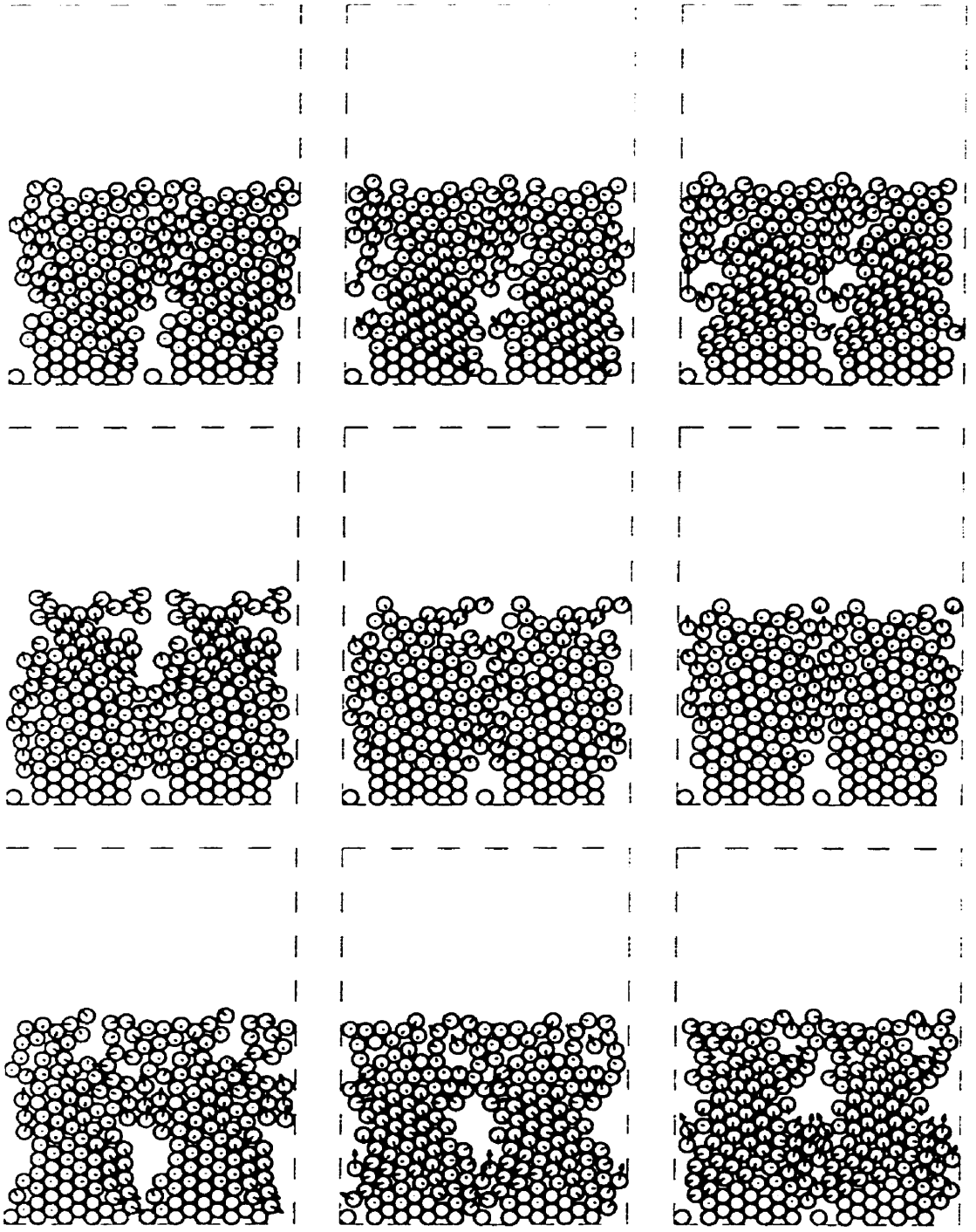

Figure 3.2.1. Sequence of the simulation of fluidization in channeling phase at St=0.5 and u^{∞}=0.15. Related times of the frames from lower left to upper right are 500, 510, 520, 530, 540, 550, 560, 570, and 580 in dimensionless units respectively.

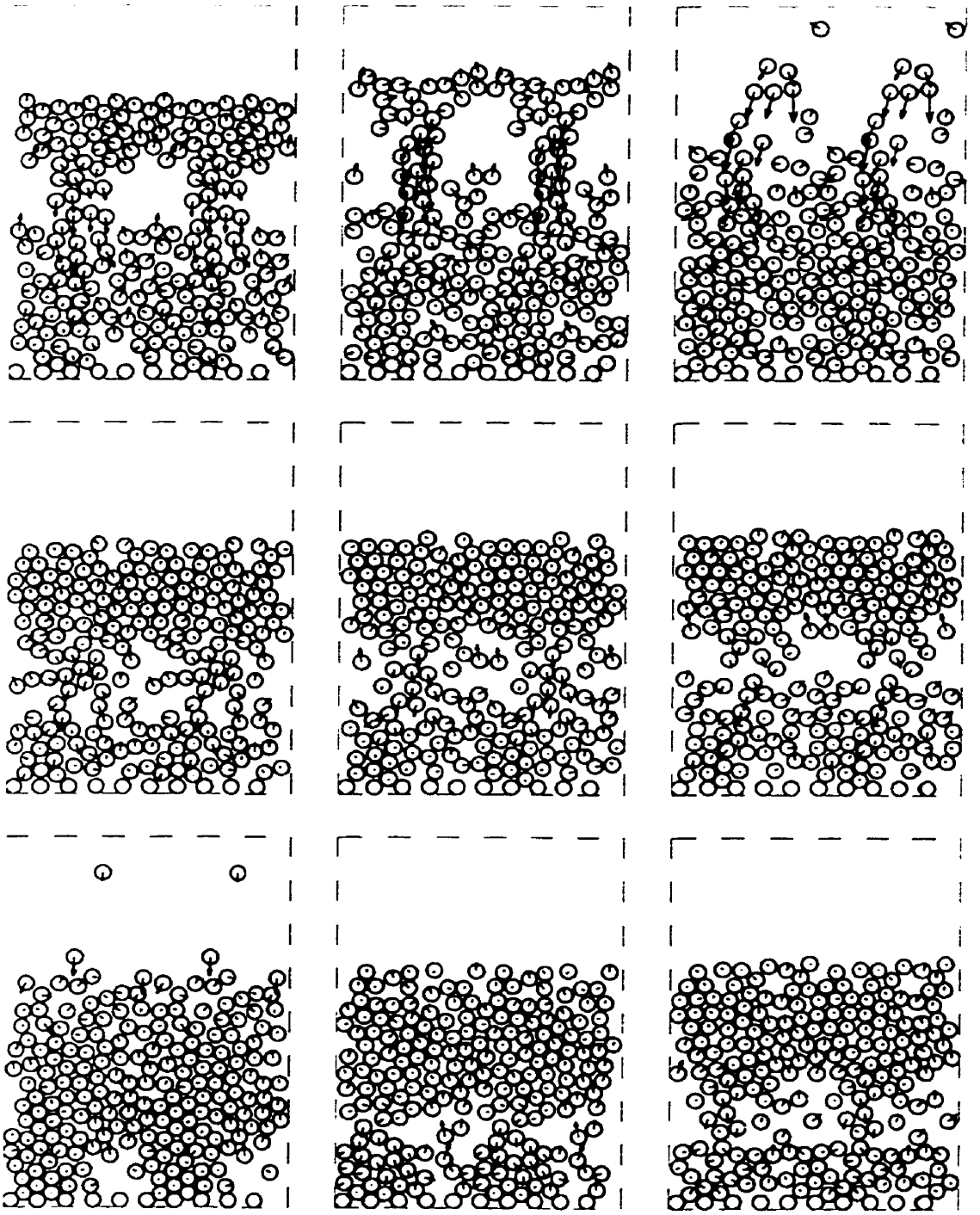

Figure 3.2.. Sequence of the simulation of fluidization in bubbling phase at St=10 and u^{*}=0.20. Related times of the frames from lower left to upper right are 240, 270, 290, 300, 310, 320, 340, 360, and 380 in dimensionless units respectively.

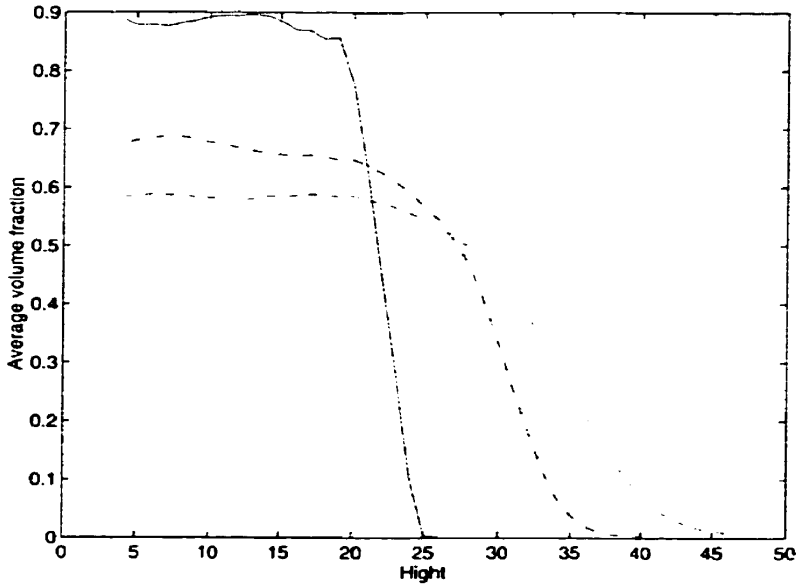

Figure 3.2.3 Average volume fraction of particles along the cell height in fluidization with fixed particles at St=10. Solid line is for u^{∞}=0.1, dash-dotted line for u^{∞}=0.15, dashed line for u^{∞}=0.2, and dotted line for u^{∞}=0.3.

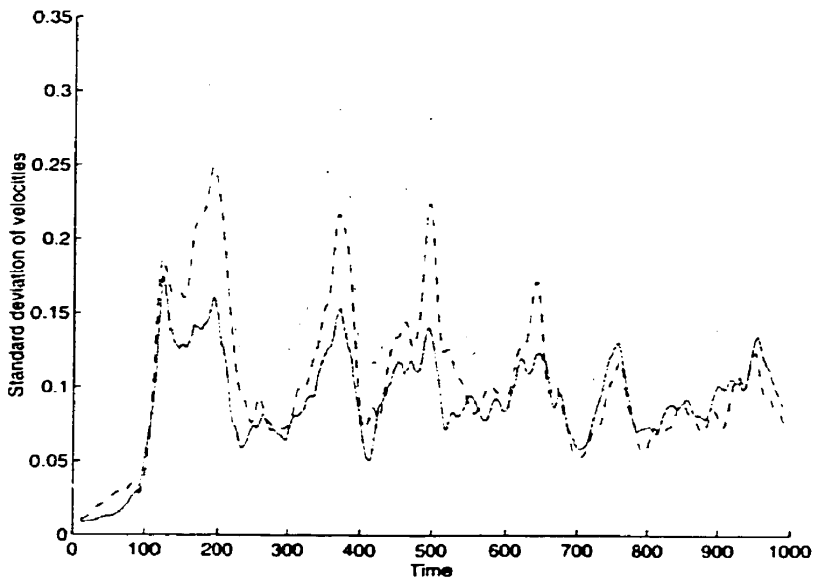

Figure 3.2.4. Standard deviation of particle velocities in fluidization with fixed particles at St=10 and u^{∞}=0.2. Solid line is for horizontal component of velocity, dash-dotted line for vertical component of velocity, and dashed line for magnitude of velocity.

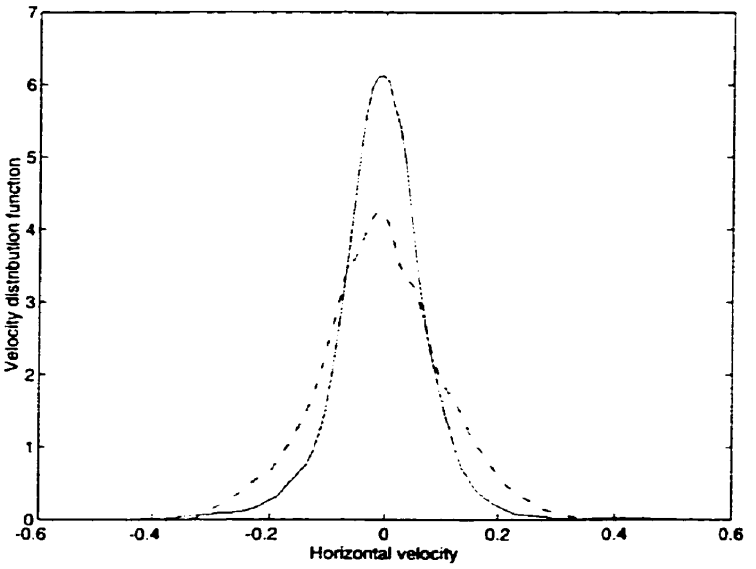

Figure 3.2.5. Velocity distribution of horizontal components of velocities of particles in fluidization with fixed particles at St=10 and u^{∞}=0.2. Solid line is related for the time when there is no bubble, and dash-dotted line is related for the time when there are bubbles in the bed

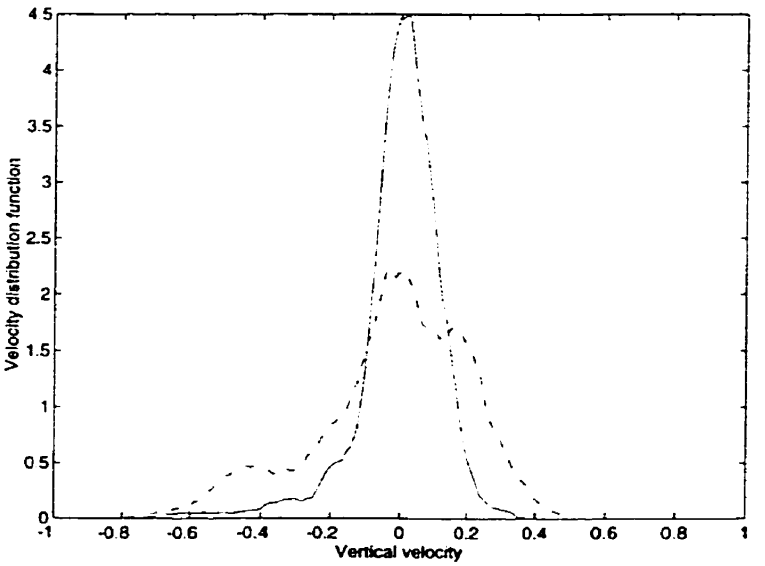

Figure 3.2.6. Velocity distribution of vertical components of velocities of particles in fluidization with fixed particles at St=10 and u^{∞}=0.2. Solid line is related for the time when there is no bubble, and dash-dotted line is related for the time when there are bubbles in the bed

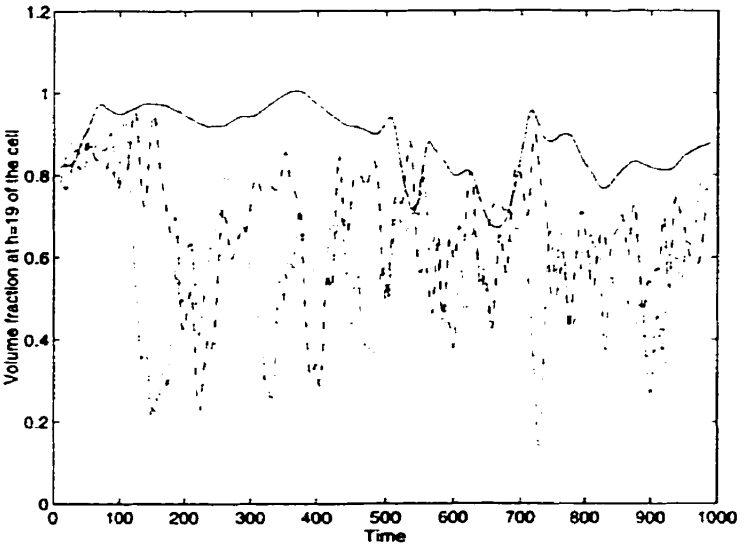

Figure 3.2.7. Volume fraction of particles in fluidization with fixed particles at h=19 level of the cell and St=10. Solid line is for u^{∞}=0.1, dash-dotted line for u^{∞}=0.15, dashed line for u^{∞}=0.2, and dotted line for u^{∞}=0.3.

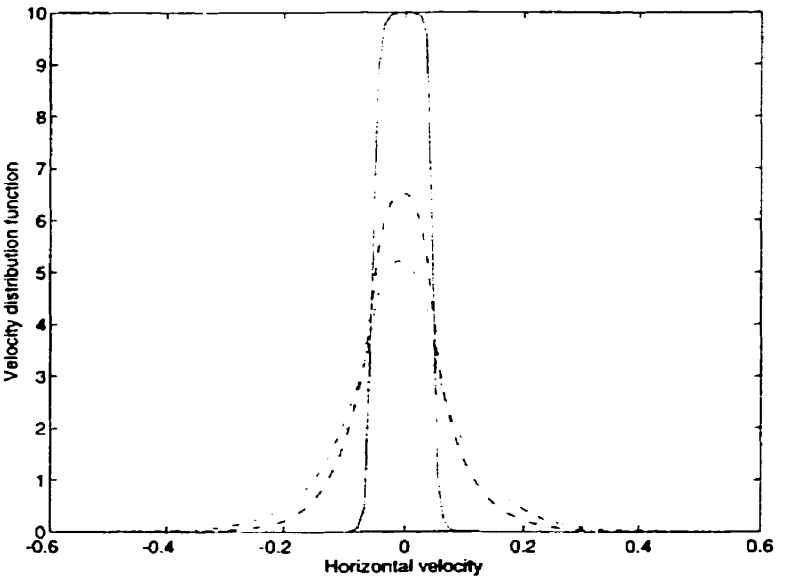

Figure 3.2.8. Velocity distribution of horizontal components of velocities of particles in fluidization with fixed particles at St=10. Solid line is for u^{∞}=0.1, dash-dotted line for u^{∞}=0.15, dashed line for u^{∞}=0.2, and dotted line for u^{∞}=0.3.

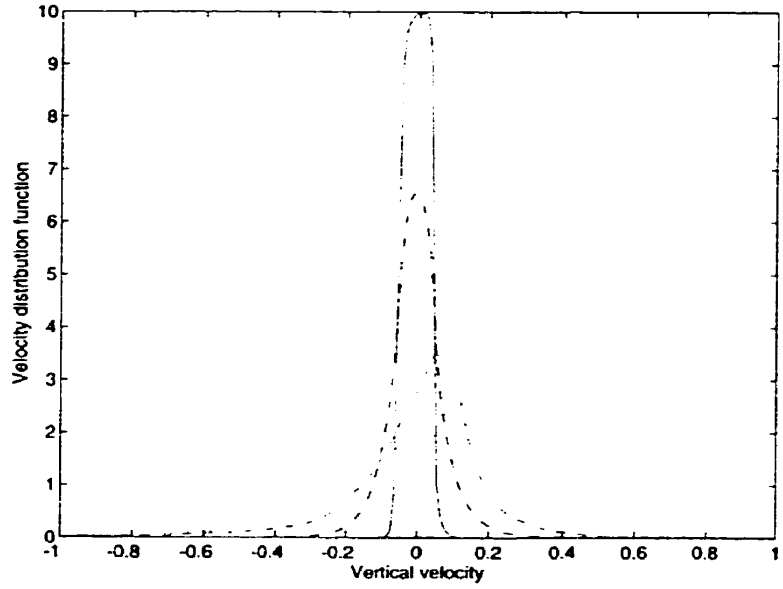

Figure 3.2.9. Velocity distribution of vertical components of velocities of particles in fluidization with fixed particles at St=10. Solid line is for u^{∞}=0.1, dash-dotted line for u^{∞}=0.15, dashed line for u^{∞}=0.2, and dotted line for u^{∞}=0.3.

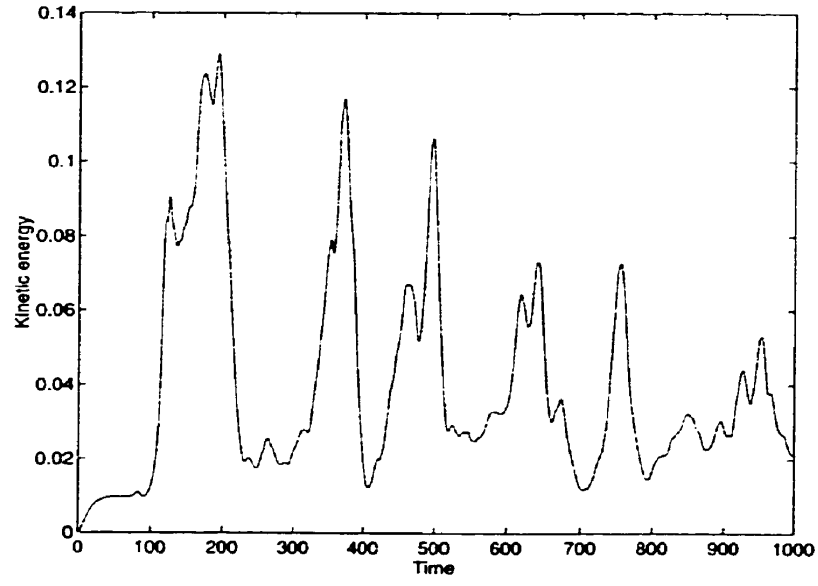

Figure 3.2.10. Kinetic energy per particle in fluidization with fixed particles at St=10 and u^{∞}=0.2.

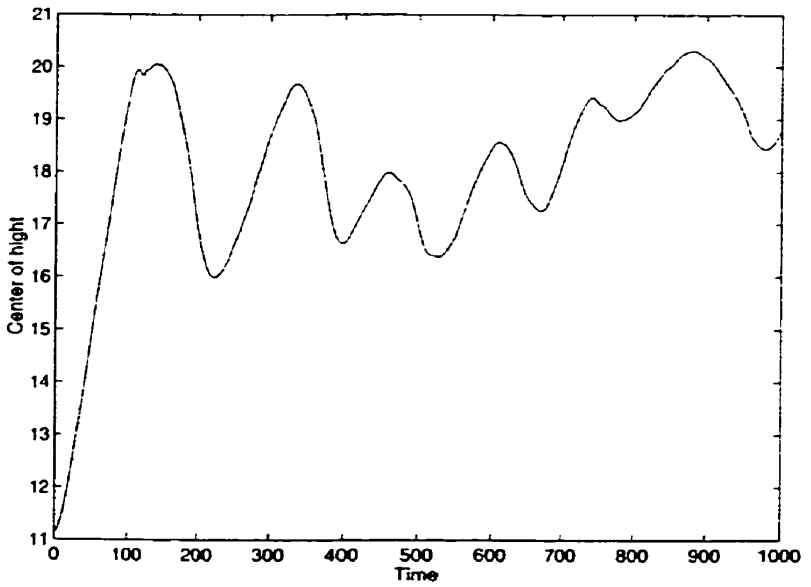

Figure 3.2.11. Height of center of mass of particles in fluidization with fixed particles at St=10 and u^{∞}=0.2.

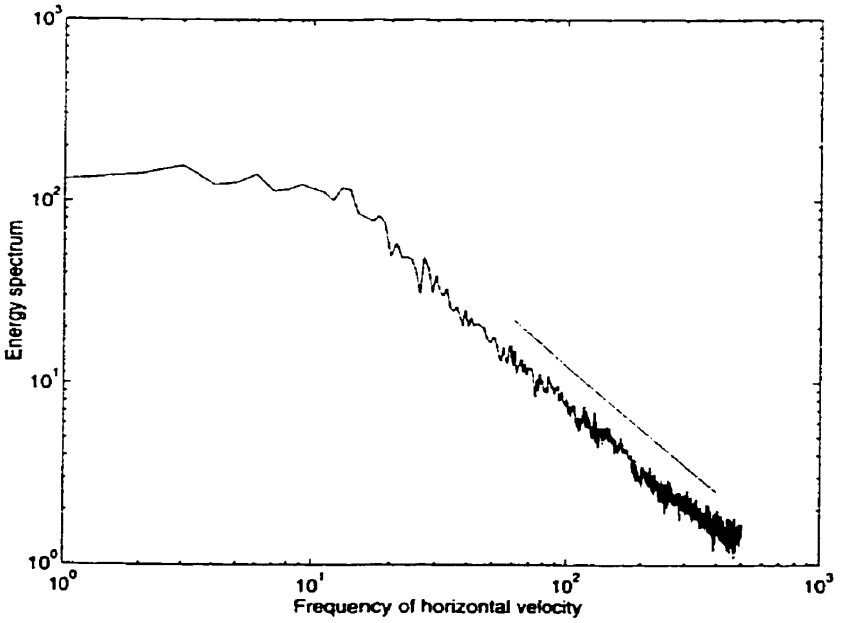

Figure 3.2.12 Energy spectrum of horizontal component of velocity in fluidization with fixed particles at St=10 and u^{∞}=0.2.

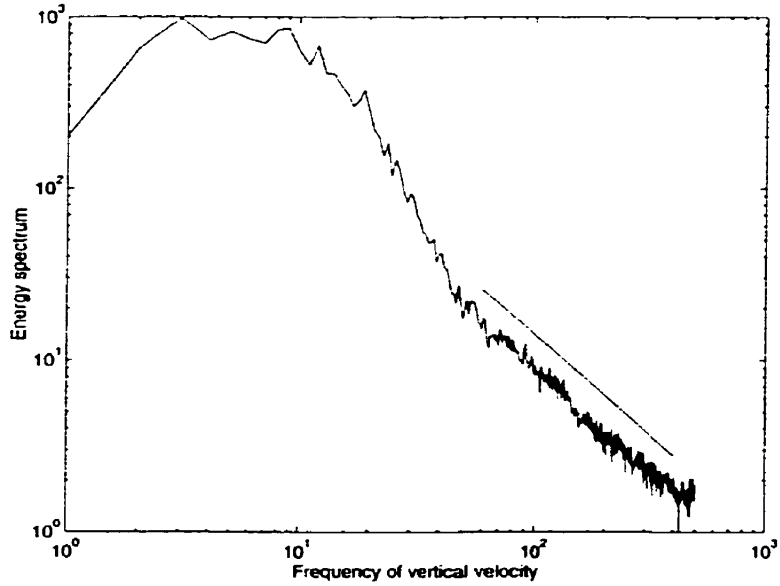

Figure 3.2.13 Energy spectrum of vertical component of velocity in fluidization with fixed particles at St=10 and u^{∞}=0.2.

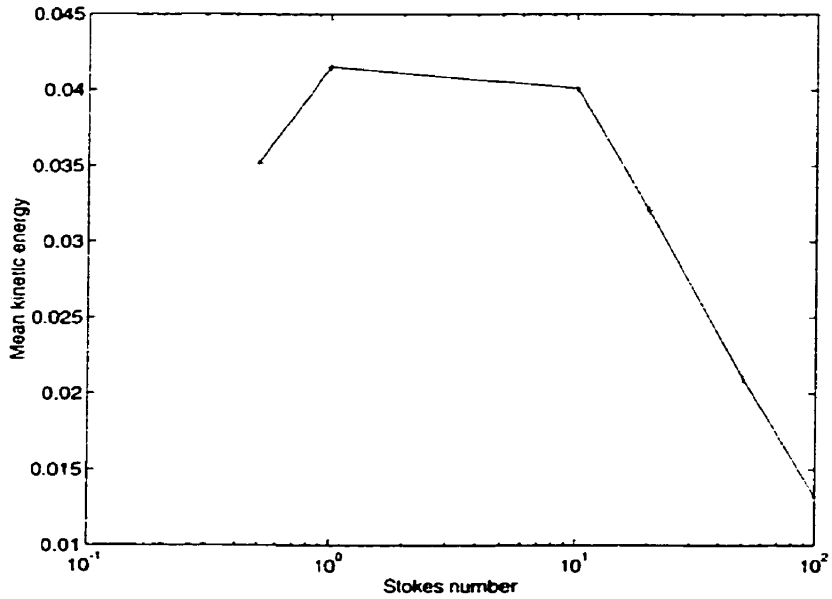

Figure 3.2.14 Mean kinetic energy of particles in fluidization with fixed particles at u^{∞}=0.2

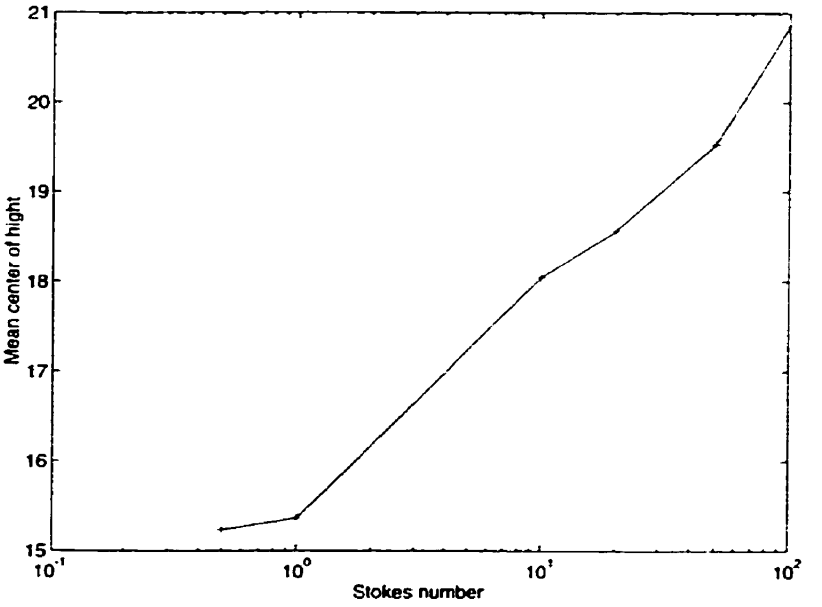

Figure 3.2.15 Mean height of center of mass of particles in fluidization with fixed particles at u^{∞}=0.2

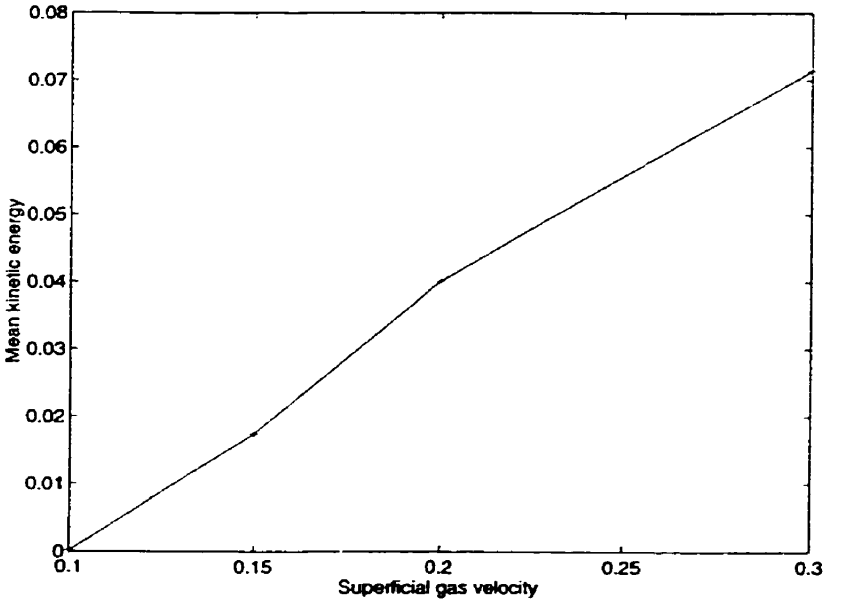

Figure 3.2.16 Mean kinetic energy per particle in fluidization with fixed particles at St=10

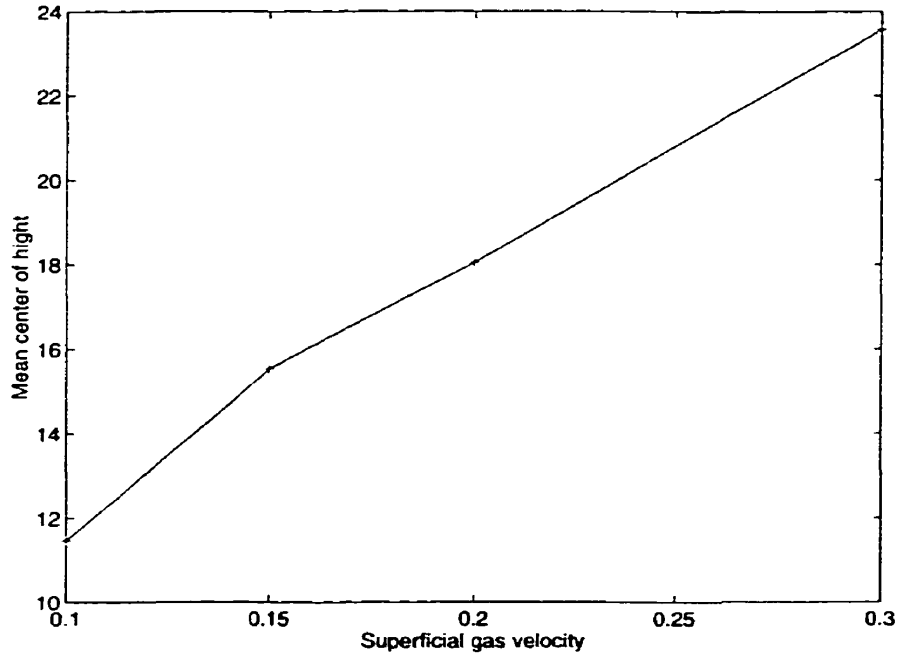

Figure 3.2.17 Mean height of center of mass of particles in fluidization with fixed particles at St=10

3.3 Fluidization without fixed particles

Fig. 3.3.1 shows the sequence of simulation of a fluidized cell without fixed particles and with 100 particles. It is seen that the size of a bubble has increased to the maximum size possible in a cell and the cell is in slugging phase. Fig. 3.3.2 shows that the average volume fraction of particles in a cell is nearly constant because there is always a slug cycling the cell. Fig. 3.3.3 shows that velocity distribution is symmetric in horizontal direction and changes very slightly with u^{*}. Fig. 3.3.4 shows that as u^{*} increases, vertical velocity shifts to right and fewer particles fall in the bed. Fig. 3.3.5 shows that volume fraction of particles at a given level changes periodically depending on the

position of the slug. By counting the number of peaks, the velocity of the slug is determined to be 0.26 in dimensionless units in comparison to superficial gas velocity, which is 0.3. Fig. 3.3.6 shows that standard deviation of velocity has a very low variations because there is always one slug cycling the cell with constant size and velocity Fig. 3.3.7 shows the variation of height of center of mass with the passage of slug.

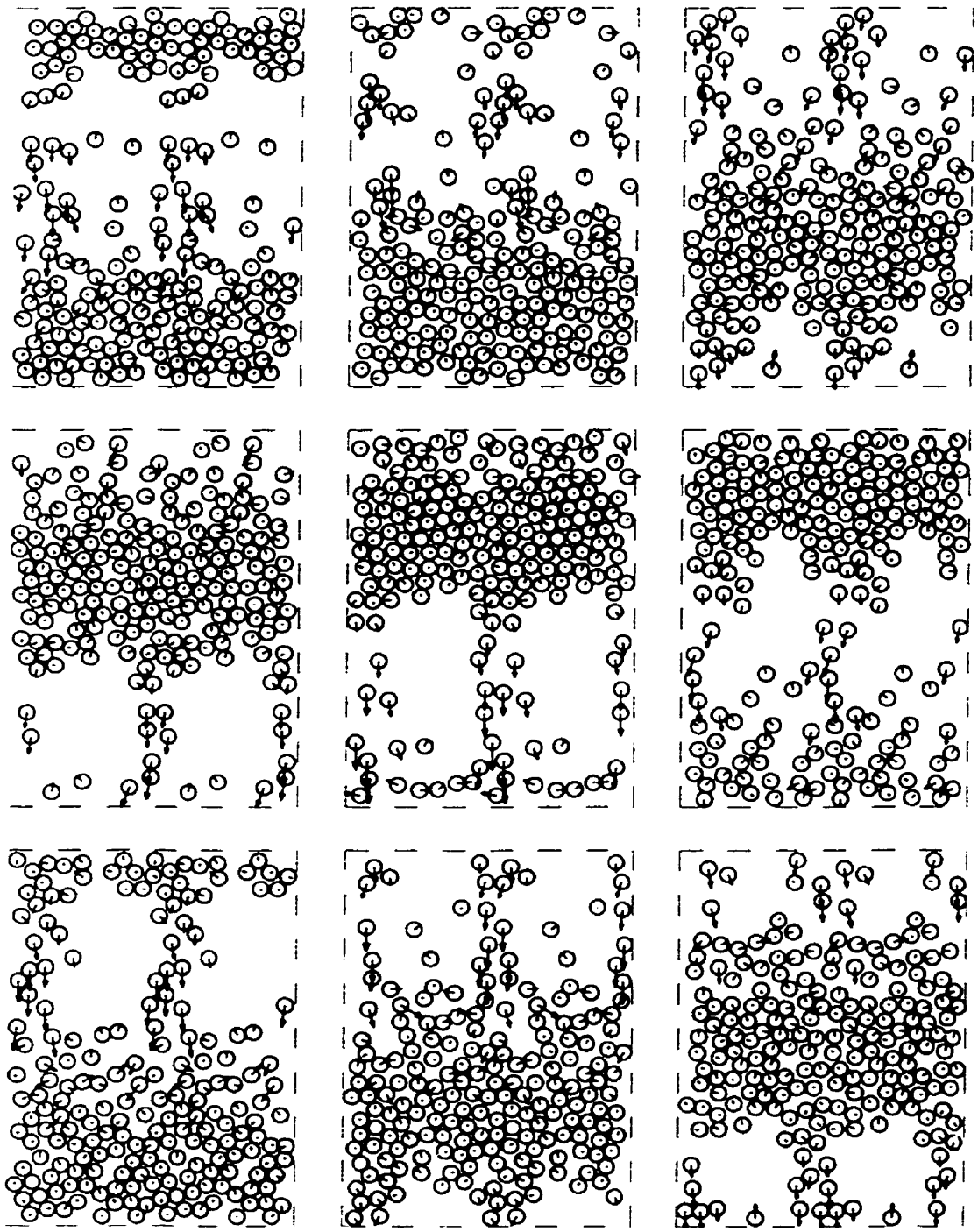

Figure 3.3.1. Sequence of the simulation of fluidization without fixed particles at St=15 u^{∞}=0.3. Related times of the frames from lower left to upper right are 500, 530, 560, 590, 620, 650, 680, 710, and 740 in dimensionless units respectively.

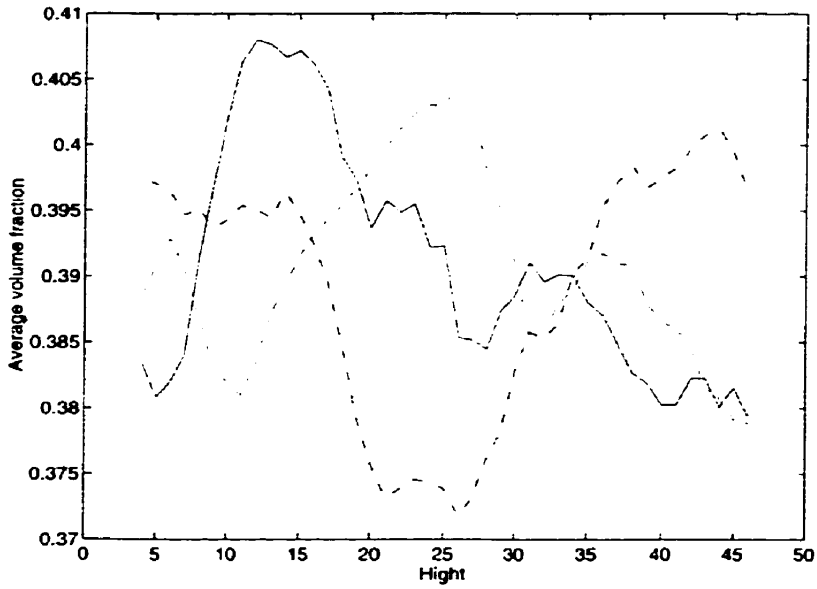

Figure 3.3.2 Average volume fraction of particles along the cell height in fluidization without fixed particles at St=15. Solid line is for u^{∞}=0.3, dash-dotted line for u^{∞}=0.5, and dashed line for u^{∞}=0.6.

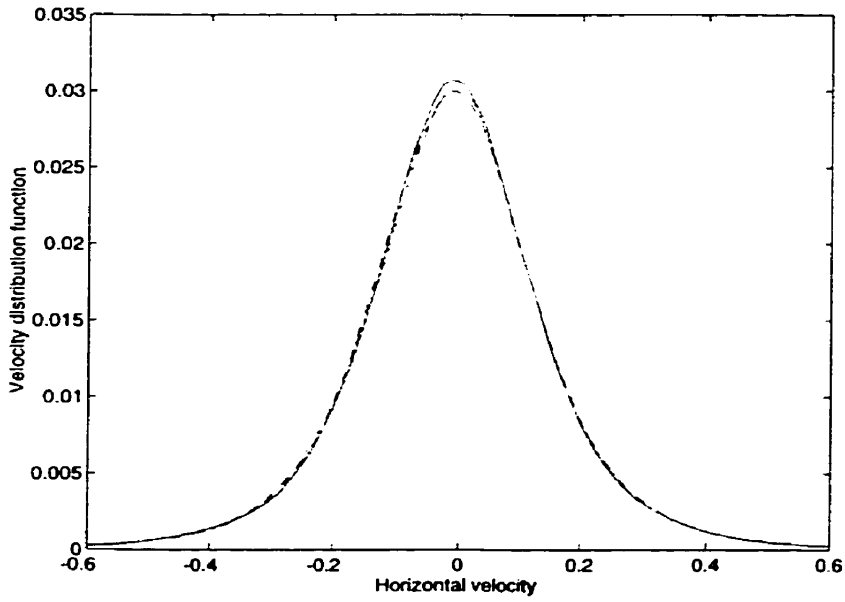

Figure 3.3.3. Velocity distribution of horizontal component of velocity in fluidization without fixed particles at St=15 Solid line is for u^{∞}=0.3, dash-dotted line for u^{∞}=0.5, and dashed line for u^{∞}=0.6.

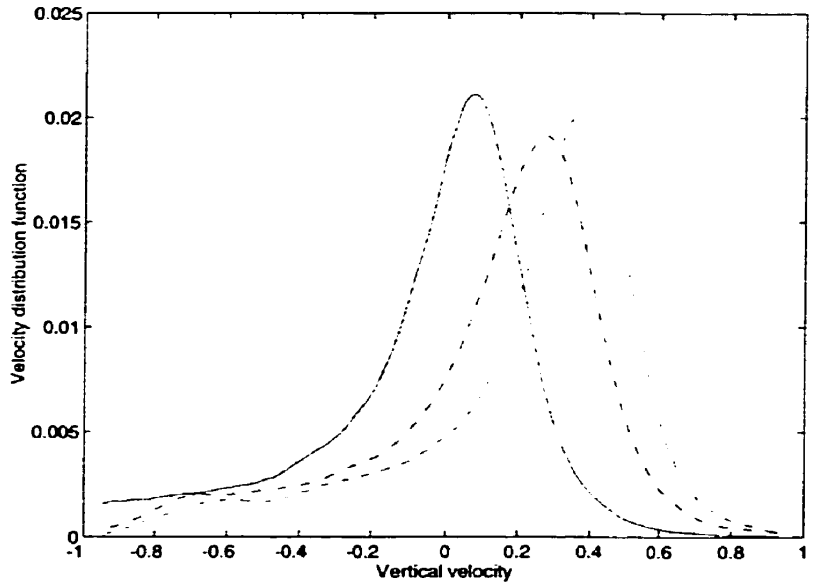

Figure 3.3.4. Velocity distribution of vertical component of velocity in fluidization without fixed particles at St=15 Solid line is for u^{∞}=0.3, dash-dotted line for u^{∞}=0.5, and dashed line for u^{∞}=0.6.

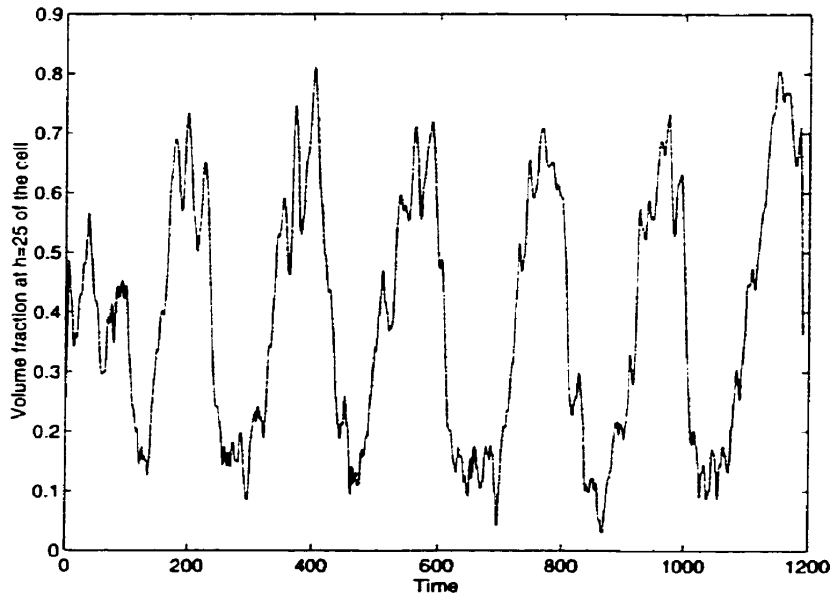

Figure 3.3.5. Volume fraction of particles in fluidization without fixed particles at h=25 level of the cell, St=15, and u^{∞}=0.3 .

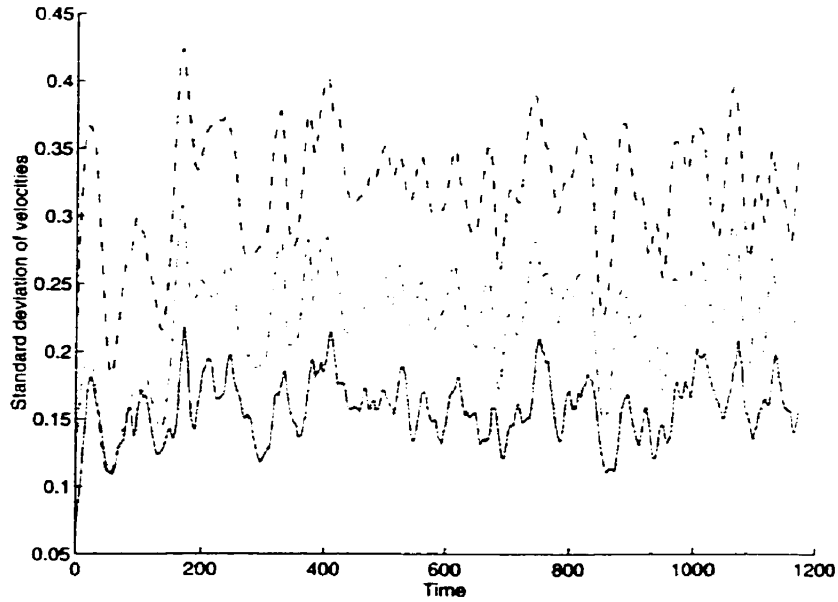

Figure 3.3.6. Standard deviation of velocities of particles in fluidization without fixed particles at St=15 and u^{∞}=0.3. Solid line is for horizontal component of velocity, dash-dotted line for vertical component of velocity, and dashed line for magnitude of velocity.

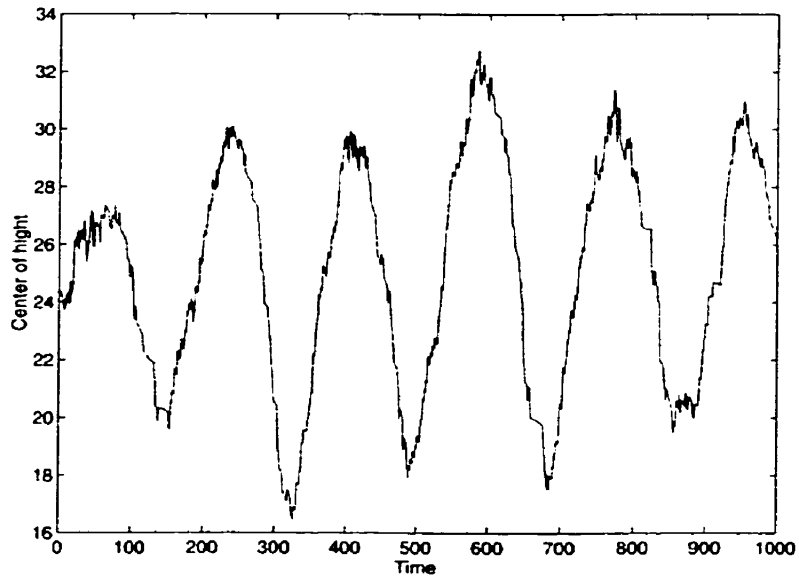

Figure 3.3.7. Height of center of mass of particles in fluidization without fixed particles at St=15 and u^{∞}=0.3.

3.4 Spouted bed

Fig. 3.4.1 shows the sequence of simulation of a spouted bed at $u^{\sim}$=1 and St=10. Cell has the dimension of $17.5\times50\times2$ and $u^{\sim}$ is zero except at the center of cell with a thickness of 3.5. Fig. 3.4.2-3 show that kinetic energy, and height of center of mass of particles are nearly constant in respect to time. Fig. 3.4.4-5 show how the average kinetic energy per particles, and height of center of mass increases with response to increase in $u^{\sim}$. Fig. 3.4.6-7 show that when stokes number increases, the height of center of mass also increases but the kinetic energy per particle decreases.

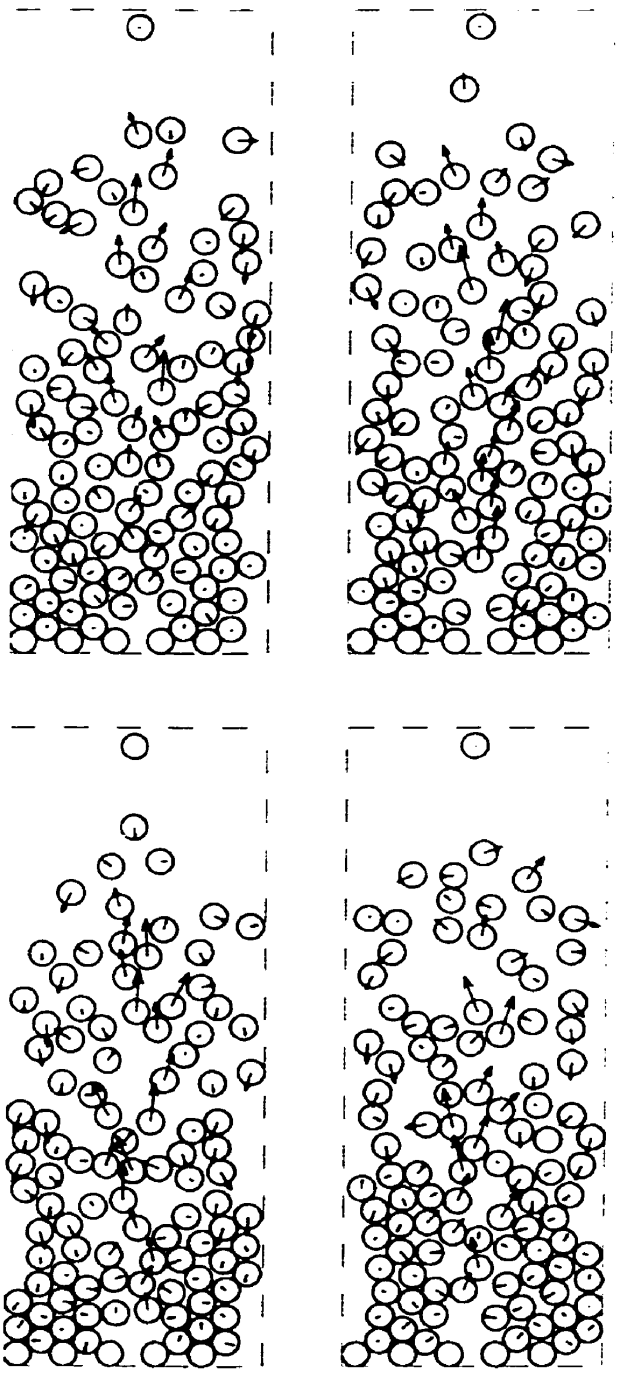

Figure 3.4.1. Sequence of the simulation of spouted bed at St=10 and u^{*}=1 superficial gas velocity. Related times of the frames from lower left to upper right are 310, 320, 330, and 340 in dimensionless units respectively.

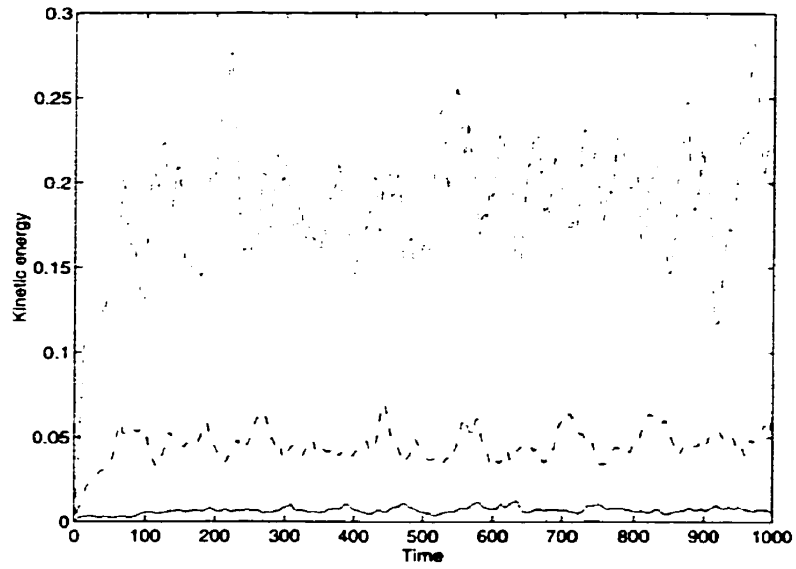

Figure 3.4.2 Kinetic energy per particle in spouted bed at St=10. Solid line is for u^{∞}=0.3, dash-dotted line for u^{∞}=0.6, dashed line for u^{∞}=1.3

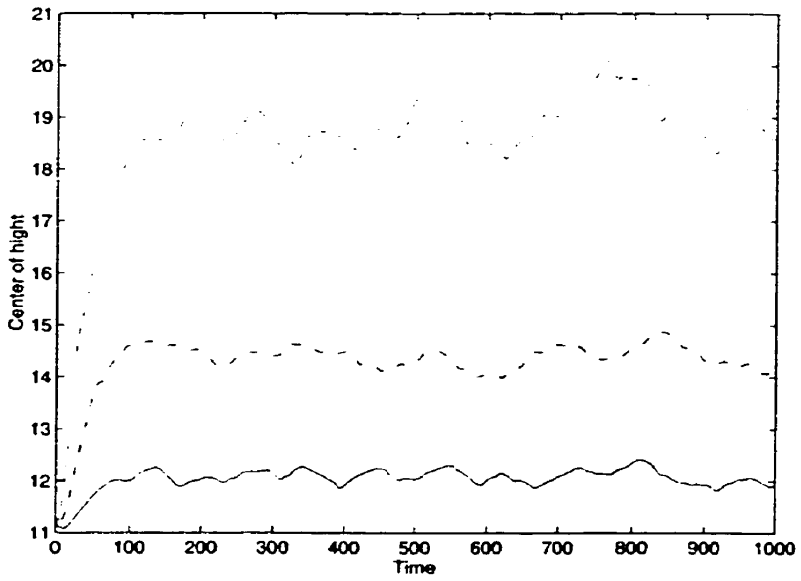

Figure 3.4.3 Height of center of mass of per particles in spouted bed at St=10. Solid line is for u^{∞}=0.3, dash-dotted line for u^{∞}=0.6, dashed line for u^{∞}=1.3

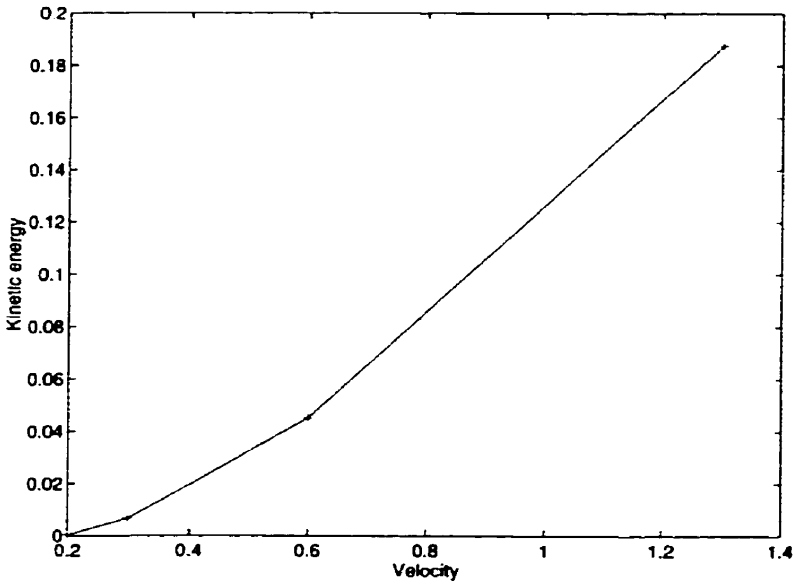

Figure 3.4.4 Kinetic energy per particle in spouted bed at St=10 as a function of superficial gas velocity.

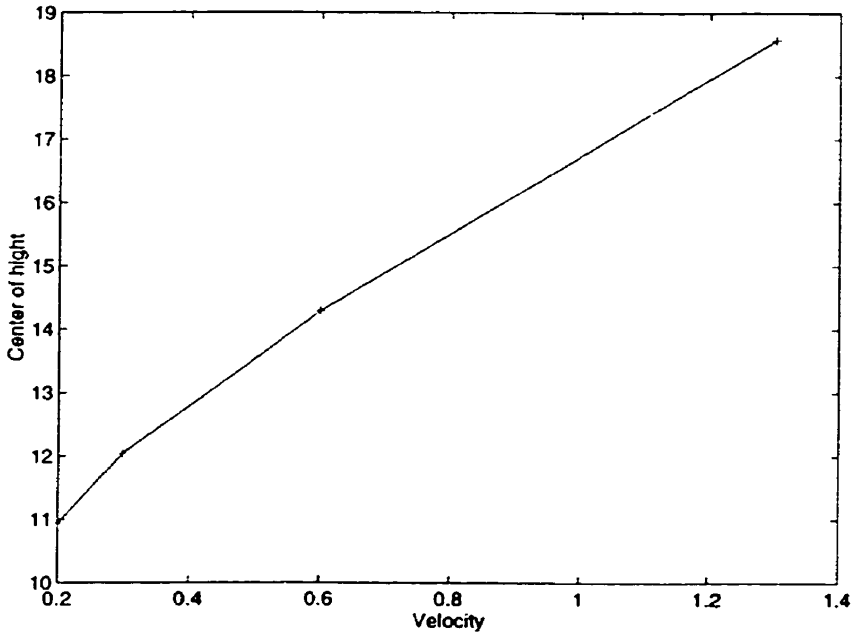

Figure 3.4.5 Height of center of mass of particles in spouted bed at St=10 as a function of superficial gas velocity.

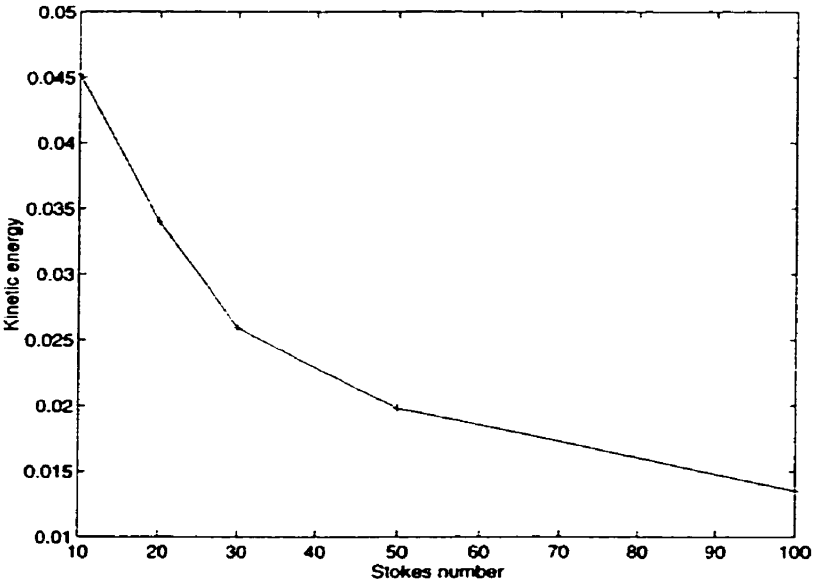

Figure 3.4.6 Kinetic energy per particle in spouted bed at u^{∞}=0.6.

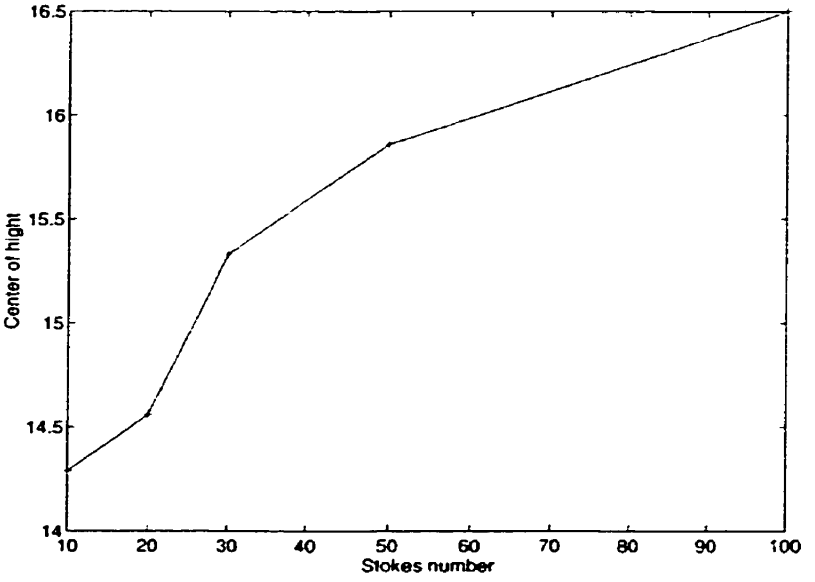

Figure 3.4.7 Height of center of mass of particles in spouted bed at u^{∞}=0.6.

3.5 Fluidization with mixed cohesive and non-cohesive particles

Fig. 3.5.1 shows the sequence of simulation of fluidization. Gray particles are highly cohesive. The m, n, S_{F0}, and $F_{\max}$ of the Lennard-Jones parameters for these particles are equal to 1, 0.5, 0.05, and 20 respectively. Gray particles quickly agglomerate and fluidization is suppressed. It is seen if Fig. 3.5.2 that standard deviations of particles decreases as particles agglomerate. Fig. 3.5.3 shows that as cohesive particles agglomerate, fluidization becomes weak and volume fraction increases to that of a fixed bed. Fig. 3.5.4-6 show the velocity distribution of particles at two specific times; one at early time when cohesive particles are apart from each other and the other one when they are agglomerated. It shows that after agglomeration, most of particles have velocity around zero. Fig. 3.5.7-8 show that by agglomeration, kinetic energy per particle and height of center of mass of particles decreases.

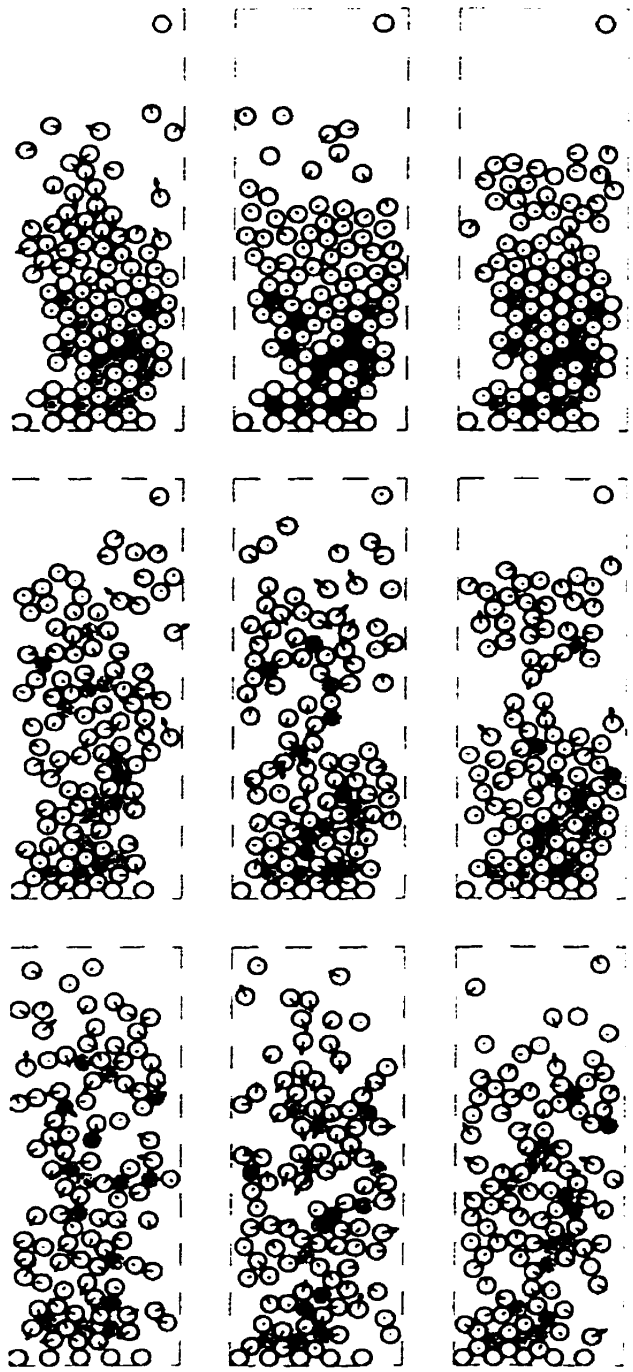

Figure 3.5.1. Sequence of the simulation of fluidization with mixed particles of cohesive and non-cohesive particles at St=10 and u^{*}=0.25 superficial gas velocity. The gray particles are highly cohesive. Related times of the frames from lower left to upper right are 20, 40, 60, 80, 100, 200, 500, 700, and 999 in dimensionless units respectively.

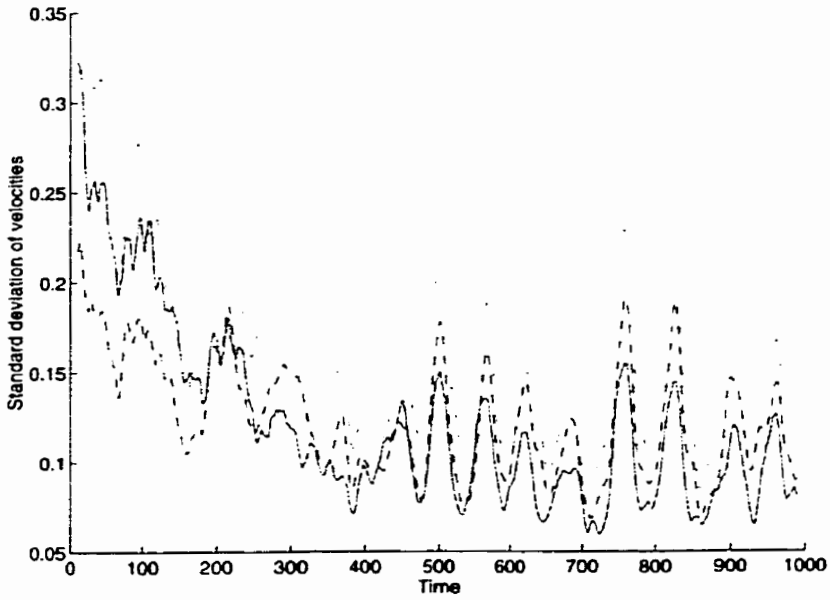

Figure 3.5.2. Standard deviation of velocities of particles in fluidization with mixed cohesive-noncohesive particles at St=10 and u^{∞}=0.25. Solid line is for horizontal component of velocity, dash-dotted line for vertical component of velocity, and dashed line for magnitude of velocity.

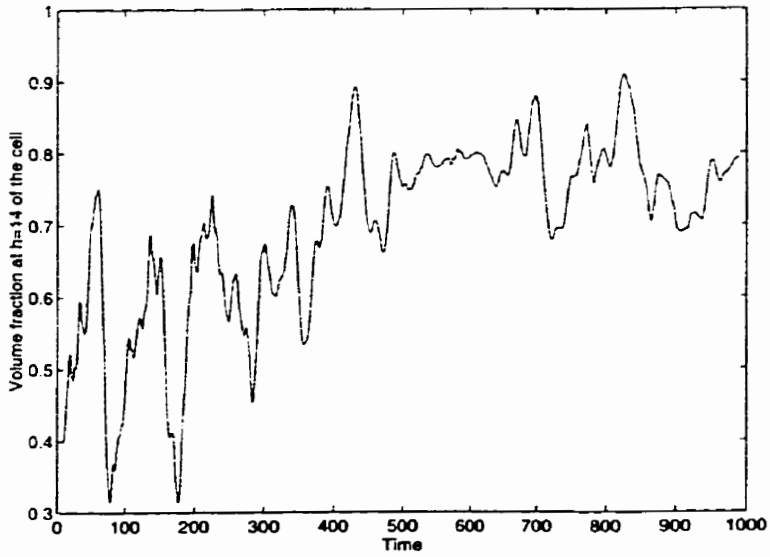

Figure 3.5.3. Volume fraction of particles in fluidization with mixed cohesive-noncohesive particles at h=14 level of cell at St=10 and u^{∞}=0.25

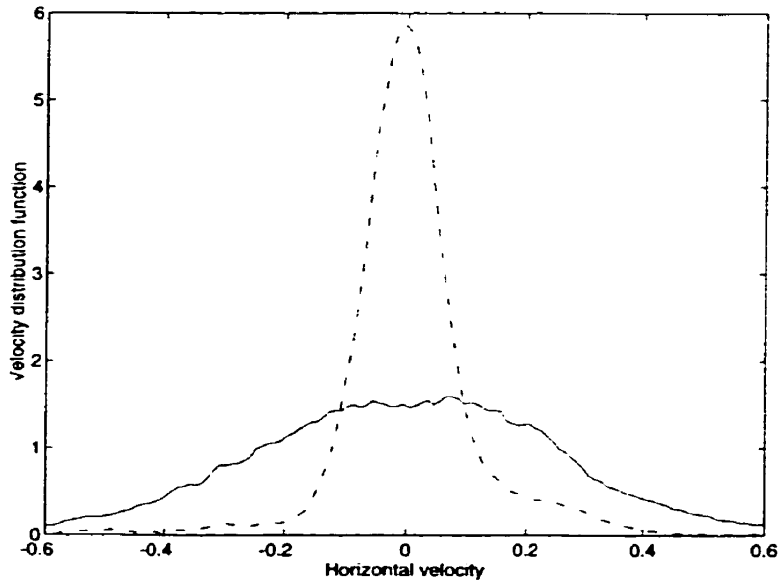

Figure 3.5.4. Velocity distribution of horizontal components of velocities of particles in fluidization with mixed cohesive-noncohesive particles at St=10 and u^{∞}=0.25. Solid line is at time=40, and dash-dotted line is at time=980.

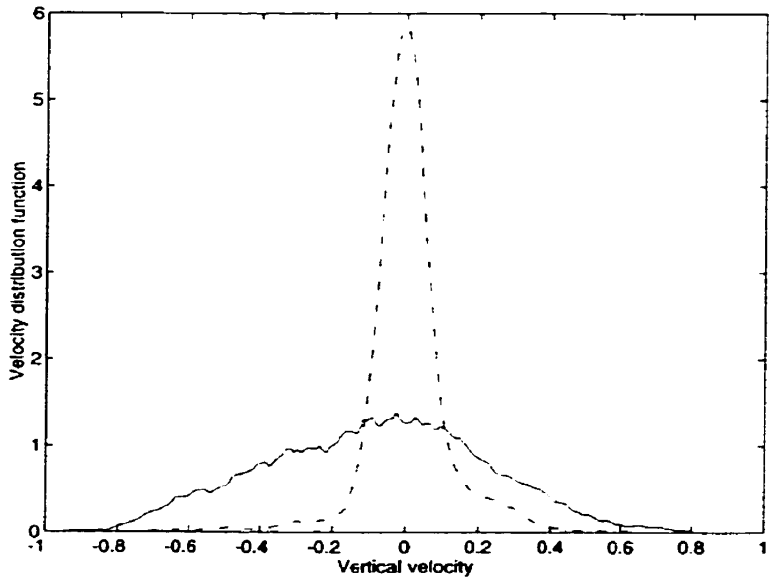

Figure 3.5.5. Velocity distribution of vertical components of velocities of particles in fluidization with mixed cohesive-noncohesive particles at St=10 and u^{∞}=0.25. Solid line is at time=40, and dash-dotted line is at time=980.

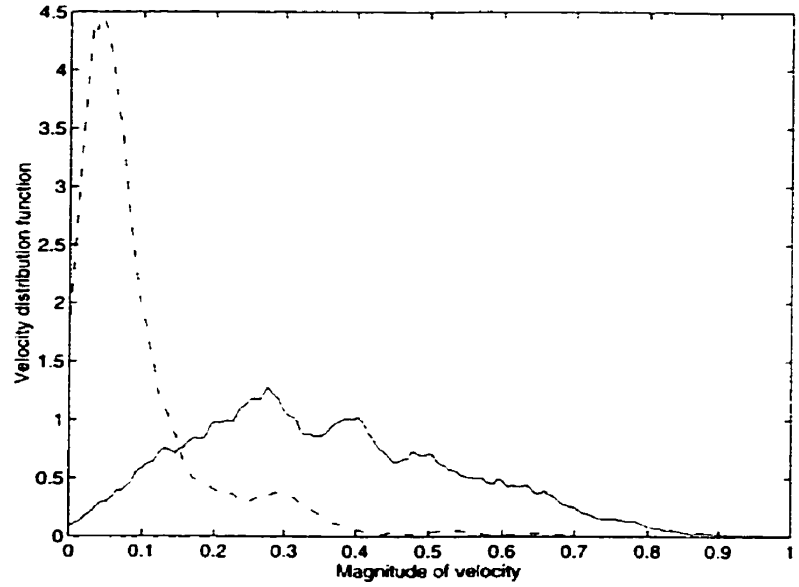

Figure 3.5.6. **Distribution of magnitude of velocities of particles in fluidization with mixed cohesive-noncohesive particles at St=10 and u^{∞}=0.25. Solid line is at time=40, and dash-dotted line is at time=980.**

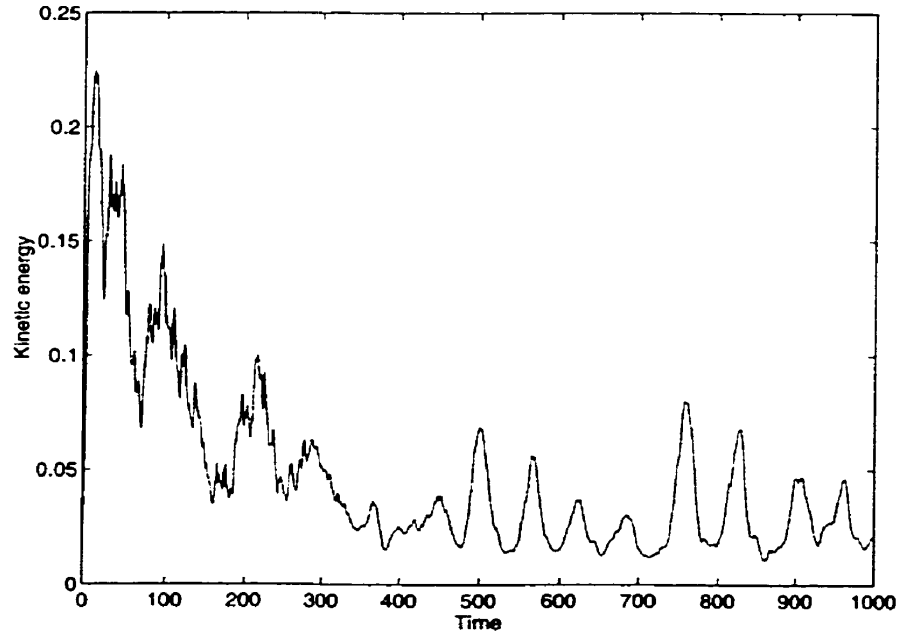

Figure 3.5.7. **Kinetic energy per particle in fluidization with mixed cohesive-noncohesive particles at St=10, and u^{∞}=0.25.**

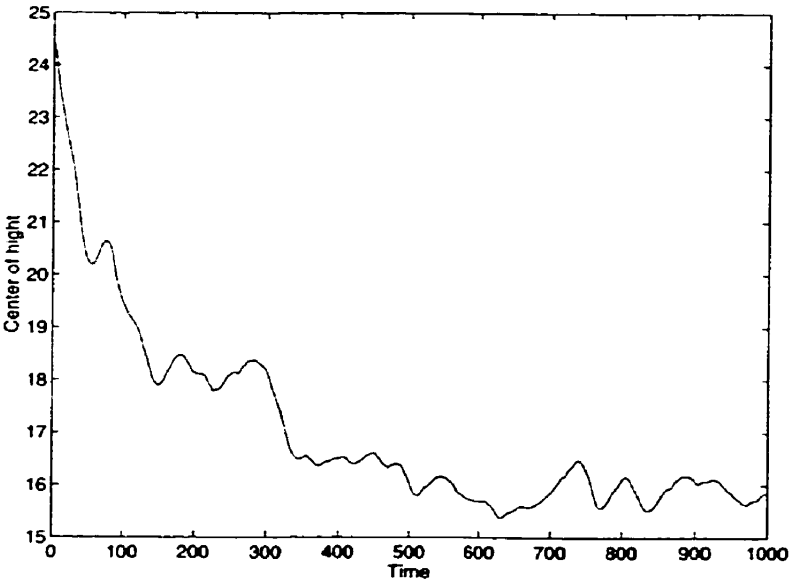

Figure 3.5.8. Height of center of mass of particles in fluidization with mixed cohesive-noncohesive particles at St=10, and u^{∞}=0.25.

CHAPTER 4: CONCLUSIONS AND RECOMMENDATIONS FOR FUTURE WORK

In this work a theoretical model, based on Newton's laws of motion, a model of particle-particle interactions, and stokes equation of motion for calculation of hydrodynamic forces, has been used to simulate the behavior of suspensions in various configurations of sedimentation, fluidization, and spouted bed. Results of the simulations are favorably similar to results obtained from experimental observations. The scale of the simulation, that is much smaller than the one arising in industrial applications, can be increased by using powerful modern computers. The following recommendations are suggested for future continuation of this work:

1) Simulating non-spherical particles with different sizes.
2) Lennard-Jones force is similar to metallic bond and particles can freely slideone over another particle. It is recommended to include forces that prevent bonded particles from changing orientation
3) Simulating large particles by using Navier-Stokes equation of motion.
4) Including chemical reactions between gas-particle phases and /or particle-particle.
5) Simulating several cells in parallel without using periodic boundary condition method.
6) Simulating 3-D suspensions

REFERENCES

ATKINS, P.W. (1990). Physical chemistry, fourth edition. *Oxford University Press*

BEENAKKER C.W.J. (1986). Ewald sum of the Rotne-Prager tensor. *Journal of chemical physics*, 85(3), 1 August 1986

BRADY, J. F. et BOSSIS, G. (1988). Stokesian dynamics. *Annual review of fluid mechanics*, 20:111-57

DEIVA VENKATESH, R. et GRMELA, M. et CHAOUKI, J. (1998). Simulation of vibrated fine powders. *Powder Technology*, 100 211-222

DING, J. et GIDASPOW, D. (1990). A bubbling fluidization model using kinetic theory of granular flow. *AIChE Journal*, Vol. 36, No. 4

DURLOFSKY, L. et BRADY, J.F. et BOSSIS, G. (1987). Dynamic simulation of hydrodynamically interacting particles. *Journal of fluid mechanics*, Vol.180, pp. 21-49

GELDART, D. (1986). Gas Fluidization Technology. *John Wiley & Sons*

HAPPEL, J. et BRENNER, H. (1986). Low Reynolds number hydrodynamics with special applications to particulate media, *Martinus Nijhoff Publishers*

HOOMANS, B.P.B. et KUIPERS, J.A.M. et BRIELS, W.J. et Van SWAAIJ, P.M. (1996) Discrete article simulation of bubble and slug formation in a two-dimensional gas-fluidized bed: a hard-sphere approach. *Chemical Engineering Science*, Vol. 51, No. 1 pp. 99-118

ICHIKI, K. et HAYAKAWA H. (1995). Dynamical simulation of fluidized bed: Hydrodynamically interacting granular particles. *Physical Review E* Vol. 52, Number 1, 658

ICHIKI, K. et HAYAKAWA H. (1998). Analysis of statistical quantities in simulation of fluidized beds. *Physical Review E* Vol. 57, Number 2 1990

JEFFREY, D.J. et ONISHI, Y. (1984). Calculation of resistance and mobility functions for two unequal rigid spheres in low-Reynolds-number flow. *Journal of fluid mechanics*, Vol. 139, pp. 261-290

KUIPERS, J.A.M. et VAN DUIN, K.J. et VAN BECKUM, F.P.H. et VAN SWAAIJ, W.P.M. (1993). Computer simulation of the hydrodynamics of a two-dimensional gas-fluidized bed. *Computers Chemical Engineering*, Vol. 17, No. 8, pp. 839-858

LADYZHENSKAYA, O.A. (1963). The mathematical theory of viscous incompressible flow. *Gordon & Breach*

PELL, M. (1990). Handbook of Powder Technology, Volume 8, Gas Fluidization. *Elsevier Science Publishers B.V.*

PERRY, R. H. et GREEN, D. Perry's chemical engineers' handbook, seventh edition *McGraw Hill Book Company*

PRESS, W.H. et FLANNERY, B.P. et TEUKOLSKY, S.A. et VETTERLING, W.T. (1988). Numerical Recipes *Cambridge University Press, Cambridge*

SANGTAE, K. et SEPPO, J. KARRILA (1991). Microhydrodynamics, Principles and Selected Applications. *Butterworth-Heinemann*

YOUNG, H.D. (1992) University Physics, Eighth edition, *Addison-Wesley Publishing Company*

APPENDIX 1: HYDRODYNAMIC FORCES

1. Far-field many-body interactions

" Beenakker (1986) " has developed the expressions for M^{∞} and the results are as follows:

$$M_{i,j}^{\alpha,\alpha} = 1 - \frac{1}{\sqrt{\pi}}\left(6a\xi - \frac{40}{3}a^3\xi^3\right) + \sum_{\gamma\neq 0} M_{i,j}^{(1)}(\mathbf{r}_\gamma) + \frac{1}{V}\sum_{\lambda\neq 0} M_{i,j}^{(2)}(\mathbf{k}_\lambda) \tag{26a}$$

for diagonal elements of M^{∞} in which $i = j$ and $\alpha = \beta$.

$$M_{i,j}^{\alpha,\alpha} = \sum_{\gamma\neq 0} M_{i,j}^{(1)}(\mathbf{r}_\gamma) + \frac{1}{V}\sum_{\lambda\neq 0} M_{i,j}^{(2)}(\mathbf{k}_\lambda) \tag{26b}$$

when $i \neq j$ and $\alpha = \beta$

$$M_{i,j}^{\alpha,\beta} = \sum_{\gamma} M_{i,j}^{(1)}\left(\mathbf{X}^\alpha - \mathbf{X}^\beta + \mathbf{r}_\gamma\right) + \frac{1}{V}\sum_{\lambda\neq 0}\cos\left[\mathbf{k}_\lambda\left(\mathbf{X}^\alpha - \mathbf{X}^\beta\right)\right] M_{i,j}^{(2)}(\mathbf{k}_\lambda) \tag{26c}$$

where γ and λ are the index vectors of periodic cells in three dimensions.

$$\gamma = (n_1, n_2, n_3) \tag{27a}$$

$$\lambda = (m_1, m_2, m_3) \tag{27b}$$

γ and λ are independent of each other and $\gamma = (0,0,0)$, $\lambda = (0,0,0)$ at main periodic cell. This means the two lattice sum pairs in the above relations can run over different periodic cell configurations to converge to their final values. V is the dimension less

volume of a periodic cell, $V = L_1 L_2 L_3$ where L_1, L_2 and L_3 are the length, width and height of a cell respectively.

$$\mathbf{r}_\gamma = (n_1 L_1 \quad n_2 L_2 \quad n_3 L_3) \tag{28a}$$

$$\mathbf{k}_\lambda = \left(\frac{2\pi n_1}{L_1} \quad \frac{2\pi n_2}{L_2} \quad \frac{2\pi n_3}{L_3} \right) \tag{28b}$$

$\mathbf{r}_\gamma$ is the position vector of a periodic cell and equals to zero at main periodic cell. $\mathbf{k}_\lambda$ is called reciprocal lattice vector and equals to zero at main periodic cell.

$$M_{i,j}^{(1)}(\mathbf{r}) = \operatorname{erfc}(\xi r)\left[\delta_{i,j}\left(\frac{3a}{4r} + \frac{a^3}{2r^3}\right) + \hat{r}_i \hat{r}_j \left(\frac{3a}{4r} - \frac{3a^3}{2r^3}\right)\right] + \frac{e^{-\xi^2 r^2}}{\sqrt{\pi}}\left[\begin{array}{l} \delta_{i,j}\left(4a^3\xi^7 r^4 + 3a\xi^3 r^2 - 20a^3\xi^5 r^2 - \frac{9}{2}a\xi + 14a^3\xi^3 + \frac{a^3\xi}{r^2}\right) + \\ \hat{r}_i \hat{r}_j \left(-4a^3\xi^7 r^4 - 3a\xi^3 r^2 + 16a^3\xi^5 r^2 + \frac{3}{2}a\xi - 2a^3\xi^3 - \frac{3a^3\xi}{r^2}\right) \end{array}\right] \tag{29}$$

$$M_{i,j}^{(2)}(\mathbf{k}_\lambda) = 6\pi a(\delta_{i,j} - \hat{k}_i \hat{k}_j)\frac{1}{k_\lambda^2}\left(1 - \frac{a^2 k_\lambda^2}{3}\right)\left(1 + \frac{k_\lambda^2}{4\xi^2} + \frac{k_\lambda^4}{8\xi^4}\right) e^{\frac{-k_\lambda^2}{4\xi^2}} \tag{30}$$

$$\operatorname{erfc}(x) = \frac{2}{\sqrt{\pi}} \int_x^\infty \exp(-z^2)\,dz \tag{31}$$

$\xi = \frac{\sqrt{\pi}}{\bar{L}}$, where $\bar{L} = (L_1 L_2 L_3)^{1/3}$ is the average length of a periodic cell.

$\mathbf{r} = \mathbf{X}^\alpha - \mathbf{X}^\beta + \mathbf{r}_\gamma$ is a vector connecting the centers of two particles. $\hat{k}_i$ and $\hat{r}_i$ are the components of unit vectors in direction of $\mathbf{k}_\lambda$ and $\mathbf{r}$ respectively.

2. Two-body interactions

" Jeffrey and Onishi (1984) " have developed relations for two-body interactions. It is valid for both near and far field interactions. The elements of two-body resistance matrix are calculated from:

$$R_{i,j}^{\alpha\beta} = X_{\alpha\beta}^{A}\hat{r}_i\hat{r}_j + Y_{\alpha\beta}^{A}\left(\delta_{i,j} - \hat{r}_i\hat{r}_j\right) \tag{32}$$

where

$$X_{\alpha\beta}^{A}(s,\lambda) = X_{\beta\alpha}^{A}(s,\lambda) = X_{(3-\alpha)(3-\beta)}^{A}(s,\lambda^{-1}) \tag{33}$$

$$X_{11}^{A} = g_1\left(1-\frac{4}{S^2}\right)^{-1} - g_2\ln\left(1-\frac{4}{S^2}\right) - g_3\left(1-\frac{4}{S^2}\right)\ln\left(1-\frac{4}{S^2}\right) + f_0(\lambda) - g_1 +$$

$$\sum_{\substack{m=2\\ m\ \text{even}}}^{\infty}\left(\frac{1}{2^m(1+\lambda)^m}f_m(\lambda) - g_1 - \frac{2}{m}g_2 + \frac{4}{mm_1}g_3\right)\left(\frac{2}{S}\right)^m \tag{34}$$

$$-\frac{1}{2}(1+\lambda)X_{12}^{A} = \frac{2}{S\left(1-\frac{4}{S^2}\right)}g_1 + \ln\left(\frac{S+2}{S-2}\right)g_2 + \left(1-\frac{4}{S^2}\right)\ln\left(\frac{S+2}{S-2}\right)g_3 + \frac{4}{S}g_3 +$$

$$\sum_{\substack{m=1\\ m\ \text{odd}}}^{\infty}\left(\frac{2}{m(1+\lambda)^m}f_m(\lambda) - g_1 - \frac{2}{m}g_2 + \frac{4}{mm_1}g_3\right)\left(\frac{2}{S}\right)^m \tag{35}$$

where

$f_0 = 1$
$f_1 = 3\lambda$
$f_2 = 9\lambda$
$f_3 = -4\lambda + 27\lambda^2 - 4\lambda^3$
$f_4 = -24\lambda + 81\lambda^2 + 36\lambda^3$
$f_5 = 72\lambda^2 + 243\lambda^3 + 72\lambda^4$

$$f_6 = 16\lambda + 108\lambda^2 + 281\lambda^3 + 648\lambda^4 + 144\lambda^5$$
$$f_7 = 288\lambda^2 + 1620\lambda^3 + 1515\lambda^4 + 1620\lambda^5 + 288\lambda^6$$

$$f_8 = 576\lambda^2 + 4848\lambda^3 + 5409\lambda^4 + 4524\lambda^5 + 3888\lambda^6 + 576\lambda^7$$
$$f_9 = 1152\lambda^2 + 9072\lambda^3 + 14752\lambda^4 + 26163\lambda^5 + 14752\lambda^6 + 9072\lambda^7 + 1152\lambda^8$$

$$f_{10} = 2304\lambda^2 + 20736\lambda^3 + 42804\lambda^4 + 115849\lambda^5 + 76176\lambda^6 + 39264\lambda^7 + 20736\lambda^8 + 2304\lambda^9$$

$$f_{11} = 4608\lambda^2 + 46656\lambda^3 + 108912\lambda^4 + 269100\lambda^5 + 319899\lambda^6 + 269100\lambda^7 + 108912\lambda^8 + 46656\lambda^9 + 4608\lambda^{10}$$

(36)

$$g_1 = \frac{2\lambda^2}{(1+\lambda)^3}, \qquad g_2 = \frac{\lambda(1+7\lambda+\lambda^2)}{5(1+\lambda)^3} \tag{37a,b}$$

$$g_3 = \frac{(1+18\lambda-29\lambda^2+18\lambda^3+\lambda^4)}{42(1+\lambda)^3} \tag{37c}$$

$$\lambda = \frac{a_\beta}{a_\alpha}, \qquad S = \frac{2r}{a_\alpha + a_\beta}, \qquad \delta_{i,j} = \begin{cases} 1 & \text{for } i = j \\ 0 & \text{for } i \neq j \end{cases}$$

In our case $a_\alpha = a_\beta = 1$

$$m_1 = -2\delta_{m,2} + (m-2)(1-\delta_{m,2}) \tag{38}$$

$$Y^A_{\alpha\beta}(S,\lambda) = Y^A_{\beta\alpha}(S,\lambda) = Y^A_{(3-\alpha)(3-\beta)}(S,\lambda^{-1}) \tag{39}$$

$$Y^A_{11} = -\ln\left(1-\frac{4}{S^2}\right)g_2 - \left(1-\frac{4}{S^2}\right)\ln\left(1-\frac{4}{S^2}\right)g_3 + f_0(\lambda) + \sum_{\substack{m=2 \\ m \text{ even}}}^{\infty}\left(\frac{1}{2^m(1+\lambda)^m}f_m(\lambda) - \frac{2}{m}g_2 + \frac{4}{mm_1}g_3\right)\left(\frac{2}{S}\right)^m \tag{40}$$

$$-\frac{1}{2}(1+\lambda)Y_{12}^{A} = \ln\left(\frac{S+2}{S-2}\right)g_2 + \left(1-\frac{4}{S^2}\right)\ln\left(\frac{S+2}{S-2}\right)g_3 + \frac{4}{S}g_3 + \sum_{\substack{m=1 \\ m \text{ odd}}}^{\infty}\left(\frac{1}{2^m(1+\lambda)^m}f_m(\lambda) - \frac{2}{m}g_2 + \frac{4}{mm_1}g_3\right)\left(\frac{2}{S}\right)^m \tag{41}$$

where

$$f_0 = 1$$

$$f_1 = \frac{3}{2}\lambda$$

$$f_2 = \frac{9}{4}\lambda$$

$$f_3 = 2\lambda + \frac{27}{8}\lambda^2 + 2\lambda^3$$

$$f_4 = 6\lambda + \frac{81}{16}\lambda^2 + 18\lambda^3$$

$$f_5 = \frac{63}{2}\lambda^2 + \frac{243}{32}\lambda^3 + \frac{63}{2}\lambda^4$$

$$f_6 = 4\lambda + 54\lambda^2 + \frac{1241}{64}\lambda^3 + 81\lambda^4 + 72\lambda^5$$

$$f_7 = 144\lambda^2 + \frac{1053}{8}\lambda^3 + \frac{19083}{128}\lambda^4 + \frac{1053}{8}\lambda^5 + 144\lambda^6$$

$$f_8 = 279 + \frac{4261}{8}\lambda^3 + \frac{126369}{256}\lambda^4 - \frac{117}{8}\lambda^5 + 648\lambda^6 + 288\lambda^7$$

$$f_9 = 576\lambda^2 + 1134\lambda^3 + \frac{60443}{32}\lambda^4 + \frac{766179}{512}\lambda^5 + \frac{60443}{32}\lambda^6 + 1134\lambda^7 + 576\lambda^8$$

$$f_{10} = 1152\lambda^2 + \frac{7857}{4}\lambda^3 + \frac{98487}{16}\lambda^4 + \frac{10548393}{1024}\lambda^5 + \frac{67617}{8}\lambda^6 - \frac{351}{2}\lambda^7 + 3888\lambda^8 + 1152\lambda^9$$

$$f_{11} = 2304\lambda^2 + 7128\lambda^3 + \frac{22071}{2}\lambda^4 + \frac{2744505}{128}\lambda^5 + \frac{95203835}{2048}\lambda^6 + \frac{2744505}{128}\lambda^7 + \frac{22071}{2}\lambda^8 + 7128\lambda^9 + 2304\lambda^{10} \tag{42}$$

$$g_2(\lambda) = \frac{4\lambda(2+\lambda+2\lambda^2)}{15(1+\lambda)^3} \tag{43}$$

$$g_3(\lambda) = \frac{2(16-45\lambda+58\lambda^2-45\lambda^3+16\lambda^4)}{(1+\lambda)^3} \tag{44}$$

$$m_1 = -2\delta_{m,2} + (m-2)(1-\delta_{m,2}) \tag{38}$$

3. Far-field two-body interactions

The relations developed by " Durlofsky and Brady (1987) " are used for calculation of far-field two-body interactions. First the mobility functions for each pair that was used in calculation of R_{2B} are calculated:

$$x^a_{\alpha\alpha} = x^a_{\beta\beta} = 1. \qquad x^a_{\alpha\beta} = x^a_{\beta\alpha} = \frac{3}{2r} - \frac{1}{r^3} \tag{45a,b}$$

$$y^a_{\alpha\alpha} = y^a_{\beta\beta} = 1. \qquad y^a_{\alpha\beta} = y^a_{\beta\alpha} = \frac{3}{4r} + \frac{1}{2r^3} \tag{46a,b}$$

we know that:

$$\begin{pmatrix} R^{\alpha\alpha} & R^{\alpha\beta} \\ R^{\beta\alpha} & R^{\beta\beta} \end{pmatrix} \begin{pmatrix} M^{\alpha\alpha} & M^{\alpha\beta} \\ M^{\beta\alpha} & M^{\beta\beta} \end{pmatrix} = \begin{pmatrix} 1 & 0 \\ 0 & 1 \end{pmatrix} \tag{47}$$

After substituting the mobility and resistance tensors in terms of their mobility and resistance functions, we would reach at the following relations between resistance and mobility functions:

$$\begin{pmatrix} X^A_{\alpha\alpha} & X^A_{\alpha\beta} \\ X^A_{\beta\alpha} & X^A_{\beta\beta} \end{pmatrix} = \begin{pmatrix} x^a_{\alpha\alpha} & x^a_{\alpha\beta} \\ x^a_{\beta\alpha} & x^a_{\beta\beta} \end{pmatrix}^{-1} = \frac{1}{(x^a_{\alpha\alpha})^2 - (x^a_{\alpha\beta})^2} \begin{pmatrix} x^a_{\alpha\alpha} & -x^a_{\alpha\beta} \\ -x^a_{\alpha\beta} & x^a_{\alpha\alpha} \end{pmatrix} \tag{48}$$

$$\begin{pmatrix} Y^A_{\alpha\alpha} & Y^A_{\alpha\beta} \\ Y^A_{\beta\alpha} & Y^A_{\beta\beta} \end{pmatrix} = \begin{pmatrix} y^a_{\alpha\alpha} & y^a_{\alpha\beta} \\ y^a_{\beta\alpha} & y^a_{\beta\beta} \end{pmatrix}^{-1} = \frac{1}{(y^a_{\alpha\alpha})^2 - (y^a_{\alpha\beta})^2} \begin{pmatrix} y^a_{\alpha\alpha} & -y^a_{\alpha\beta} \\ -y^a_{\alpha\beta} & y^a_{\alpha\alpha} \end{pmatrix} \tag{49}$$

Having known the mobility functions and using the above relations, we calculate the resistance functions of $X^A_{\alpha\alpha}$, $X^A_{\alpha\beta}$, $Y^A_{\alpha\alpha}$, and $Y^A_{\alpha\beta}$ and then calculate the far-field two-body resistance tensors of $R^{\alpha\alpha,\infty}_{2B}$, $R^{\alpha\beta,\infty}_{2B}$, $R^{\beta\alpha,\infty}_{2B}$, and $R^{\beta\beta,\infty}_{2B}$ from the following equation:

$$R^{\alpha\beta,\infty}_{i,j} = X^A_{\alpha\beta}\hat{r}_i\hat{r}_j + Y^A_{\alpha\beta}\left(\delta_{i,j} - \hat{r}_i\hat{r}_j\right) \tag{50}$$

Finally these tensors are added to the corresponding tensors of R^{∞}_{2B} resistance matrix.

APPENDIX 2: ARTICLE

SIMULATIONS AND EXPERIMENTS ON FINE POWDER FLUIDIZATION

R. Deiva Venkatesh[1,2], J. Chaouki[1,2] *,M. Grmela[2] and R. Mortazavi[1,2]

[1]BIOPRO Centre, [2]Chemical Engineering Department, Ecole Polytechnique de Montreal, P.O. Box 6079, Montreal, Qué. H3C 3A7, Canada

---

Abstract

The Stokesian Dynamics method is used to simulate the air fluidization of an FCC powder bed. Besides detailed information on the instantaneous motion of the particles in the bed, the characteristics of the bubbling bed were estimated. The particle velocities observed in the simulations are compared to tracer velocities in a radioactive particle tracking experiment conducted at an air velocity of 0.44 m/s in an FCC bed having a diameter of 15 cm. Under equiscale assumptions, the particle velocities in experiment

and simulation were in good agreement. Two other simulations on FCC particles at air velocities of 0.09 m/s and 0.06 m/s were compared for bubble characteristics measured with the fiber-optic technique in the experimental fluidized bed. The size and rise velocity of bubbles obtained using the Stokesian Dynamics simulation were in good agreement with predictions by bubbling bed models at the vicinity of the distributor while model predictions differed slightly from experimental measurement at a height of 50 mm from the distributor. The average bed porosity extracted from simulations are close to the experimental measurements.

Within the current assumptions on the quantitative comparison of experimental and simulated fluidization of powders, we conclude that the Stokesian Dynamics method captures the essential behaviour of fluidized beds. The non-definite structure of a fluidized bed has also been differentiated from that of a fixed bed.

Keywords: Powders, fluidized beds, stokesian dynamics, fibre-optic analysis, radioactive particle tracking

---

• Corresponding author

1. Introduction

Powders have widespread applications in the industry ranging from chemical, pharmaceutical, agricultural and food industries. Some of these applications involve the fluidization of fine powders. Powders have been broadly classified as Group C, A, B and D under Geldart's classification of powders [1]. Numerous experimental and theoretical studies can be found in the literature on the gas fluidization of these powders with journals such as Powder Technology dedicated to such studies.

Several interesting phenomena such as channeling and agglomeration are observed in the case of Group C powders. Homogeneous fluidization with bed expansion in Group A powders, bubbling in Group A and B powders and slugging in Group B and D powders are well known with a battery of successful models to predict such phenomena.

These well-established models of fluidized beds serve the purpose of explaining the macroscopic quantities of the bed such as bubble size, bed expansion, bubble velocity and bed porosity but their focus is not on the bed microscopy explaining particle configurations and motion. With the ever-increasing power of computers, progress has been made on both the experimental and modeling routes of studying fluidized beds. Workstations are widely used to process data from radioactive particle tracking, laser velocimetry, optic fiber equipments etc., to study the microscopy of fluidized beds. On the other hand, modeling and simulations of fluidized beds can be performed on

computers for the same reasons. The two categories of fluidized bed models are: (a) the two-fluid model and (b) the discrete-particle model that describe fluidized beds with the latter category having the advantage of effectively describing the particle motion [2].

The focus of this paper is the discrete particle simulation of fluidized powders. To simulate the fluidization of powders, we employ the Stokesian dynamics method. The empirical parameters that have to be introduced in the technique are those needed to characterize the Stokesian particle-fluid interactions [2, 3]. Recent simulations using the Stokesian Dynamics method have reproduced realistic particle motion in gas fluidized granular systems [3, 4].

In these simulations, the Stokesian Dynamics method is used to simulate the air fluidization of a two-dimensional bed composed of 128 spherical glass particles with 10 particles forming the fixed bottom of the bed with an uniform air velocity at a value 30% of the single particle terminal velocity. The bed whose thickness was the same as the size of the particles had width as 35 and height as 50 (dimensionless units).

The purpose of this paper is to compare the bed characteristics such as bubble size, bubble velocity and particle velocities obtained from the Stokesian Dynamics simulation of gas fluidized Fluid Cracking Catalyst with experimental measurements of these quantities using radioactive particle tracking and fiber-optic methods as well as bubbling bed models.

2. Stokesian dynamics method with periodic boundary conditions

We recall the fluidized bed model of Ichiki and Hayakawa [4] (a model to simulate the fluidization of rigid particles). For more details concerning this model refer to the paper of Brady and Bossis [2] describing Stokesian Dynamics and the paper of Ichiki and Hayakawa [4] describing the simulation of fluidized beds using the Stokesian Dynamics method. Ichiki and Hayakawa assume that the bed is composed of monodisperse spheres with no rotational motion. Table 1 enlists the characteristics of the fluid and the powder.

The motion of N fluidized particles is given by Newton's equation [4]:

$$St\frac{d\mathbf{u}}{dt} = \exp\left(\frac{t}{St}\right)\mathbf{V} \qquad (1)$$

Here, t denotes the time, St is the Stokes number, **x** is the 2D position vector, **u**=U.exp(t/St)

$$\mathbf{U} = \begin{bmatrix} \mathbf{U}_1 \\ \mathbf{U}_2 \\ \cdot \\ \cdot \\ \cdot \\ \mathbf{U}_N \end{bmatrix}$$

where **U** is the 2D velocity vector for the N-particle system.

V, representing the terminal velocity of the particles is given by the following equation:

$$\mathbf{V} - \mathbf{u}^{\infty} = -\underline{\mathbf{R}}^{-1} \cdot \mathbf{E}_Z \qquad (2)$$

$\mathbf{u}^{\infty}$ is the superficial fluid velocity vector, $\mathbf{E}_Z$ is the unit vector in the vertical direction and $\underline{\mathbf{R}}$ is the resistance matrix which is estimated from the many-body hydrodynamic interactions and the short-range lubrication forces in the Stokesian Dynamics method with periodic boundary conditions. Position and velocity vectors are dimensionless with the particle radius 'a' as the characteristic length and the single particle terminal velocity v_t as the characteristic velocity. The resistance matrix $\underline{\mathbf{R}}$ which is constructed from the particle positions is symmetric, positive-definite and its estimation using periodic boundary conditions is adequately explained by Brady and Bossis [2] and Ichiki and Hayakawa [3]. Using periodic boundary conditions, the hydrodynamic interactions are estimated in all three directions, the long-range forces calculated using the Ewald-summation technique of the mobility matrix [5] and lubrication forces from the lubrication matrix representing the short-range pair-wise repulsive interactions [6].

The instantaneous positions and velocities of the N particles are found out by integrating Eq. (1). For this purpose, we use the fourth-order Runge-Kutta method with a time step of 0.1 and the inversion of the resistance matrix is done using the Cholesky factorization technique. The resistance matrix $\underline{\mathbf{R}}$ and the terminal velocity V are estimated for each time step from the position vector **x** at that time. The simulation parameters are listed in

Table 1. The particles are allowed to move only in the vertical plane although the hydrodynamic interactions are taken into account in all three dimensions.

The direct interparticle forces during fluidization are treated as elastic collisions where the momenta of colliding particles are exchanged at the end of the time step.

3. Simulation of the gas fluidization of FCC ($u^{\infty} = 0.44$ m/s)

The purpose of this simulation was to compare the particle velocities with the experimental measurements on FCC using the Radioactive Particle Tracking (RPT) technique. We start the simulation with a random configuration of the Fluid Cracking Catalyst (FCC) particles of size 70μm. The dimensions of the unit cell are 17.5x50x2 with periodic boundary conditions in all directions representing a small volume in the central portion of a fluidized bed farthest from the distributor and the walls (see Figure 1 for details). Using the Runge-Kutta technique we calculate positions and velocities of all 100 particles for each time step (dt = 0.1) with St = 235 for FCC.

During fluidization, we introduce air with an uniform velocity of 0.44 m/s and track the positions and velocities of all fluidizable particles for each time step. We record every tenth time step upto a maximum of 1000 recorded steps. All simulations were run on an IBM SP2 with a performance of 130 MFlops.

The axial distribution of the time-averaged horizontal and vertical components of the particle velocities obtained from this simulation is compared with those obtained in experiments on radioactive particle tracking of FCC later in Section 7.

4. Simulation of the gas fluidization of FCC (u^{∞} = 0.09 and 0.06 m/s)

In this case, in addition to the 100 fluidizable particles, we have five particles fixed in space at the bottom of the unit cell to represent the distributor where the bubbles would originate. Two gas velocities 0.09 m/s and 0.06 m/s were used in these simulations to compare with the bubble characteristics of a fluidized FCC bed measured experimentally using the fiber-optic method. Here, the unit cell represents a small volume close to the distributor in the experimental bed.

The average bubble size, bubble velocity and area fraction of the bubble phase obtained from the microscopic simulation results are compared with the experimentally measured values in Section 7.

5. Radioactive Particle Tracking Experiment

The experiments were done in a gas-solid fluidized bed as shown in Figure 2. The column was made of a Plexiglass pipe with 152 mm internal diameter and 1500 mm height. Air at room temperature was introduced into the bed through a conical section,

passing through a stainless steel porous plate and a nozzle type air distributor. Air flow rate was measured by an orifice plate connected to a water manometer. A cyclone placed at the air outlet of the column returns the entrained solids back to the bed.

The solids used in the experiments was the Fluid Cracking Catalyst (FCC) having particle size of 70 μm and a density of 1971 kg/m^3. Initial height of the bed was 0.22 m (1.5 times the column diameter).

The tracer was made of a mixture of gold powder and epoxy resin of size 420 μm to be used in the experiment. It was activated in the SLOWPOKE nuclear reactor of École Polytechnique prior to the experiment. The produced isotope ^{198}Au emits γ-rays which are counted by 16 cylindrical NaI(Tl) scintillation detectors on sliding rails. A typical arrangement of the detectors around the fluidized bed is shown in Figure 2. Two personal computers simultaneously register the number of γ-rays detected by each detector in every sampling period of 20 ms. These number of counts are used later to calculate the co-ordinates of the tracer. Details of the system calibration and the inverse reconstruction strategy for tracer position rendition are described by Larachi *et al.* [7, 8]. During the experiment the tracer was placed into the bed to move freely with the other particles inside the bed. Movement of the tracer was then monitored for about 5 hours during which the count rate of the tracer at some 820,000 points were acquired. The bed was then made empty and the tracer was recovered from the solids.

6. Fiber-optic experiment

Fiber-optic experiments were carried out in the same column described in Section 4 having 150 mm in diameter at 20°C under different superficial gas velocities in the bubbling regime of fluidization. The same FCC powder discussed in the radioactive particle tracking study was used in this case as well.

A cross fiber-optic probe [9] with two cross-fiber bunches of 0.8 mm in diameter composed of several small optic fibers of 40 μm diameter is placed at a position of 50 mm from the distributor to measure the local instantaneous voidage. A PV - 4A Particle Velocity Analyzer made by the Institute of Chemical Metallurgy, Chinese Academy of Sciences is employed to get the time series of dynamic local voidage under different operating conditions. More than 20 runs with 60,000 data each were sampled with a sampling frequency of 16 KHz under the operating conditions. The size of bubbles and their rise velocities at the given height were measured as an average of two radial positions one at the centre of the bed and the other at two-thirds the radius of the bed.

7. Results

7.1 Comparison of Stokesian Dynamics results with Radioactive Particle Tracking (RPT)

As explained in Section 3, the particles are first generated randomly in the unit cell. We introduce uniform air flow in the upward direction with a high velocity of 0.44 m/s. In Figure 3 we see a state of the fluidized bed during the 1000 recorded time steps.

Velocity profiles were extracted from the particle trajectories by averaging the 1000 steps for several axial positions. Observe that the entire bed is in a fluidized state in Figure 4 which shows the axial distribution of the x- and z- components of the particle velocity along the bed height obtained from FCC simulations at 0.44 m/s.

As mentioned in Section 3, this unit cell having periodic boundary conditions in all directions represents a small area at the centre of a fluidized FCC bed which has the least influence of the wall or distributor. The axial distribution of the average particle velocities computed from the Stokesian Dynamics simulation is therefore a representative zoom area (dotted box) at the centre of the experimental fluidized bed described in Section 4 which is farthest from the wall, distributor and the bed surface. Using this assumption, we ensure comparison of simulation and experiment at the same dimension scale. It is difficult to simulate conditions near the distributor at the bottom of the bed due to very high velocity of the gas flow. In fact, an attempt to simulate a unit cell with fixed particles at its bottom to represent a small volume above the distributor proved to be unproductive as particles carried up by the high gas flow (0.44 m/s) were collected against the fixed particles of the periodic image directly above the central cell . The figure also shows experimental results of the x- and z-components of the particle

velocities as measured by the radioactive particle tracking technique along the bed height at a radial distance of 1 cm from the axis of the bed. The particle velocities in both cases are rendered dimensionless using the characteristic single particle terminal velocity.

Comparing the x- and z-components of the particle velocities at the central portion of the experimental FCC bed with the simulation results obtained from the Stokesian Dynamics method indicates a good agreement between them. The particles appear in both cases to have a dominant upward motion compared to the lateral movement at the high gas velocity.

7.2 *Comparison of Stokesian Dynamics results with Fiber-optic experiments*

Comparison of the Stokesian Dynamics simulation results of a bubbling bed were made with measurements of bubble characteristics (bubble size and velocity) based on the fiber-optic technique explained in Section 6. In this case, we need fixed particles at the bottom of the unit cell to act as the distributor where the bubbles would originate. The ratio of the height of the fixed bed that the 100 simulated particles would have formed to the width of the unit cell (17.5) is 1.3. Larger heights of the unit cell would require cell widths larger than 17.5 to avoid slugging at the top which implies more number of simulated particles and hence longer computational times.

Using the information of instantaneous particle positions and velocities, the void spaces arising in the bed are identified as bubbles and the motion of the bubbles are followed starting from their birth at the distributor to their explosion at the surface of the bed. The history of each bubble viz. their size, velocity can thus be extracted from the simulation data.

Figure 5 shows a snapshot of periodic images of the bubbling bed of FCC at 0.09 m/s. Notice that a few particles can be entrained in the rising bubble and the bubble is 'grown' as opposed to its initial size near the distributor where it is comparable to the size of the particle.

Comparing the results of the simulation and experimental measurements of the characteristics of the bubbling bed of FCC particles at an air velocity of 0.09 m/s, in Figure 6. we note that the scale of comparison is not the same, i.e., the sizes of the unit cell and the experimental bed differ considerably. Here, we assume that the unit cell represents a small portion of the experimental bed at the proximity of the distributor and far from the wall. An indirect quantitative comparison between the unit cell and the experimental set-up is possible by bridging the experimental results observed at the height of 50 mm along the axis of the bed with simulation results using bubbling bed models as discussed below.

Comparing the results of experiment and simulation, we arrive at the following report:

Here bubble sizes have been rendered dimensionless as is usual in Stokesian Dynamics by the particle radius 'a' and the bubble rise velocity by the single particle terminal velocity, v.

Average bed porosity at 0.09 m/s:

The average bed porosity at a height of 50 mm from the distributor is 0.55 in the case of simulation and 0.52 in the case of the experiment. The porosity is averaged radially over two positions, one at the center of the bed and the other at two-thirds the radius of the bed.

Bubble characteristics at 0.09 m/s:

The dimensionless bubble size estimated from simulation results has a value of 18 at a height of 35 (equivalent of 1.2 mm from the distributor) as shown in the inset of the bubble diameter vs. height plot in Figure 6 for the unit cell. The fiber-optic measurement at this higher velocity at a height of 50 mm from the distributor gave a dimensionless bubble size of 474.86. This is explained by the increase in the size of the rising bubbles as well as due to bubble coalescence. However, the simulation result agrees well with the model for predicting bubble size near the distributor [10], which gives a value of 55 for the given bed depicted in Figure 6.

We bridge the simulation results near the distributor with the experimental results at a height of 50 mm using common bubbling bed models. Using the Rowe model for bubble size as a function of the bed height [11], we calculate a bubble size of 19.8 close to our simulation result. The Rowe model shown below and its agreement with the simulation prediction of the bubble size near the distributor is shown in Figure 6.

$$d_b = g^{-0.25} z^{0.75} \left(u^{\infty} - u_{mb}\right)^{2.5} \tag{3}$$

Comparing the bubble rise velocities in both experiment and the bubbling bed model, we find the experimental value to be close to that predicted by the Kunii-Levenspiel model [10] at 50 mm from the distributor. As seen in Figure 6, the simulation results (inset) agree well with the model prediction of 0.32.

$$u_b = 1.55\left\{\left(u^{-} - u_{mf}\right) + 14.1\left(d_b + 0.005\right)\right\}^{1} d_t^{0.32} + u_{br} \tag{4}$$

$$u_{br} = 0.711\left(g d_b\right)^{0.5} \tag{5}$$

Average bed porosity at 0.06 m/s:

An average bed porosity of 0.49 was estimated from the Stokesian Dynamics results while the radially averaged fiber-optic measurements yielded a value of 0.49 as well.

Bubble characteristics at 0.06 m/s:

At this lower air velocity, we compare the bubble size and their rise velocity obtained in the simulation and the fiber-optic experiment in Figure 7. The insets show the bubble characteristics in the unit cell. As in the above case, the unit cell represents an elemental area at the centre of the distributor. The average bubble size obtained by the Stokesian Dynamics method is 12 and the range of the bubble size agrees well with the bubble size of 22.42 predicted by the bubble size model applicable near the distributor [10]. The bubble size obtained by the fiber-optic method is 403.43 which was measured at a height of 50 mm. The Rowe model yields a value of 12.71. Interestingly, the bubble rise velocity estimated from the simulation is very close to the Kunii-Levenspiel result as shown in the figure. The experimental bubble rise velocity at the height of 50 mm is close to the model prediction.

From the results of comparison with bubbling bed models, we infer that the Stokesian Dynamics method reasonably predicts the bubble size and bubble rise velocities (at the proximity of the distributor).

Comparison between two-dimensional and three-dimensional beds:

It is to be noted that the Stokesian Dynamics simulation of bubbling beds is performed in a pseudo two-dimensional bed while experiments and the Kunii-Levenspiel model are prescribed for three-dimensional bubbles. In two-dimensional beds, the Davidson theory assumes the bubble shape to be cylindrical [12]. It however is reported to overestimate the penetration in actual two-dimensional bubbles (cloud penetration is defined as the

ratio of cloud radius to the bubble radius). Using the bubble rise model for two-dimensional bubbles [13] and the bubble size measured in the simulation at the gas velocity of 0.09 m/s. we obtain a bubble rise velocity of 0.403 which is close to both the three-dimensional model as well as the simulation result (Figure 6). The same conclusion is reached at the gas velocity of 0.06 m/s where the two-dimensional model yields a bubble rise velocity of 0.3781 again close to simulation results. When the bubble size is as small as obtained in the simulations, we observe little deviation between the two-dimensional and three-dimensional bubble characteristics compared to simulations. As pointed out in Section 2 that even though the unit cell is pseudo two-dimensional, hydrodynamic interactions are estimated in all three directions. Brady and Bossis [2] have reported that pseudo two-dimensional simulations as well as the Ewald-summation technique are computational conveniences with the physics of the suspension being adequately described by the hydrodynamic interactions even in the absence of particle motion in the third dimension. A recent paper by Morris and Brady [14] justifies the use of pseudo two-dimensional cells in describing the pressure-driven flow of suspensions using Stokesian Dynamics. Here the suspension temperature (mean square of the scalar particle velocity fluctuations) is not affected by the increase in the thickness of the unit cell beyond the particle diameter. The influence of particle motion perpendicular to the plane of flow might cause deviations from the two-dimensional case (both model and simulation) when the system size is large (cell size > $O(10^2)$).

Structure of a fluidized bed

In addition to obtaining the characteristics of the fluidized bed that has been compared with experiments and bubbling bed models, a method of quantifying the structure of the bed using simulations is the estimation of the pair-distribution function.

We compared the structure of the fluidized bed with that of a fixed bed using the pair-distribution function G(r) which is the probability density of finding a particle at a distance r from a given particle [2]. Figure 8 compares the pair-distribution function G(r) in the horizontal and vertical directions both in a fixed as well as the fluidized bed at 0.09 m/s obtained from the instantaneous particle positions of the 100 particles. The marked difference of a fluidized bed (represented in Figure 5) from the fixed bed is that G(r) is continuous which indicates a non-definite structure due to the mixing of particles throughout the bed.

8. Conclusions

We simulate the behaviour of gas fluidized FCC using the Stokesian Dynamics method. Initially, we simulate the simulation of FCC powder following the work of Ichiki and Hayakawa [4] using 100 fluidizable particles of 70 μm size. In this case, we considered particle collisions to be elastic and the gas velocity at 0.44 m/s. We observe the finely fluidized state of the bed and computed the x- and z-components of the time-averaged particle velocities along the height of the bed. A radioactive particle tracking experiment was carried out with the air fluidization of FCC under the same conditions and the

velocity of the tracer was followed at various positions along the height of the bed. The unit cell of the simulation was assumed to be a small area at the centre of the experimental bed which is least influenced by the extremities of the bed. Comparing the Stokesian Dynamics results of particle velocities and the tracer velocities, we observe a good agreement between the simulation and the radioactive particle tracking method.

Two other simulations were carried out with the FCC powder at 0.09 m/s and 0.06 m/s respectively in the same unit cell. In this case, the characteristics of the bubbling bed such as bubble size, bubble rise velocity and areal fraction of the bubbles were extracted from the instantaneous positions and velocities of the particles. For comparison, two experiments were carried out with FCC at these two velocities and the fiber-optic technique was used to find these characteristics of the bubbling bed at an axial position in the bed.

Assuming the simulated unit cell represents a miniature area at the bottom of the axis of the experimental fluidized bed, comparison of the bubbling bed characteristics indicated that at both the gas velocities, the simulation values of bubble size and velocity are in agreement with the bubbling bed models at the vicinity of the distributor while the experimental measurements of these quantities conform well with model predictions. The bubble characteristics of the simulated bed are in agreement with two-dimensional bubble models and it is argued that for small bubble sizes as obtainable in the simulations, the difference between two-dimensional and three-dimensional models is not significant.

The structure of a fluidized bed was differentiated from that of a fixed bed using the pair-distribution function. This function is continuous for a fluidized bed unlike a fixed bed quantifying the spatial distribution of particles in the fluidized state having a non-definite structure.

Within the current assumptions on the quantitative comparison of experimental and simulated fluidization of powders, we conclude that the Stokesian Dynamics method captures the essential behavior of fluidized beds. The major challenge/constraint that we face in the experimental comparison of the simulation of fluid-particle systems using the Stokesian Dynamics method described in this paper is the computational time which limits the size of the simulation cell. However, with revolutionary technologies in computer processing speed expected in the near future, this problem is expected to be 'partially' overcome.

9. List of Symbols

a	Particle radius
d	Diameter
G	Pair-correlation function
g	Gravitational acceleration
m	Mass of particle
N	Total number of simulated particles
Nm	Number of fluidizable particles
Nf	Number of fixed (distributor) particles
r	Interparticle separation
t	Time
U	Particle velocity vector
u^{∞}. uinf	Superficial velocity of fluid
x	Position vector of particles (x_x. x_y. x_z)
x.y.z	Coordinate axes

Subscripts

B	Bubble
br	Single bubble
mb	Minimum bubbling condition

mf	Minimum fluidization condition
p	Particle
t	Tube (bed)
x,y,z	3D vector components

Greek letters

ρ	Linear density (bulk density/solid density)
v	Single particle terminal velocity (characteristic velocity)
μ	Viscosity of the fluid

Acknowledgements

Deiva Venkatesh is deeply thankful to Navid Mostoufi for his experimental assistance on radioactive particle tracking and Dr. Cui Heping for actively assisting in the fiber-optic studies. He also expresses gratitude to Dr. Kengo Ichiki, Kyoto University, Kyoto, Japan for his continuous help during this work.

10. References

[1] D.Geldart, *Powder Technol.* 7 (1973) 285.

[2] Brady J.F. and Bossis G., *Annu. Rev. Fluid Mech.*, 20 (1985) 111.

[3] Ichiki K. and Hayakawa H., *Phys. Rev. E*, 52-1 (1995) 658.

[4] Ichiki K. and Hayakawa H., *Phys. Rev. E*, 57-2 (1998) 1990.

[5] Beenakker C.W.J., *J. Chem. Phys.* 50 (1986) 1581.

[6] Jeffrey D.J. and Onishi Y.J., *J. Fluid Mech.*, 139 (1984) 261.

[7] Larachi F., Kennedy G. and Chaouki J., *Nuclear Instruments and Methods in* Physics Research A 338 (1994) 568.

[8] Larachi F., Cassanello M., Chaouki J. and Guy C., *AIChE Journal* 42-9 (1996) 2439.

[9] Reh and Li, Circulating Fluidized Bed Technology III, eds: Basu P., Horio M. and Hasatani M, Pergamon, Oxford (1991) 163.

[10] Kunii D. and Levenspiel O., *Fluidization Engineering*, Second Edition, 1991.

[11] Rowe P.N., *Chem. Eng. Sci.*, 31 (1976) 285.

[12] Davidson J.F. and Harrison D., *Fluidised Particles*, Cambridge Univ. Press (1963).

[13] Cheremisinoff N.P. and Cheremisinoff P.N., *Hydrodynamics of Gas-Solids Fluidization*, Gulf Publishing Co. (1984).

[14] Morris J.F. and Brady J.F., *Int. J. Multiphase Flow*, 24-1 (1998) 105 .

Powder properties	
d	Particle diameter
a	Particle radius (characteristic length)
ρ_P	Solid density
v	Single-particle settling velocity
Fluid properties	
ρ_f	Fluid density
μ_f	Fluid viscosity
Bed properties	
L_X	Length
L_Y	Width
L_Z	Thickness
Dimensionless numbers	
Re	Reynolds number
St	Stokes number
Simulation parameters	
dt	Time step
Nr	Number of recordings

Table 1 Fluidized System and Simulation parameters

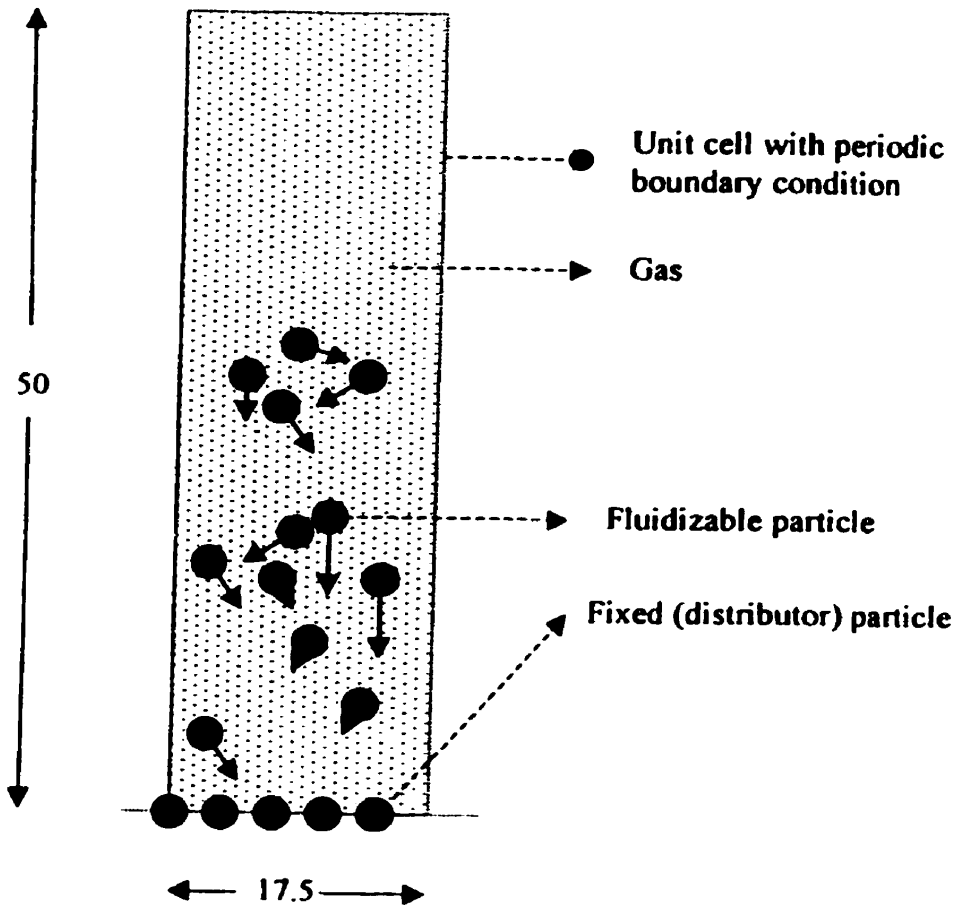

Figure 1 Gas fluidized fine powder bed – Unit cell with periodic boundary condition

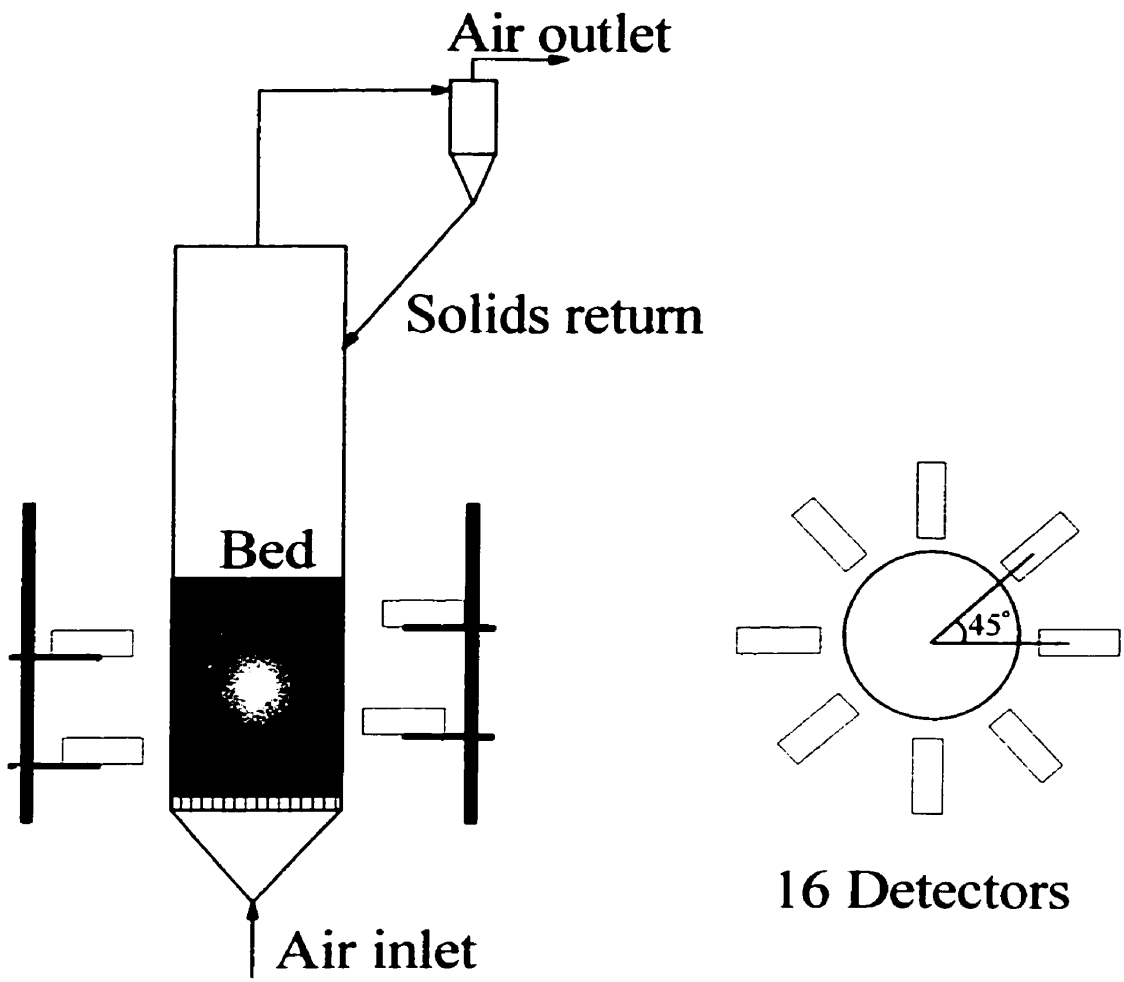

Figure 2 Radioactive particle tracking - Experimental set-up and typical configuration of the detectors

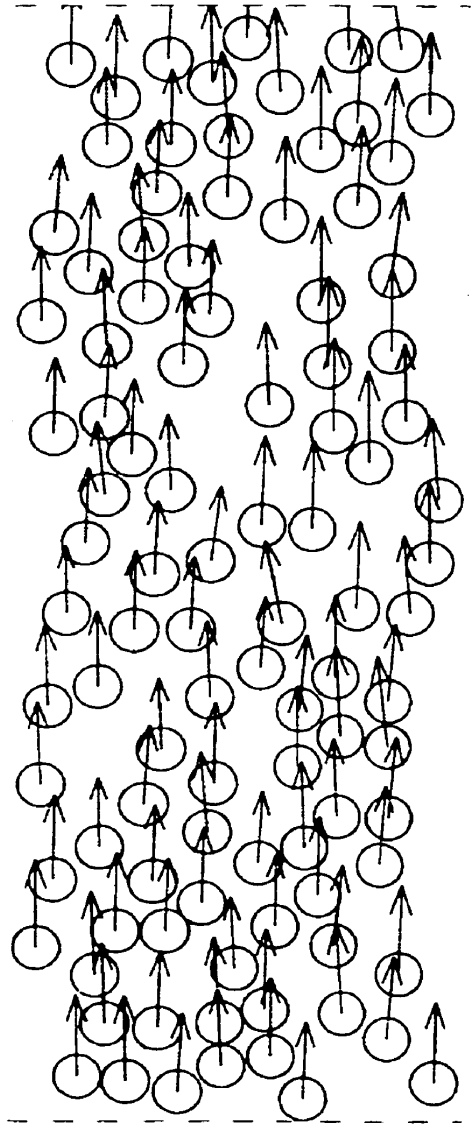

Figure 3 Stokesian Dynamics simulation of high-velocity fluidization (N = Nm = 100, u^{∞} = 0.44 m/s)

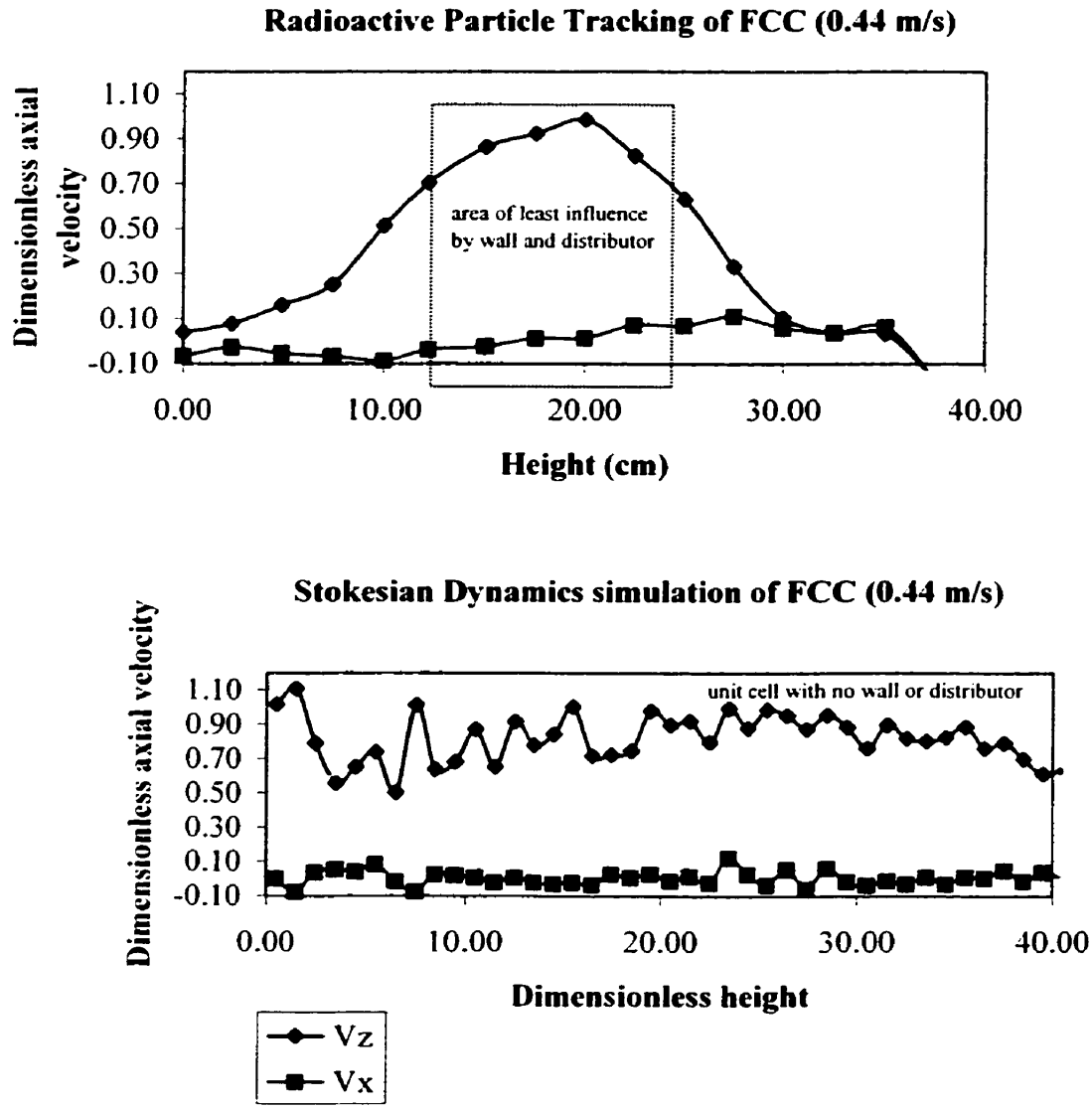

Figure 4 Comparison of particle velocities - Stokesian Dynamics vs Radioactive particle tracking (N = Nm = 100, u^{∞} = 0.44 m/s)

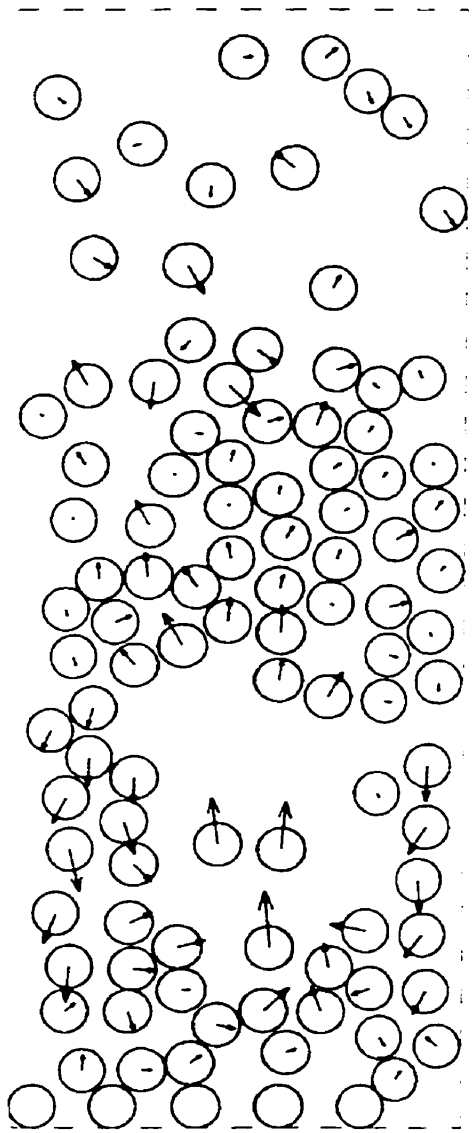

Figure 5 Stokesian Dynamics simulation of bubbling beds (Nm = 100, Nf = 5)

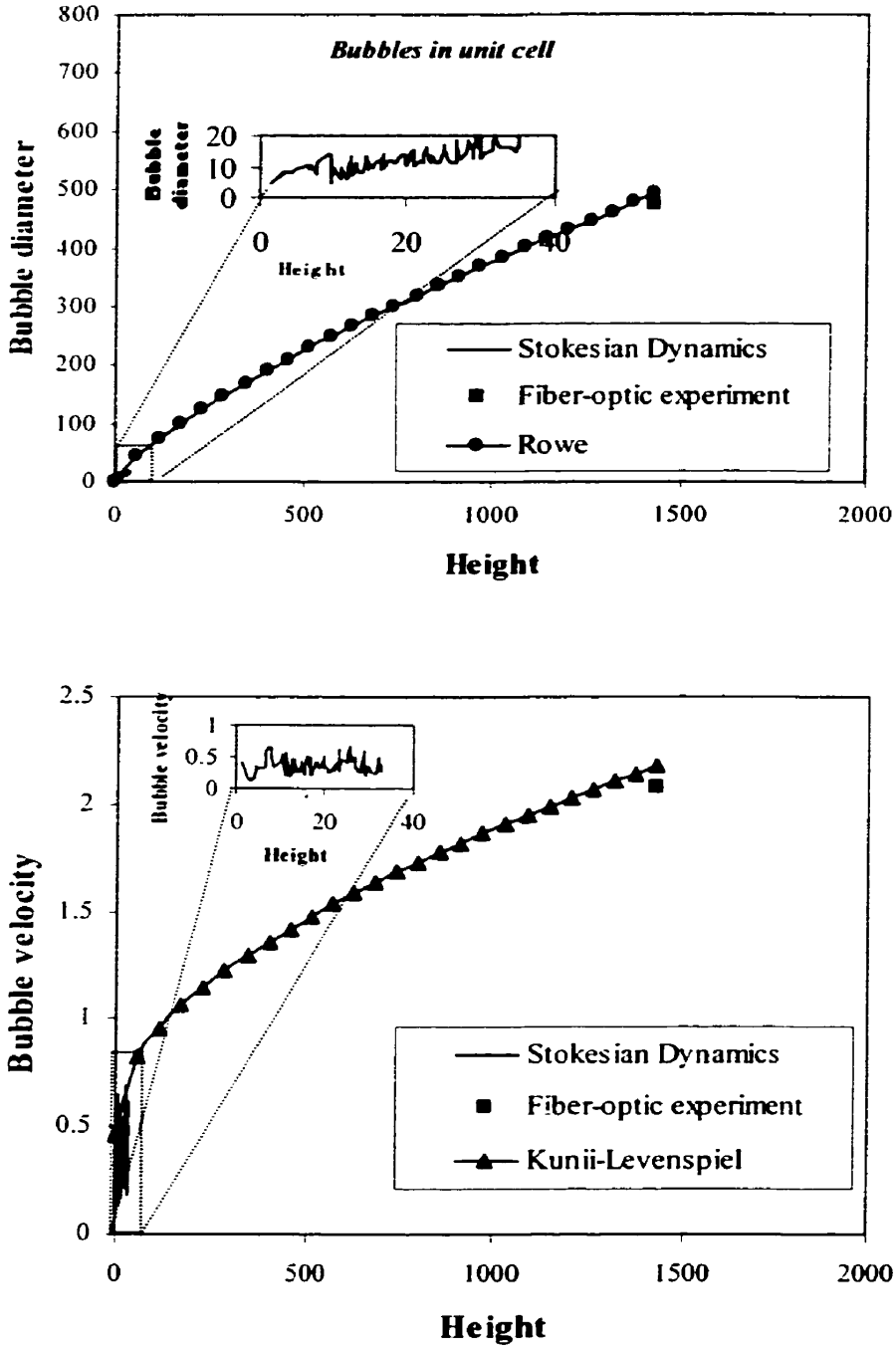

Figure 6 Comparison of bubble characteristics - Stokesian Dynamics vs Fiber-optic experiments (Nm = 100, Nf = 5, u^{∞} = 0.09 m/s)

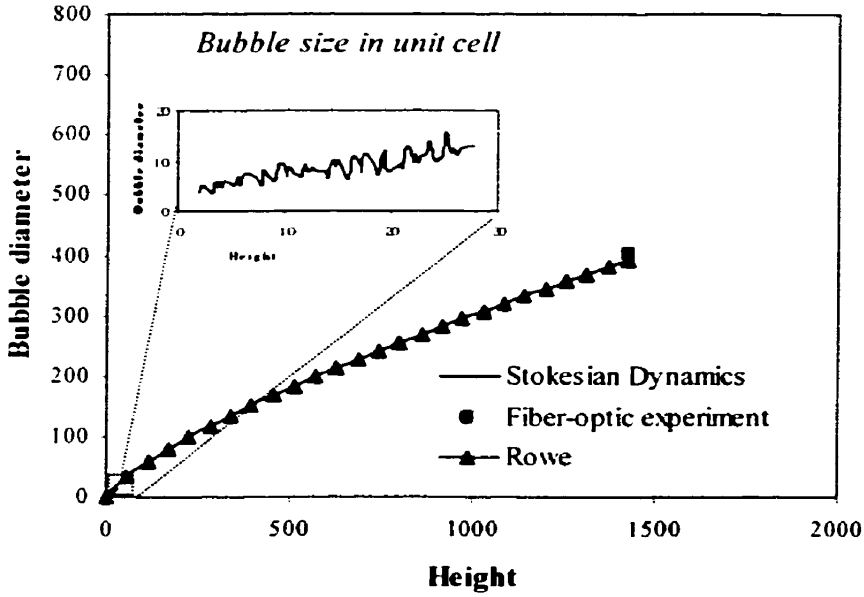

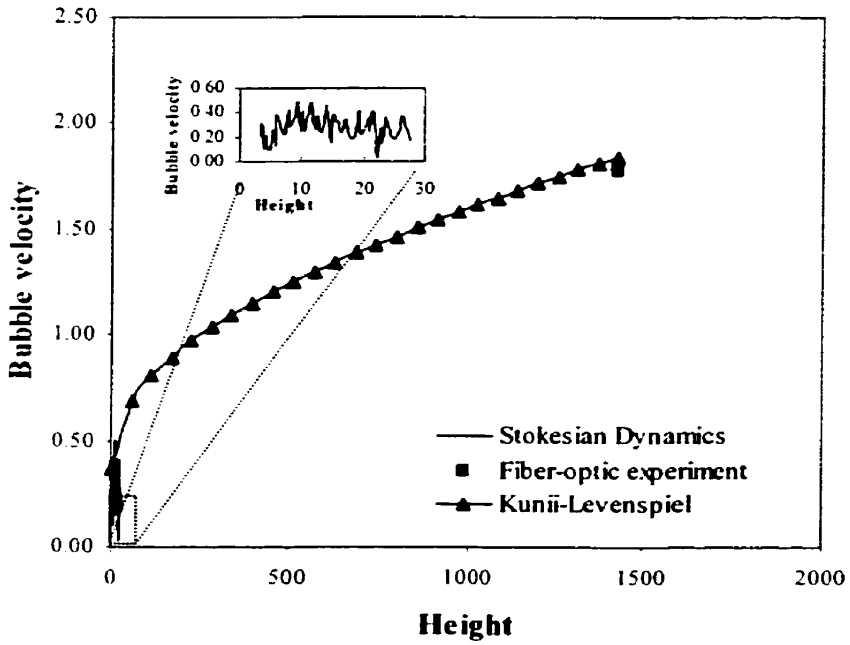

Figure 7 Comparison of bubble characteristics - Stokesian Dynamics vs Fiber-optic experiments (Nm = 100, Nf = 5, $\bar{u}$ = 0.06 m/s)

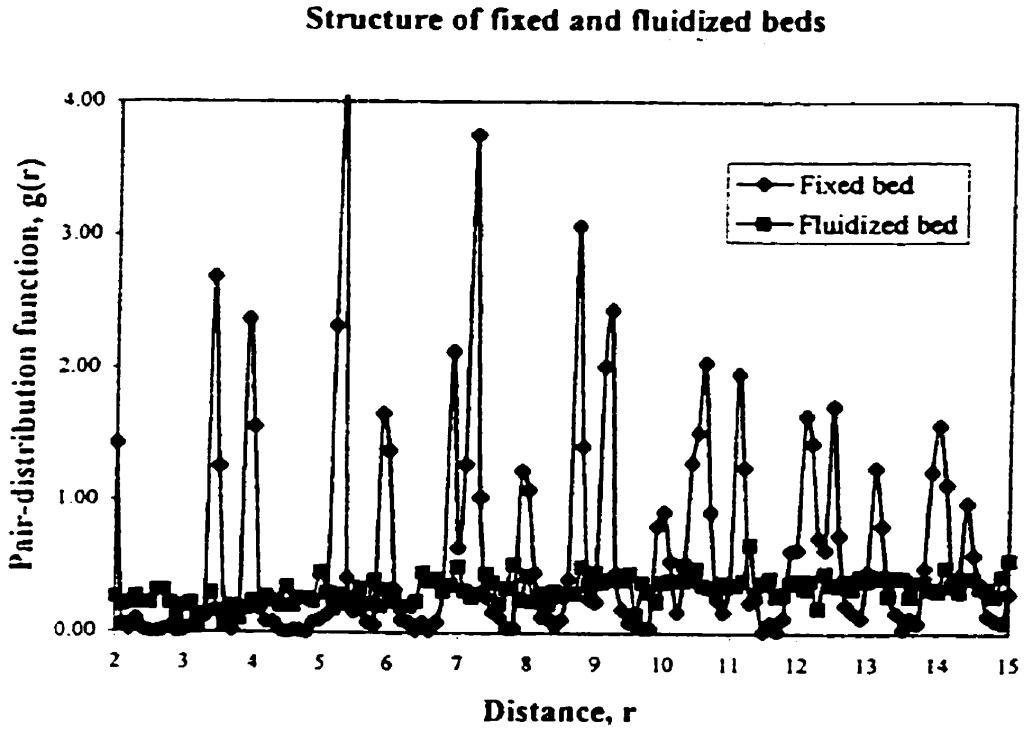

Figure 8 Structures of fluidized bed

APPENDIX 3: MORE INFORMATION ON CHAPTER 3

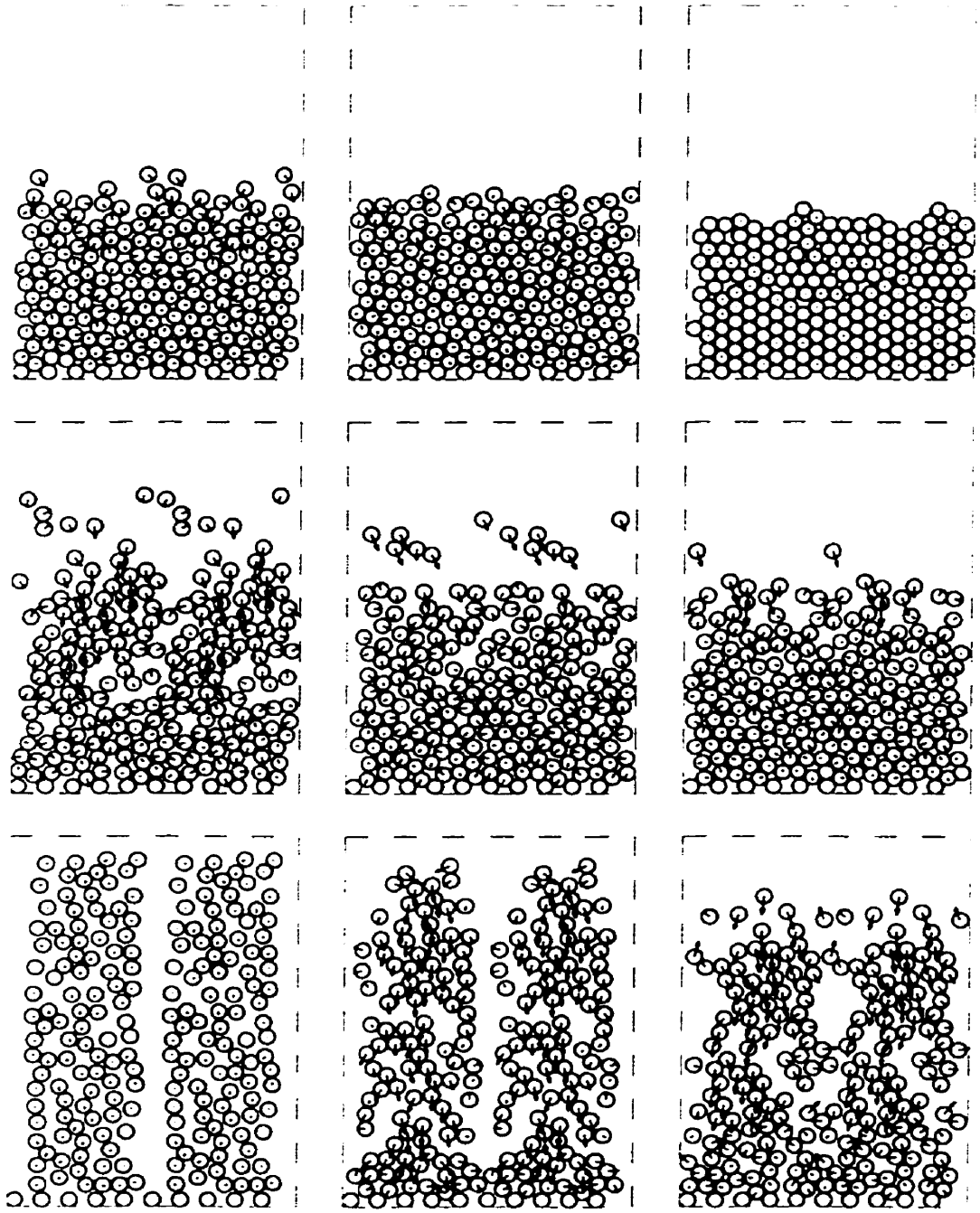

Figure 3.1.8. Sequence of the simulation of sedimentation with cohesive particles at St=10. Related times of the frames from lower left to upper right are 0, 10, 20, 30, 40, 50, 60, 70, and 170 in dimensionless units respectively. The Lennard-Jones parameters of m, n, $S_{l\text{-}0}$, F_{max} are equal to 2, 1, 0.05, and 5 respectively.

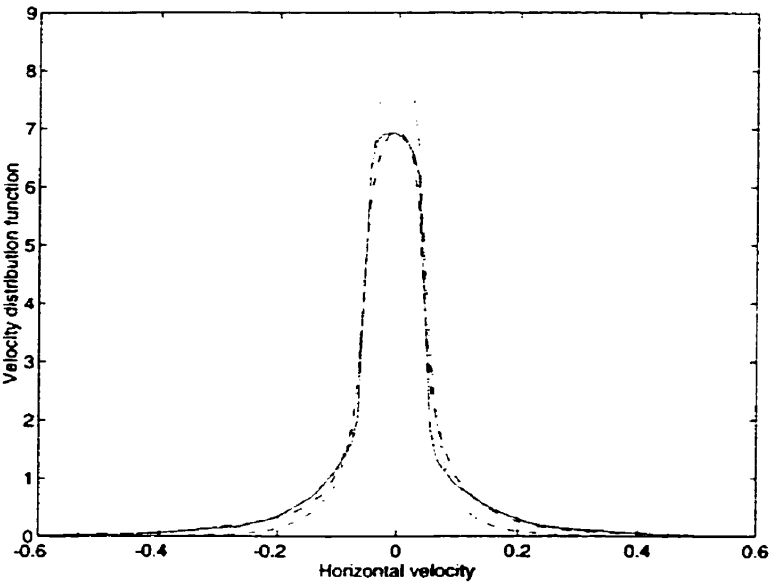

Figure 3.1.9. Velocity distribution of horizontal component of velocity in sedimentation. Solid line is for St=1, dash-dotted line for St=10, dashed line for St=100

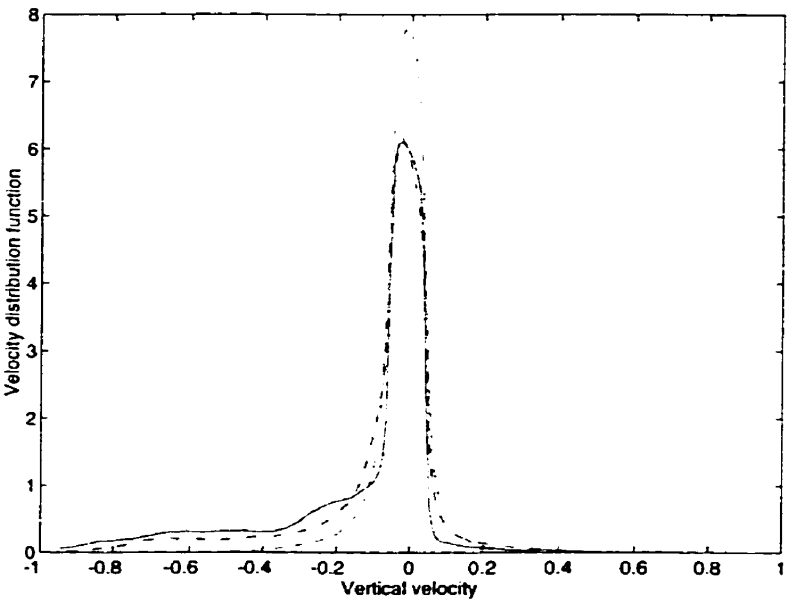

Figure 3.1.10. Velocity distribution of vertical component of velocity in sedimentation. Solid line is for St=1, dash-dotted line for St=10, dashed line for St=100

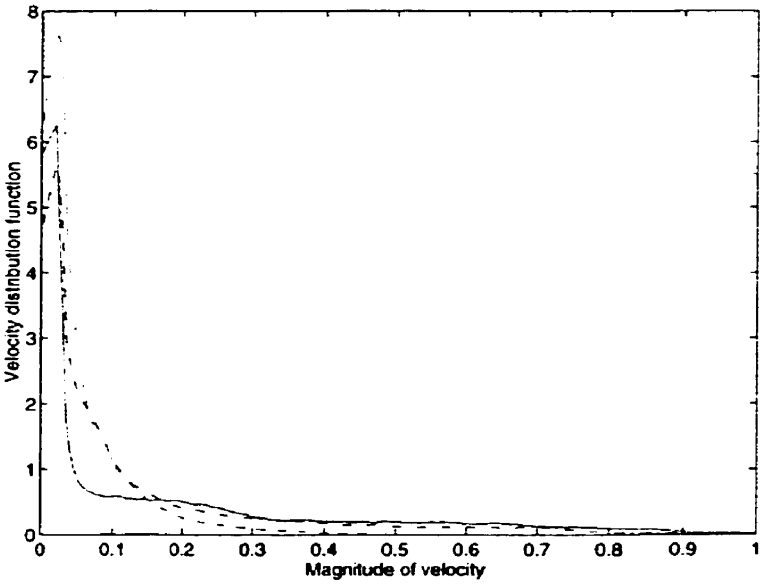

Figure 3.1.11. Distribution of magnitude of velocities of particles in sedimentation. Solid line is for St=1, dash-dotted line for St=10, dashed line for St=100

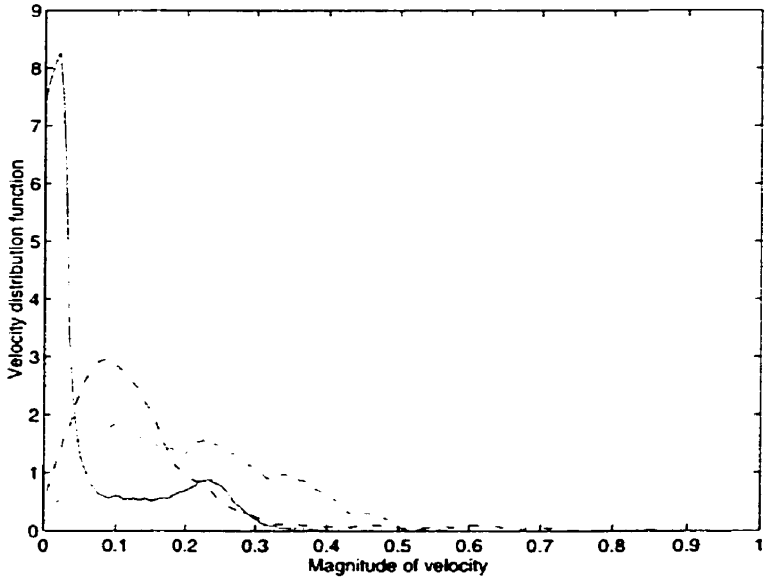

Figure 3.1.12. Distribution of magnitude of velocities of particles in sedimentation at time=60. Solid line is for St=1, dash-dotted line for St=10, dashed line for St=100

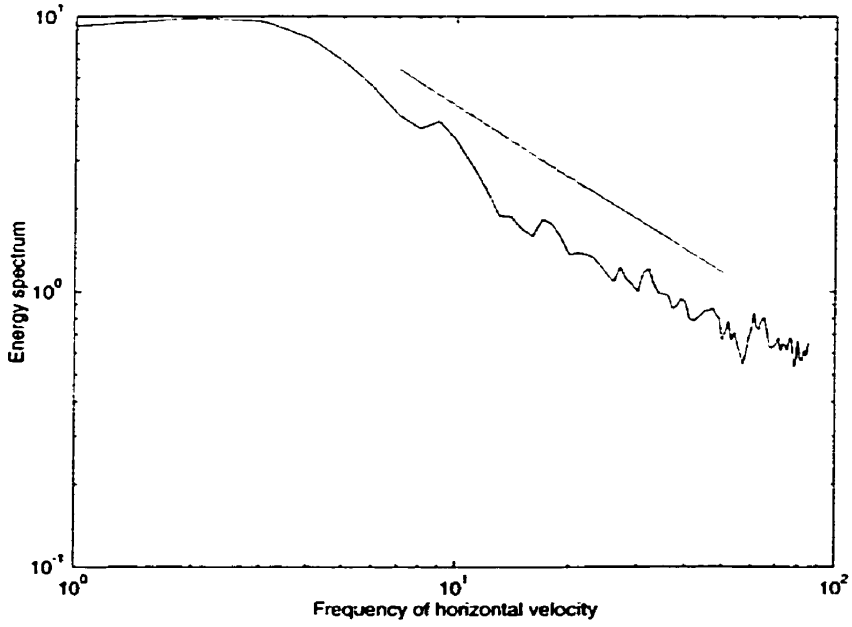

Figure 3.1.13. Energy spectrum of horizontal components of velocities of particles in sedimentation at St=10

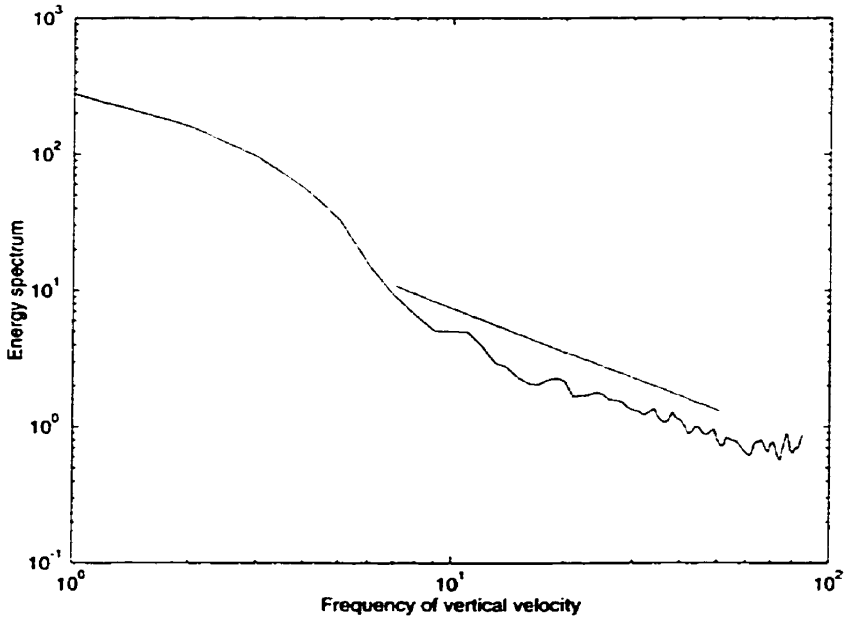

Figure 3.1.14. Energy spectrum of vertical components of velocities of particles in sedimentation at St=10

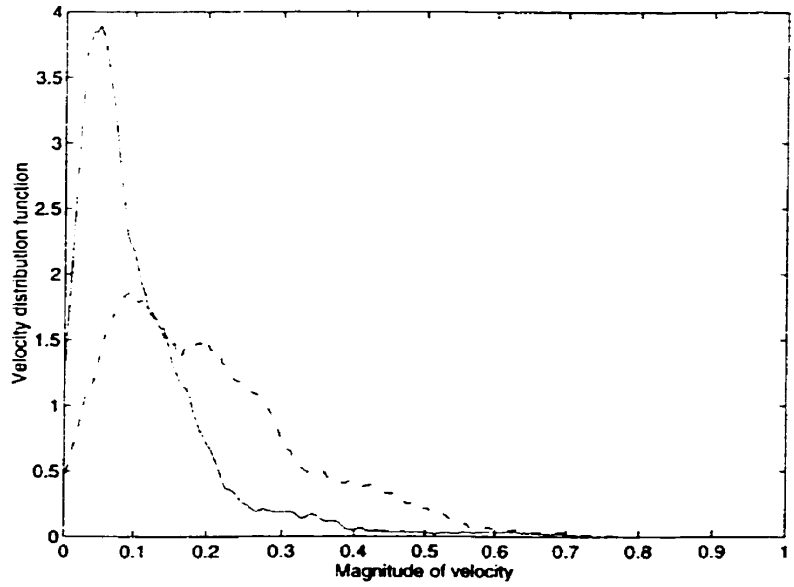

Figure 3.2.18. Distribution of magnitude of velocities of particles in fluidized bed with fixed particles at St=10 and u^{∞}=0.2. Solid line is related for the time when there is no bubble, and dash-dotted line is related for the time when there are bubbles in the bed

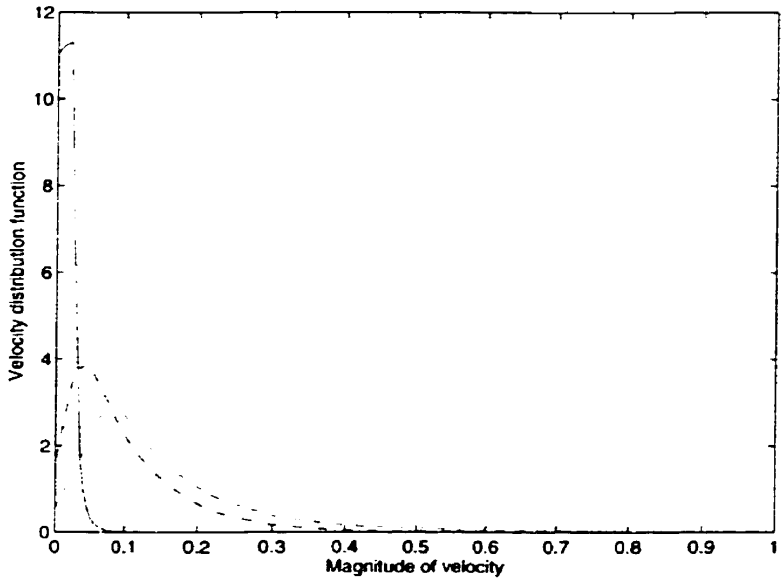

Figure 3.2.19. Distribution of magnitude of velocities of particles in fluidized bed with fixed particles at St=10. Solid line is for u^{∞}=0.1, dash-dotted line for u^{∞}=0.15, dashed line for u^{∞}=0.2, and dotted line for u^{∞}=0.3.

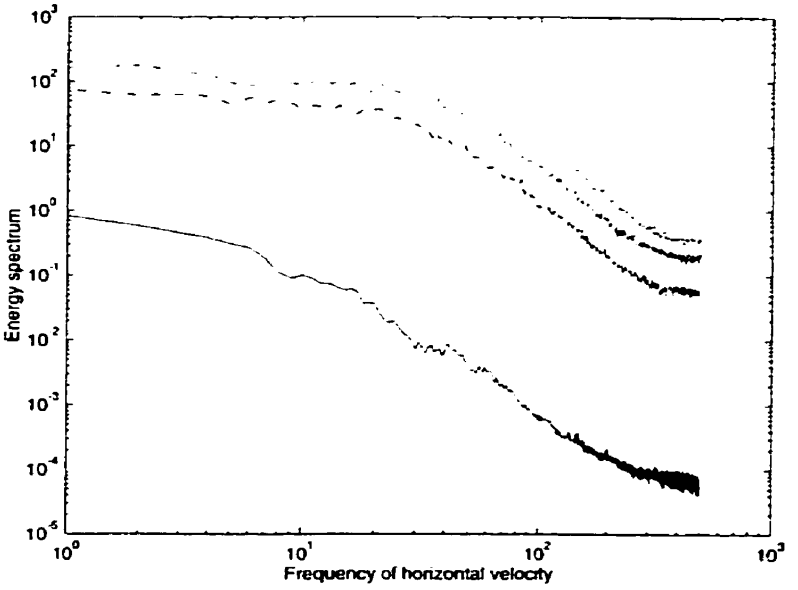

Figure 3.2.20 Energy spectrum of horizontal component of velocity in fluidized bed with fixed particles at St=0.5. Solid line is for u^{∞}=0.1, dash-dotted line for u^{∞}=0.15, dashed line for u^{∞}=0.2, and dotted line for u^{∞}=0.3.

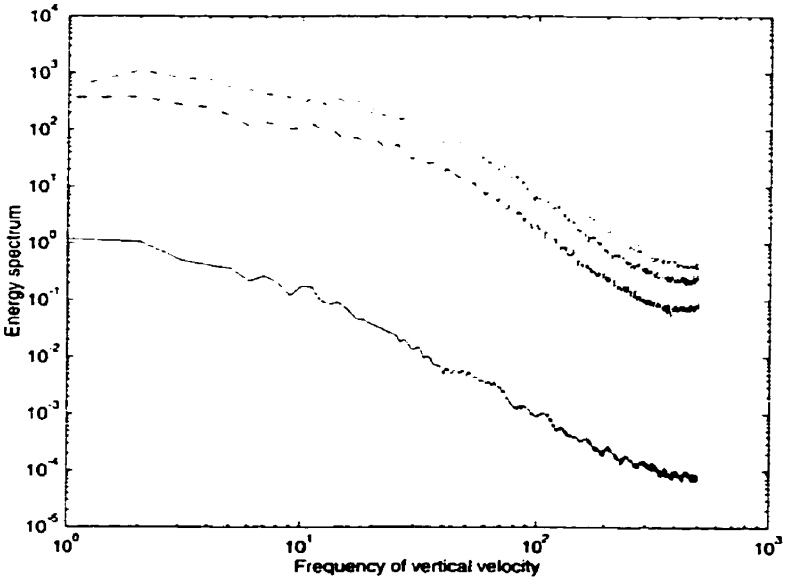

Figure 3.2.21 Energy spectrum of vertical component of velocity in fluidized bed with fixed particles at St=0.5. Solid line is for u^{∞}=0.1, dash-dotted line for u^{∞}=0.15, dashed line for u^{∞}=0.2, and dotted line for u^{∞}=0.3

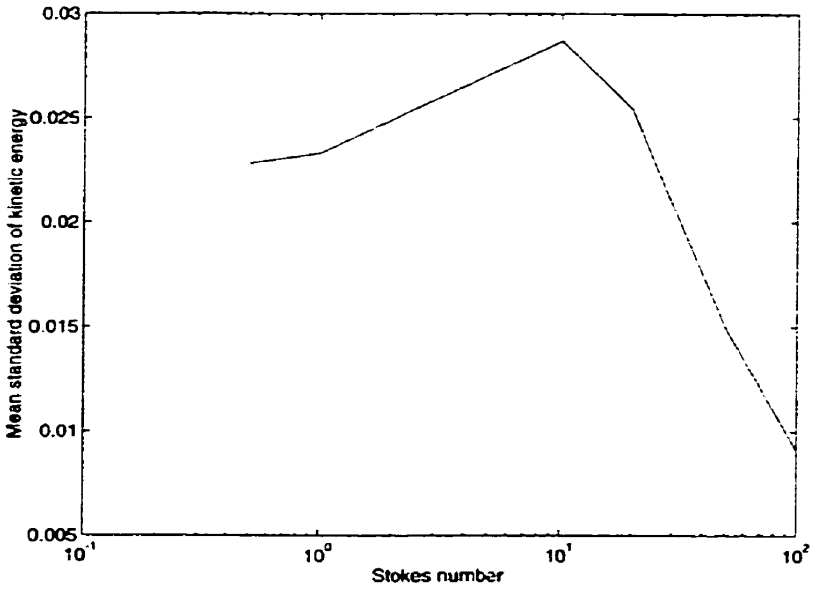

Figure 3.2.22 Mean standard deviation of kinetic energy per particle in fluidized bed with fixed particles at u^{∞}=0.2

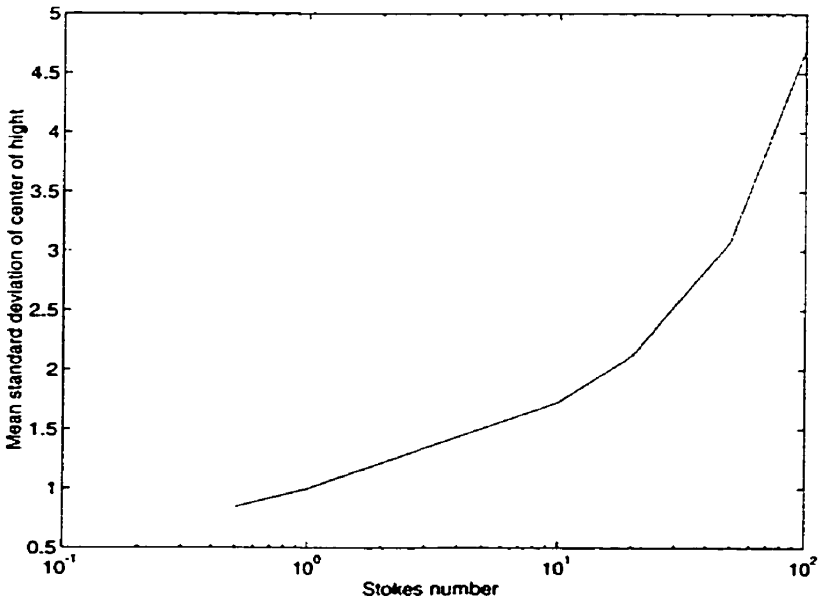

Figure 3.2.23 Mean standard deviation of height of center of mass of particles in fluidized bed with fixed particles at u^{∞}=0.2

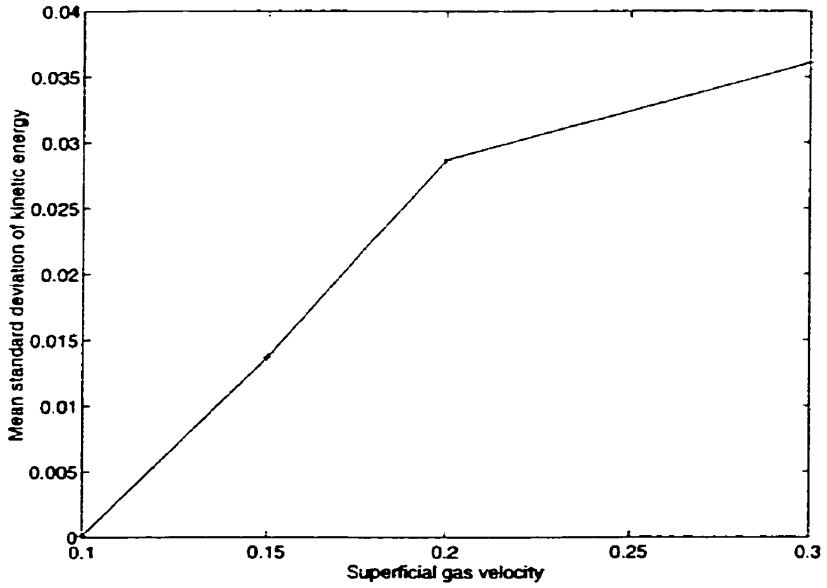

Figure 3.2.24 Mean standard deviation of kinetic energy per particle in fluidized bed with fixed particles at St=10

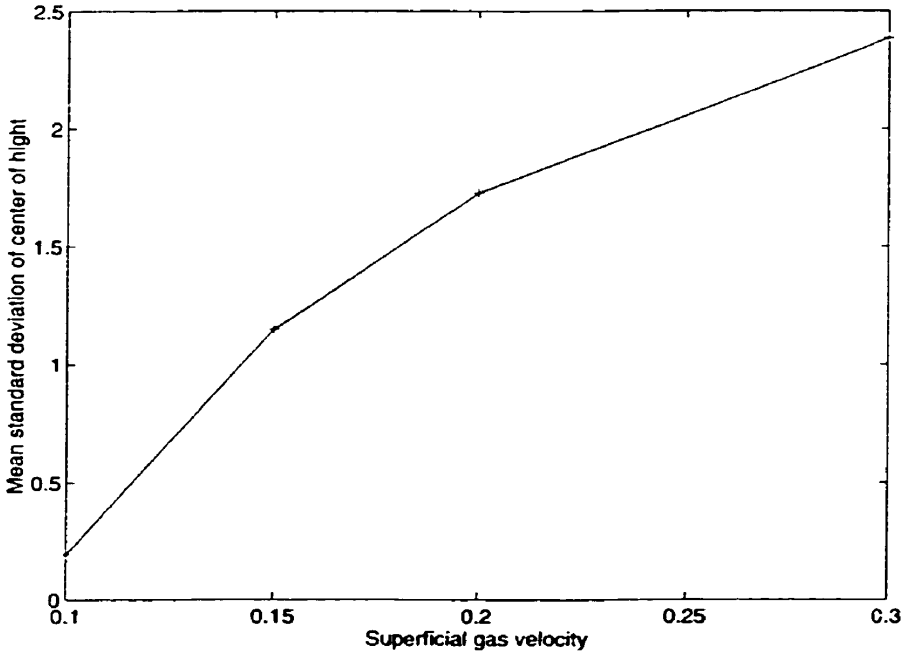

Figure 3.2.25 Mean standard deviation of height of center of mass of particles in fluidized bed with fixed particles at St=10

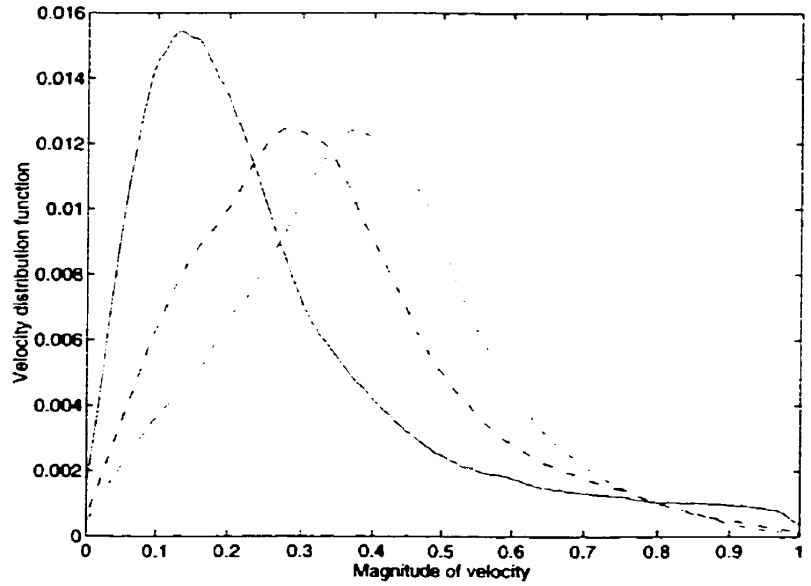

Figure 3.3.8. Distribution of magnitude of velocities of particles in fluidized bed without fixed particles at St=15 Solid line is for u^{∞}=0.3, dash-dotted line for u^{∞}=0.5, and dashed line for u^{∞}=0.6.

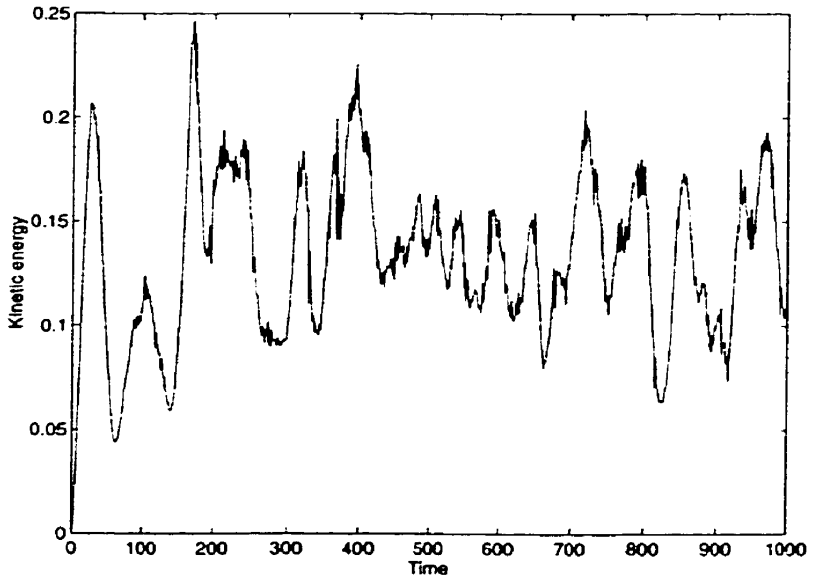

Figure 3.3.9. Kinetic energy per particle in fluidized bed without fixed particles at St=15 and u^{∞}=0.3.

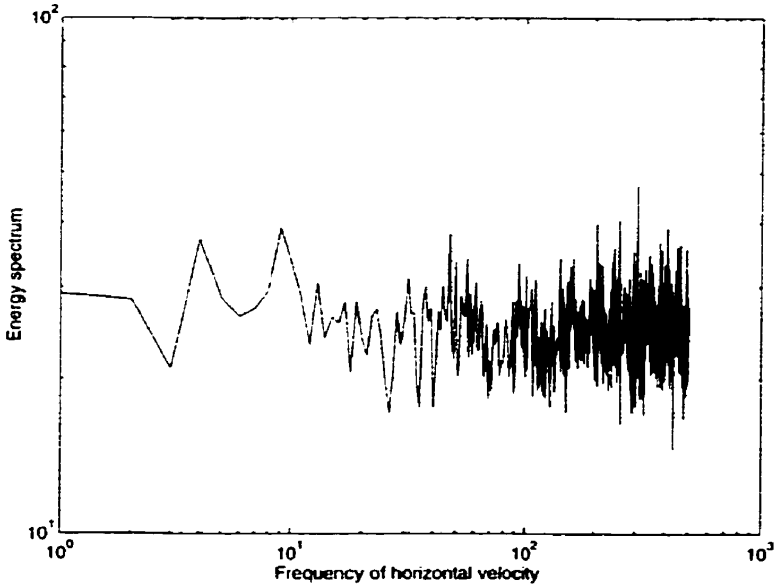

Figure 3.3.10. Energy spectrum of horizontal component of velocities of particles in fluidized bed without fixed particles at St=15 and u^{∞}=0.3.

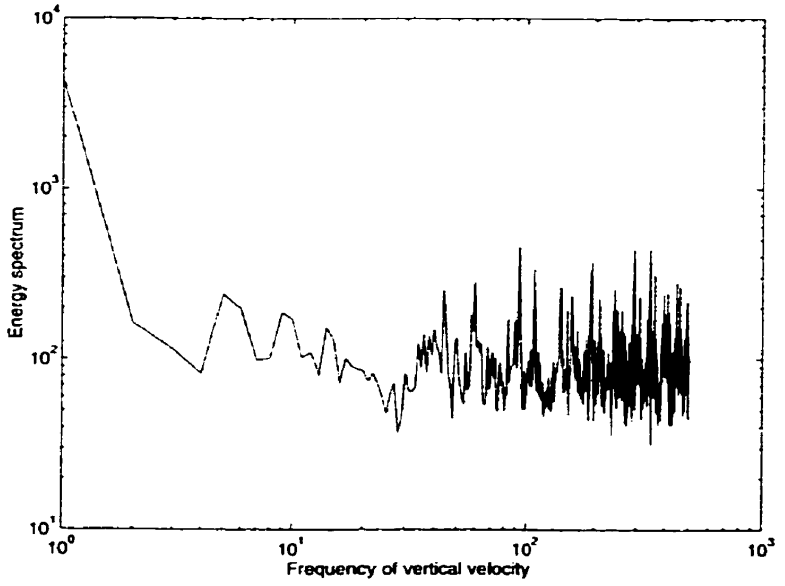

Figure 3.3.11. Energy spectrum of vertical component of velocities of particles in fluidized bed without fixed particles at St=15 and u^{∞}=0.3.

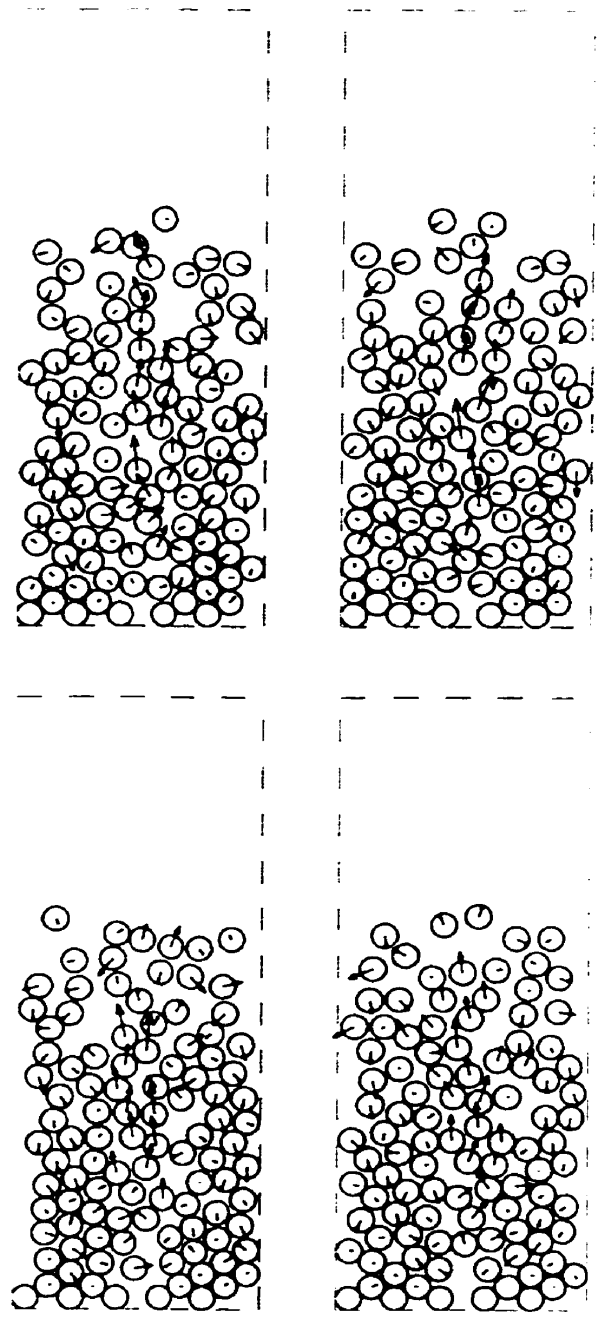

Figure 3.4.8. Sequence of the simulation of spouted bed at St=10 and u^{*}=0.6 superficial gas velocity. Related times of the frames from lower left to upper right are 310, 320, 330, and 340 in dimensionless units respectively.

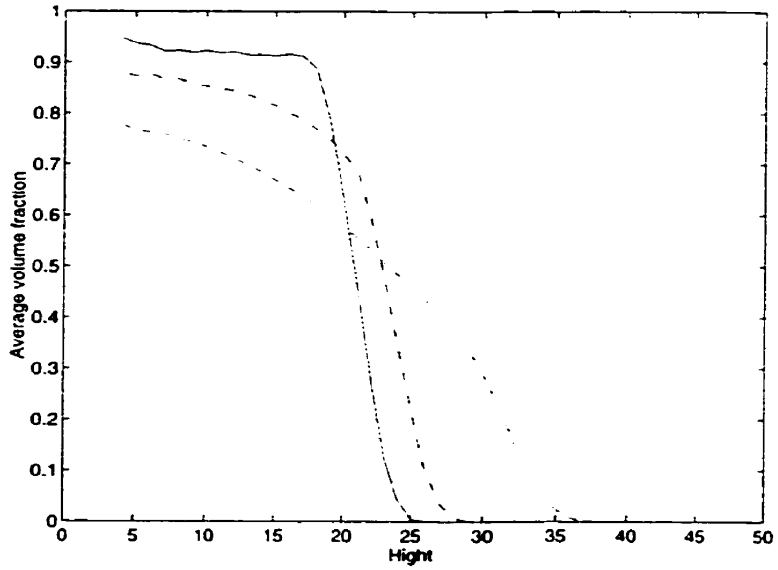

Figure 3.4.9 Average volume fraction of particles along the cell height in spouted bed at St=10. Solid line is for u^{∞}=0.2, dash-dotted line for u^{∞}=0.3, dashed line for u^{∞}=0.6, and dotted line for u^{∞}=1.3.

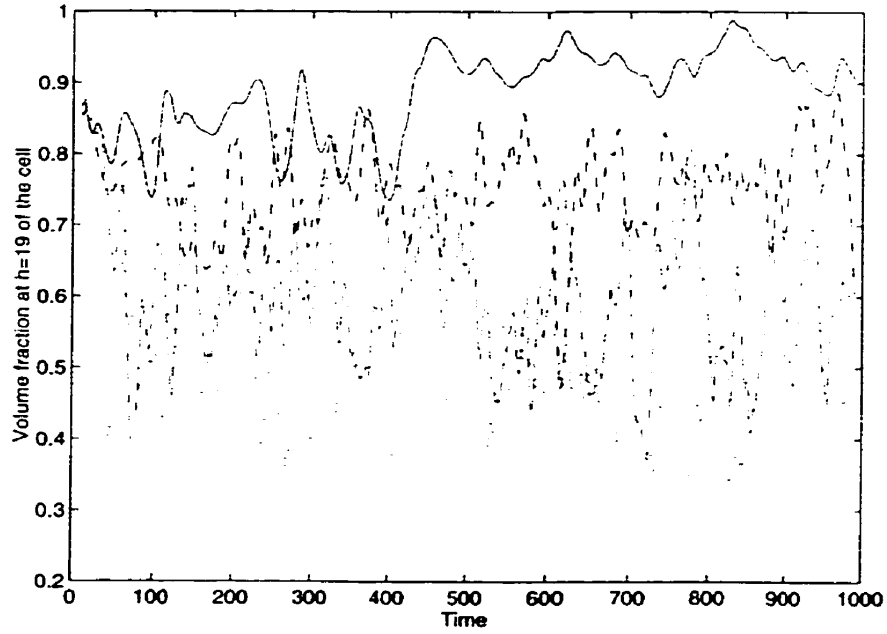

Figure 3.4.10 Volume fraction of particles in spouted bed at h=19 and St=10. Solid line is for u^{∞}=0.2, dash-dotted line for u^{∞}=0.3, dashed line for u^{∞}=0.6, and dotted line for u^{∞}=1.3.

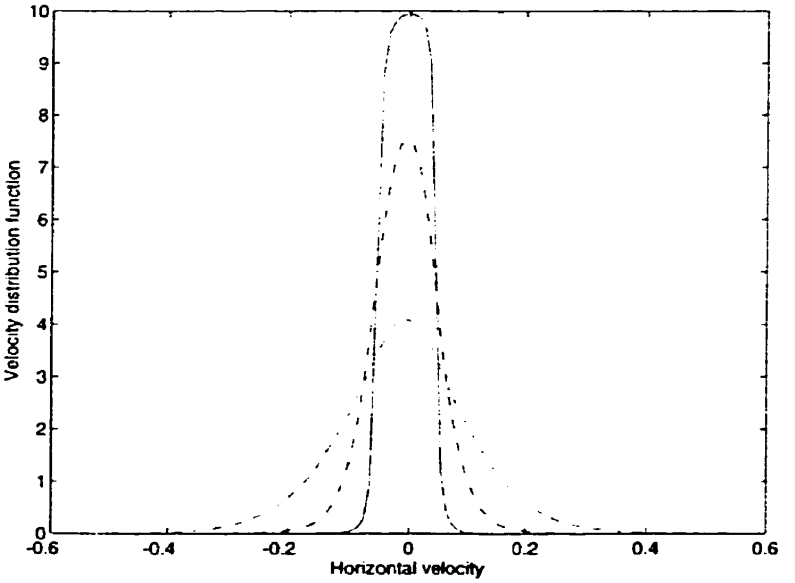

Figure 3.4.11 Velocity distribution of horizontal components of velocities of particles in spouted bed at St=10. Solid line is for $u^{\sim}$=0.2, dash-dotted line for $u^{\sim}$=0.3, dashed line for $u^{\sim}$=0.6, and dotted line for $u^{\sim}$=1.3.

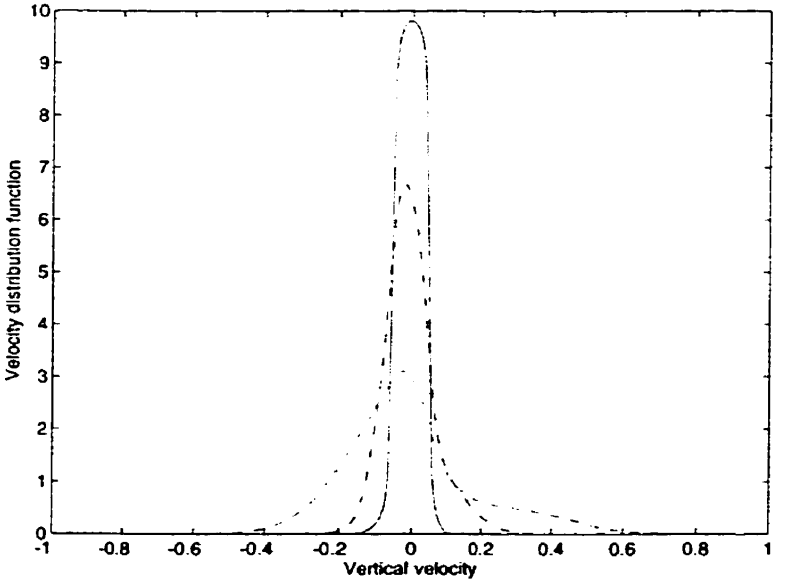

Figure 3.4.12 Velocity distribution of vertical components of velocities of particles in spouted bed at St=10. Solid line is for $u^{\sim}$=0.2, dash-dotted line for $u^{\sim}$=0.3, dashed line for $u^{\sim}$=0.6, and dotted line for $u^{\sim}$=1.3.

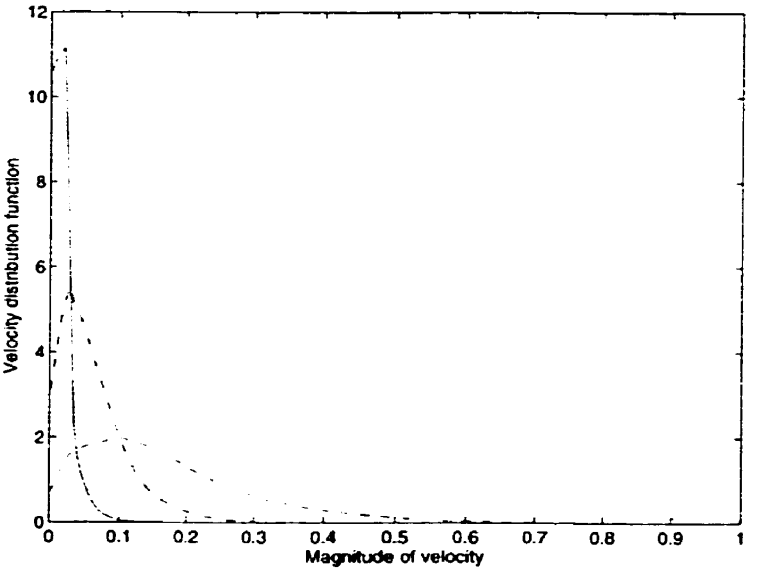

Figure 3.4.13 Distribution of magnitude of velocities of particles in spouted bed at St=10. Solid line is for u^{∞}=0.2, dash-dotted line for u^{∞}=0.3, dashed line for u^{∞}=0.6, and dotted line for u^{∞}=1.3

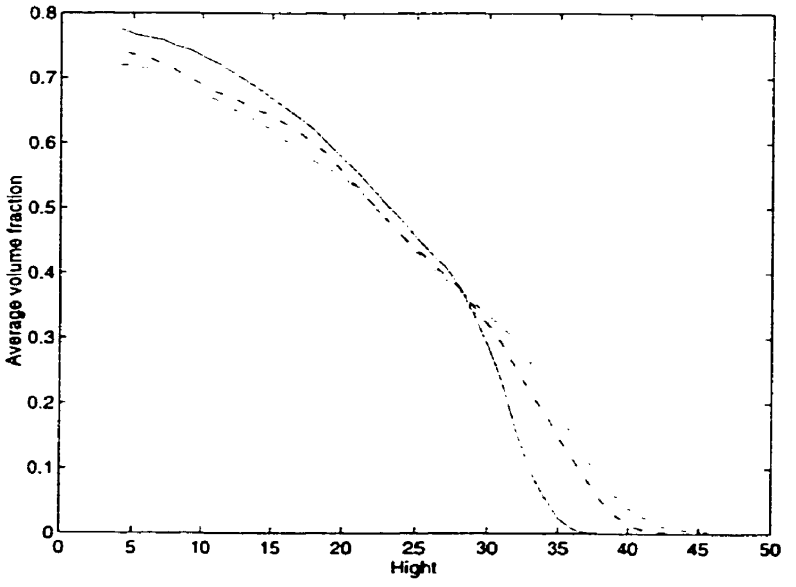

Figure 3.4.14 Average volume fraction of particles along the cell height in spouted bed at u^{∞}=0.6. Solid line is for St=10, dash-dotted line for St=30, dashed line for St=50, and dotted line for St=100.

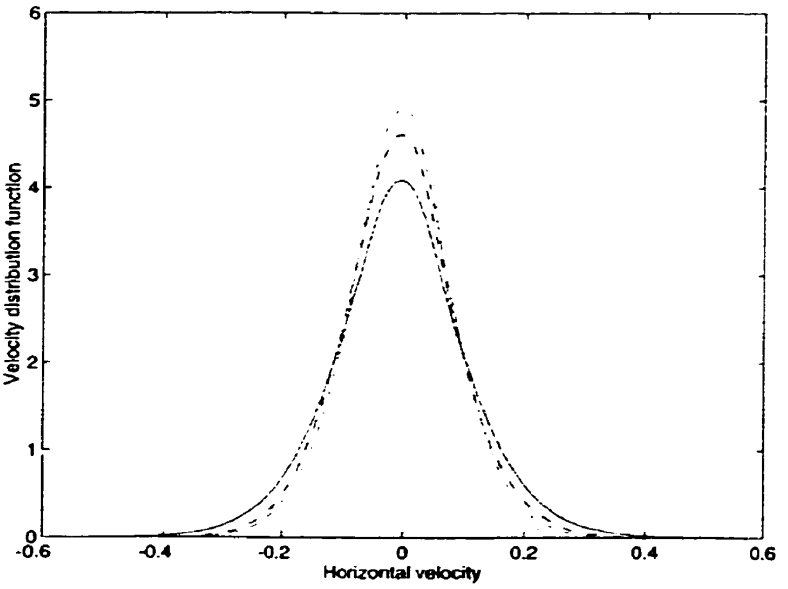

Figure 3.4.15 Velocity distribution of horizontal components of velocities of particles in spouted bed at u^{*}=0.6. Solid line is for St=10, dash-dotted line for St=30, dashed line for St=50, and dotted line for St=100.

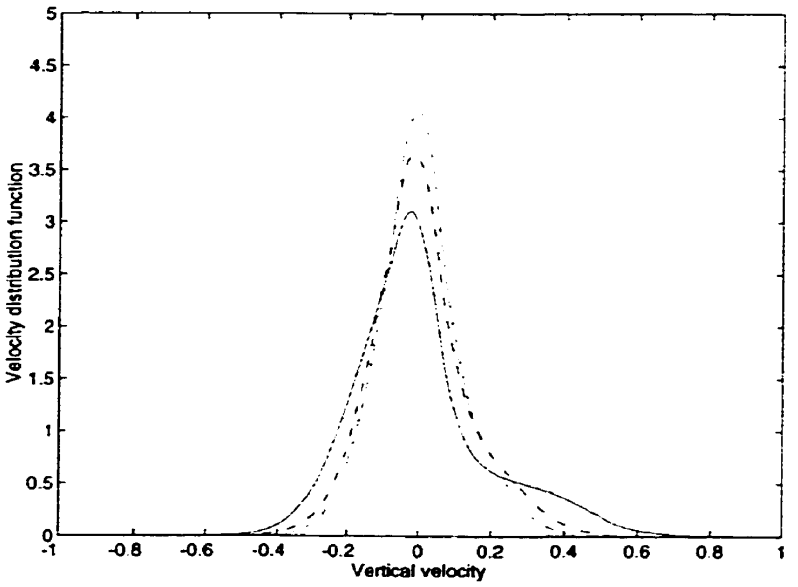

Figure 3.4.16 Velocity distribution of vertical components of velocities of particles in spouted bed at u^{*}=0.6. Solid line is for St=10, dash-dotted line for St=30, dashed line for St=50, and dotted line for St=100.

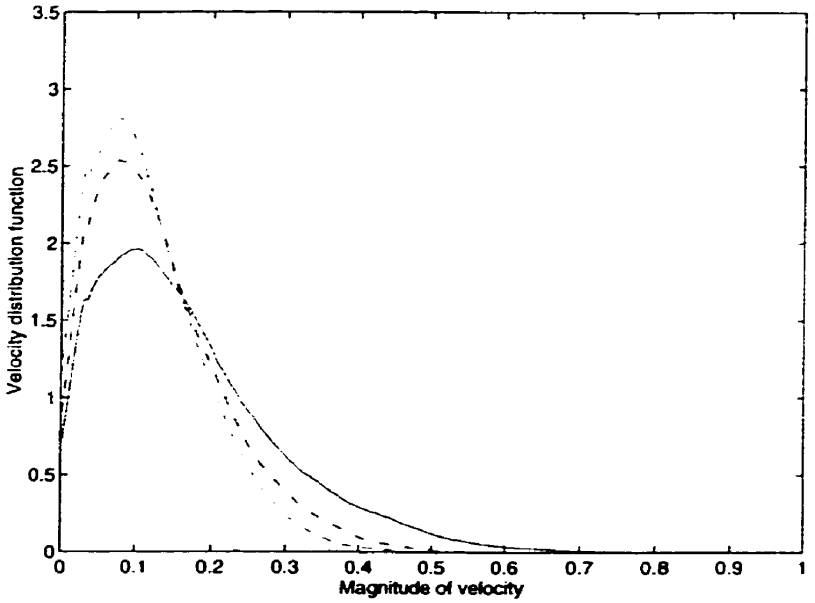

Figure 3.4.17 Distribution of magnitude of velocities of particles in spouted bed at $u^{\sim}$=0.6. Solid line is for St=10, dash-dotted line for St=30, dashed line for St=50, and dotted line for St=100.

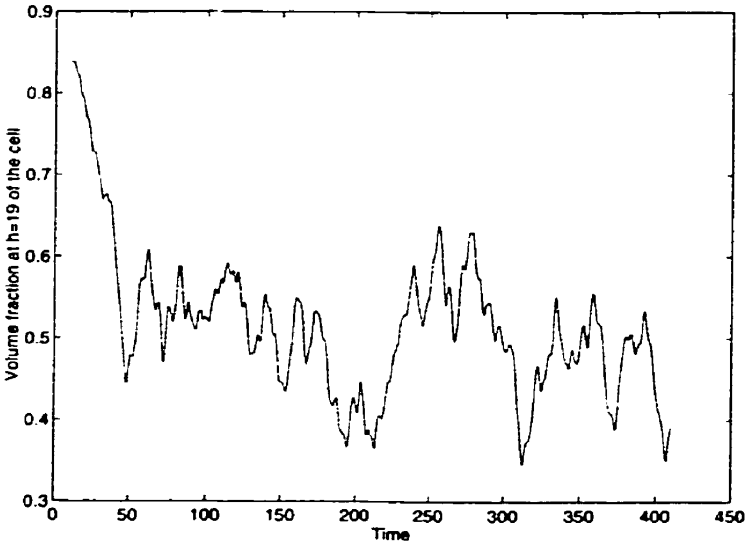

Figure 3.4.18 Volume fraction of particles in spouted bed at h=19, St=10, and $u^{\sim}$=1.

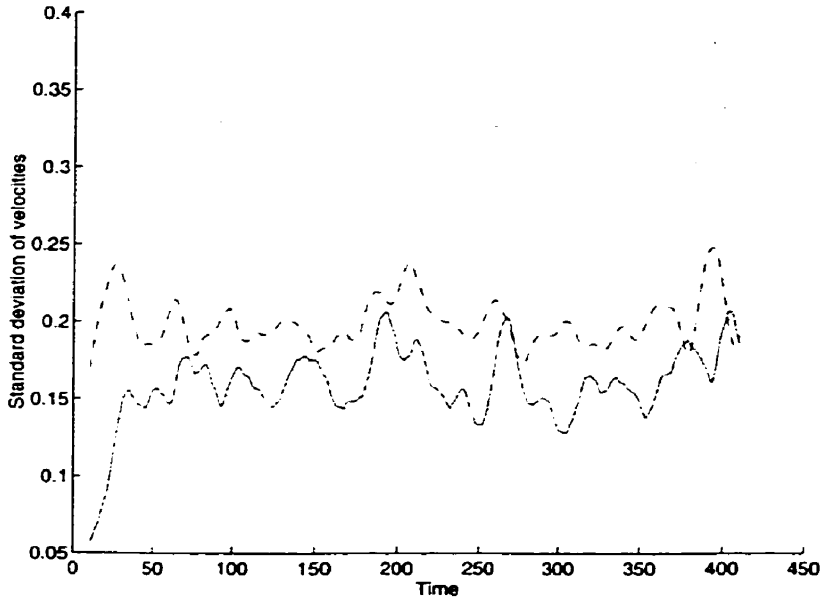

Figure 3.4.19 Standard deviation of velocities of particles in spouted bed at St=10 and $u^{\infty}=1$. Solid line is for horizontal component of velocity, dash-dotted line for vertical component of velocity, and dashed line for magnitude of velocity.

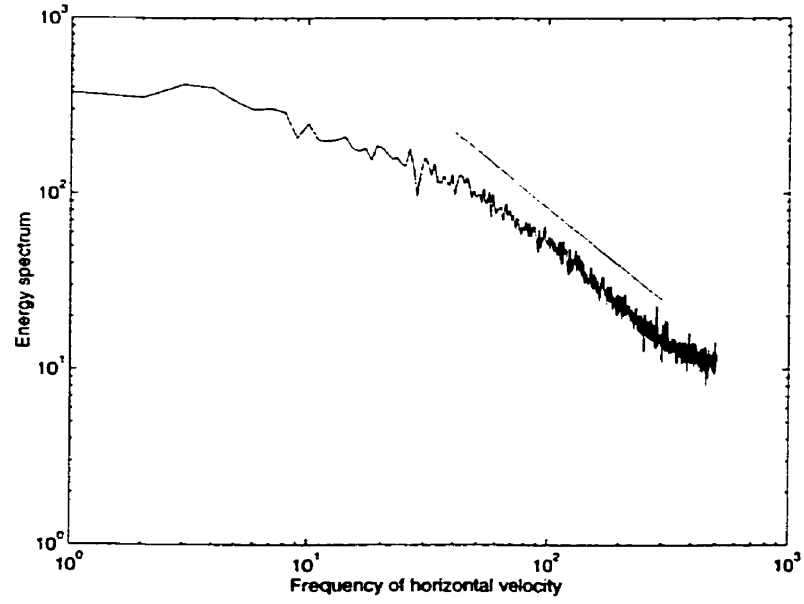

Figure 3.4.20 Energy spectrum of horizontal component of velocities of particles in spouted bed at St=10 and $u^{\infty}=1.3$.

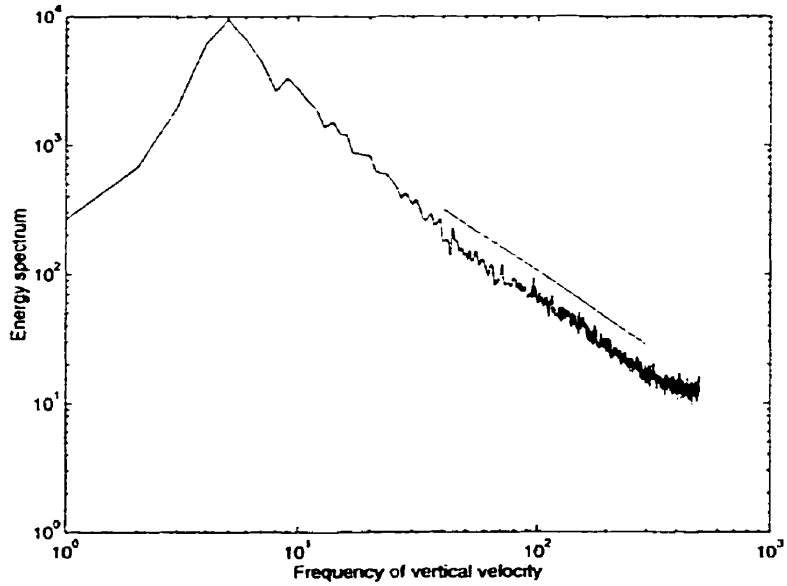

Figure 3.4.21 Energy spectrum of vertical component of velocities of particles in spouted bed at St=10 and u^{∞}=1.3.

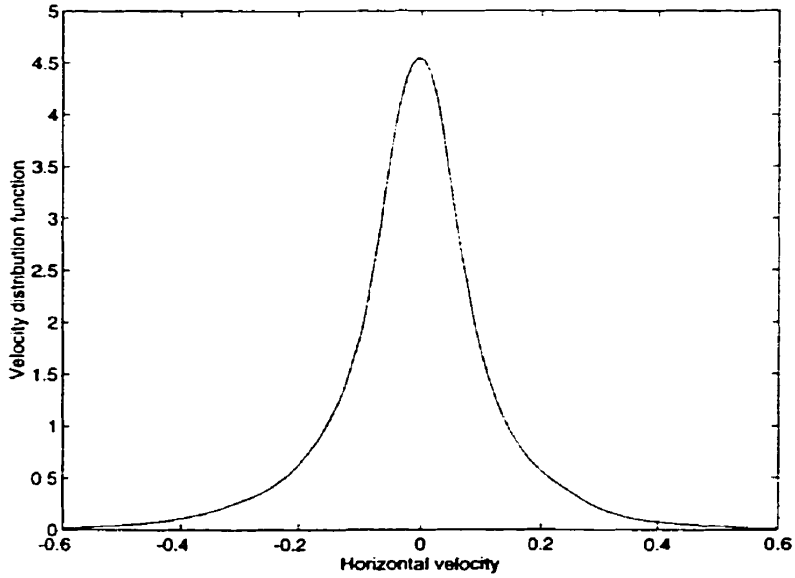

Figure 3.5.9. Velocity distribution of horizontal component of velocities of particles in fluidized bed with mixed cohesive-noncohesive particles at St=10 and u^{∞}=0.25

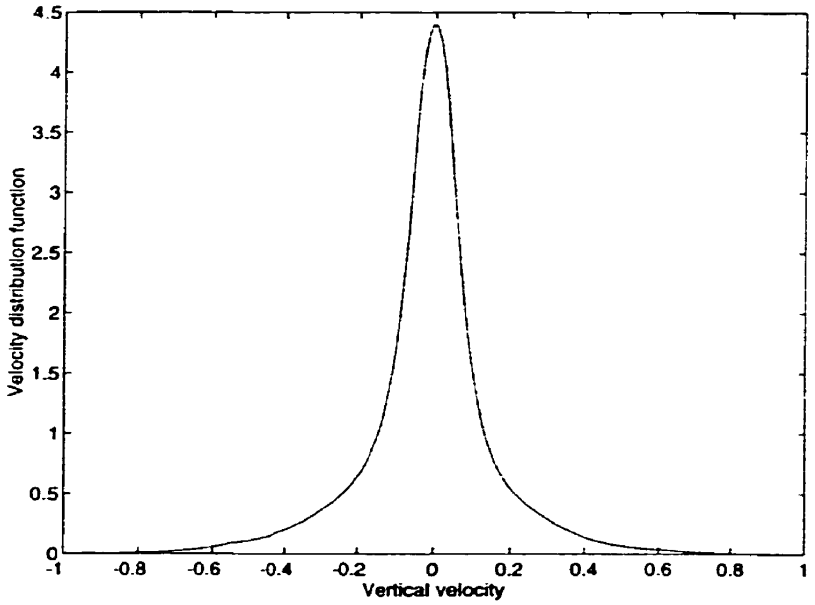

Figure 3.5.10. Velocity distribution of vertical component of velocities of particles in fluidized bed with mixed cohesive-noncohesive particles at St=10 and u^{∞} =0.25

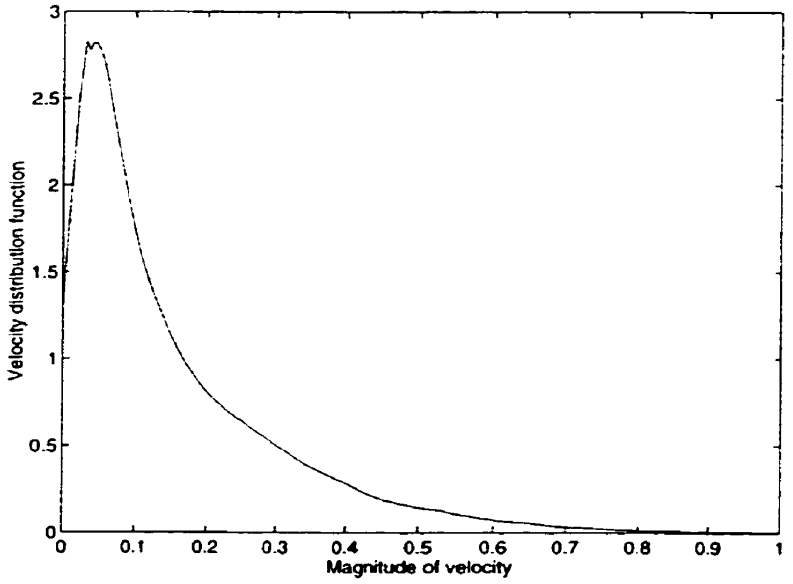

Figure 3.5.11. Distribution of magnitude of velocities of particles in fluidized bed with mixed cohesive-noncohesive particles at St=10 and u^{∞} =0.25

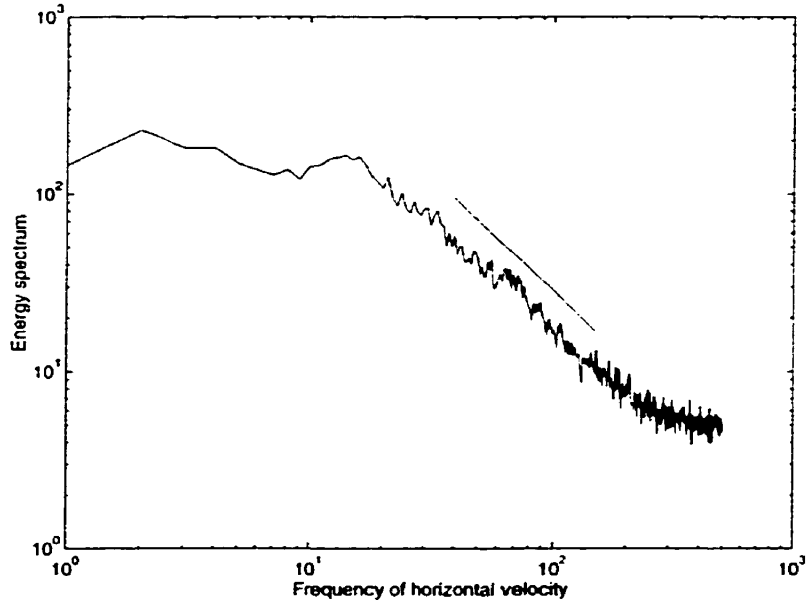

Figure 3.5.12. Energy spectrum of horizontal component of particles in fluidized bed with mixed cohesive-noncohesive particles at St=10, and u^{∞} =0.25.

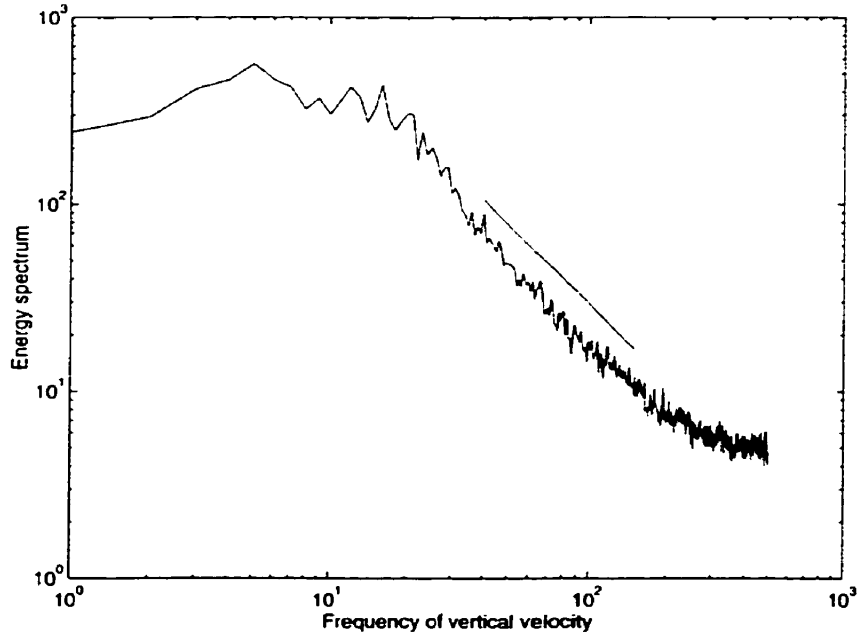

Figure 3.5.13. Energy spectrum of vertical component of particles in fluidized bed with mixed cohesive-noncohesive particles at St=10, and u^{∞} =0.25.